Polymerization in a small droplet on a superhydrophobic surface

by

Fang-Ju Lin

A dissertation submitted to the Graduate Faculty in Chemistry in partial fulfillment of the requirements for the degree of Doctor of Philosophy, The City University of New York

2013

This manuscript has been read and accepted for the
Graduate Faculty in Chemistry in satisfaction of the
dissertation requirement for the degree of Doctor of Philosophy.

Dr. Alan M. Lyons

Date | Chair of Examining Committee

Dr. Maria C. Tamargo

Date | Executive Officer

Dr. Nan-Loh Yang

Dr. Glen Kowach

Dr. Alan M. Lyons

Supervision Committee

THE CITY UNIVERSITY OF NEW YORK

Abstract

Polymerization in a small droplet on a superhydrophobic surface

by

Fang-Ju Lin

Advisor: Dr. Alan M. Lyons

Droplets of fluids have been used as small volume reactors in microfluidic applications, including polymerase chain reaction, as well as synthesis of small-molecules, polymers, and gel particles. More recently, reactions within individual droplets on superhydrophobic surfaces have been studied. However, the fundamentals of polymerization reactions in a droplet on a superhydrophobic surface have not been reported.

To address this issue, firstly, a temperature- and atmosphere-controlled environmental chamber was designed to maintain a constant volume of the droplet on superhydrophobic surface by insuring an equilibrium solvent vapor pressure, eliminating extraneous evaporation or condensation of water. A new technique, micro-dilatometry, was developed to measure the change in volume of the droplet in real-time as a function of photopolymerization conditions. Experimental parameters include photoinitiator concentration, UV light intensity and surface type. In this way, polymerization rate could be calculated in isolated 10 μL droplets.

Droplets on a superhydrophobic surface can be easily and completely lifted off the surface with a syringe because of the weak interactions between liquid and solid surface. Because of this unique aspect of superhydrophobic surfaces, small droplets could be easily analyzed in an external instrument such as NMR or GPC. The percent conversion of monomer to polymer, calculated by micro-dilatometry, was verified by NMR for the same droplet. The molecular

weight of the formed polymer could also be measured by injecting the droplet into a GPC. These results demonstrated good correlation between micro-dilatometry and NMR for percent conversions ranging from 5 - 18%.

Above 18% conversion, experiments demonstrated significant deviations between micro-dilatometry and NMR. Main reason of these discrepancies is proofed to be changes in the vapor pressure of water within the droplet as the concentration of solute molecules decreased significantly during polymerization.

Using the micro-dilatometry technique, the kinetics of polymerization of acrylamide was studied. The polymerization rate within isolated 10 μL droplets was found to be significantly higher than in a well-stirred vial. In addition, the molecular weight of polymers formed in droplets was found to be larger than in the well-stirred system. A hypothesis is presented to explain the higher polymerization rate and molecular weight in small isolated droplets.

Acknowledgments

May I have the pleasure to express my sincere thanks to my advisor, Professor Alan M. Lyons, for the cooperation, and advice during my graduate study. Without his guidance, expertise, and patience, this thesis would not have come to fruition. I will always be grateful for his help. I also want to thank my research committee members, Professor Nan-Loh Yang and Professor Glen Kowach for their time, advice and support.

Table of Contents

List of Figures

List of Table

Chapter 1. Introduction: Photoinitiated Free Radical Polymerization

Photoinitiated free radical polymerization has been extensively studied because it provides a well controlled route for fabrication of materials, exhibits rapid polymerization rates, and the rate can be easily determined by controlling the irradiation period.[1,2] Furthermore, photopolymerization can be conducted at low temperatures, unlike thermal-initiated polymerization that is performed above 40 ℃. With the application of photopolymerization to small droplets (for example, in microfluidics with volumes in the femtoliter to microliter range), questions regarding how the size of the reactor affects the kinetics of photopolymerization arise. The aim of my research is to understand the kinetics of photopolymerization in static droplets: both spherical droplets on a superhydrophobic surface as well as hemispherical droplets on a hydrophobic surface were studied and compared to a well-mixed solution. For this study, an aqueous solution of acrylamide (1.40 M) using Darocur 1173 as the photoinitiator was used. This chapter provides an introduction to the kinetics of photopolymerization and its application to small static droplets on surfaces.

1.1 Mechanistic Understandings

Photopolymerization models have been established and based on three primary reaction mechanisms: initiation, propagation, and termination. The initiation starts using illumination of ultra-violet (250-400 nm) or visible light (400-800 nm). A general mechanism for photopolymerization is described by[3]

Initiation:

Initiator Decomposition $I_2 \xrightarrow{h\nu} 2I\bullet$ (1.1)

Chain Initiation $I\bullet + M \xrightarrow{k_i} R_1\bullet$ (1.2)

Propagation: $R_i\bullet + M \xrightarrow{k_p} R_{i+1}\bullet$ (1.3)

Termination: $R_i\bullet + R_j\bullet \xrightarrow{k_t} P_{i+j} \quad or \quad P_i + P_j$ (1.4)

where I_2 is the initiator, $I\bullet$ is the radical produced from the initiator, M is the monomer, $R_i\bullet$ is a radical of chain containing i monomer units, P is the polymer, hv is the energy of an incident photon, k_i is the rate constant for initiation step, k_p is the rate constant for propagation, and k_t is the rate constant for termination.

The first step of the initiation mechanism is the decomposition of the initiator, where photolysis of initiator (I_2) yields two primary radicals ($I\bullet$). The second step of the initiation on mechanism is the chain initiation step, where a primary radical reacts with a monomer (M) to form a polymer radical ($R_1\bullet$) one unit in length. The second mechanism is Propagation, which represents the growth of the polymer chain by the addition of M to $R_1\bullet$. The last mechanism is Termination, which can take place through two different mechanisms. The first is Coupling, where two growing radical chains react to form one polymer chain (R_{i+j}). The second is Disproportionation, where two polymer chains (R_i and R_j) react to form two terminated polymer chains Ri and Rj. Termination can occur by Coupling, Disproportionation or a combination of Coupling and Disproportionation. Therefore, the mode of termination influences the molecular weight and molecular weight distribution in linear-polymer polymerization system. The central factor of kinetic rate laws for polymerization is the magnitude of rate coefficients (k_i, k_p, and k_t). These coefficients vary with intrinsic properties of initiator and monomer, solvent as well as temperature.

1.2 Typical Phenomena

Various parameters, such as absorption coefficient, quantum yield and concentration of initiators, as well as depth and geometry of the reaction system, influence photopolymerization and affect the reaction rate and molecular weights of polymers. Photopolymerization kinetic parameters are required to evaluate and analyze reaction systems based on reaction rates and polymer molecular weight.

1.2.1 Absorption of Light to Initiate Polymerization

1.2.1.1 The Quantum Yield of Initiation (Φ)

The electronic energy levels of a molecule play an important role in the initiation rate of photopolymerization. Each photoinitiator molecule absorbs light of a particular wavelength and then its energy level changes which leads to initiation. The energy, E, causing excitation in a mole of light is $N\,hc/\lambda$, where N is Avogadro's number, h is Planck's constant, c is the speed of light and λ is the wavelength of exciting light. The energy has a unit of mol^{-1} J. Therefore, a simplified illustration (Fig. 1.1) of the relative positions of the electronic energy level of a molecule helps explain the initiation reaction.

Figure 1.1 shows a Jablonski diagram of the decomposition of an acetophenone type photoinitiator, which undergoes a unimolecular bond cleavage to produce free-radicals,[4] during the polymerization.[2] It can be seen that a photoinitiator molecule in the presence of UV light is converted from its ground state, S_o, to its first exited state, S_1. The initiating route is strongly affected by several pathways. The successive steps of the modes are:

$$S_o \xrightarrow{h\nu} S_1 \longrightarrow T_1 \qquad with \quad \Phi_{ISC} \tag{1.5}$$

$$T_1 \longrightarrow I\bullet \qquad with \quad \Phi_R \tag{1.6}$$

$$I\bullet \xrightarrow{M} R_1\bullet \qquad with \quad \Phi_{RM} \tag{1.7}$$

$$\Phi = \Phi_{ISC} \times \Phi_R \times \Phi_{RM} \leqq 1 \tag{1.8}$$

where S_o is singlet ground state, S_1 is singlet excited state, T_1 is triplet excited state, $I\bullet$ is initiator radical, M is monomer, $R_1\bullet$ is a radical of chain containing one monomer unit, Φ_{ISC} is the fraction of initiator molecules promoted to the triplet excited state per photon absorbed, Φ_R is the fraction of initiator molecules dissociated per photo absorbed, Φ_{RM} is the fraction of chain radicals formed per primary radicals formed, and Φ is the fraction of starting chains per photon absorbed. These modes are summarily quantified in the quantum yield of initiation for the production of a primary free-radical, Φ. The Φ value is smaller than or equal to 1. The Φ value depends on experimental conditions (such as solvent or temperature) and on the nature of the monomer-photoinitiator couple. The rate of initiation, R_i, is proportional to Φ.

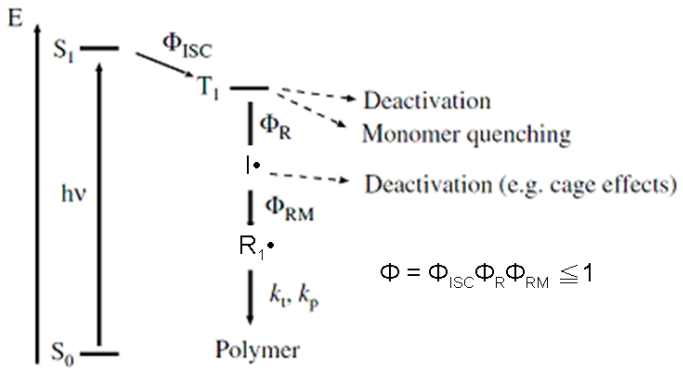

Figure 1.1 Simplified Jablonski diagram of the acetophenone type initiator decomposition of photopolymerization.[2]

There are many types of initiators used for photopolymerization reactions. Acetophenone type photoinitiators are especially interesting to the work in this thesis because they absorb at easily accessible wavelengths (~300 nm) and form no gaseous bi-products. Data for two

common and highly efficient acetophenone type photoinitiators are readily available in the literature: 2,2-dimethyl-2-phenylacetophenone (DMPA) and 2-Hydroxy-2-methyl-1-phenyl-propan-1-one (Darocur 1173). They exhibit high quantum yield Φ_{ISC}, and Φ_{ISC} is generally assumed to equal to 1.[5] Thus, the overall quantum yield Φ of the initiation process of acetophenone type photoinitiator relies only on Φ_R and Φ_{RM}. R_i is proportional to $\Phi_R \times \Phi_{RM}$.

Figure 1.2 indicates the photocleavage of both DMPA and Darocur 1173.[6] The radicals are generated via α-cleavage of DMPA and Darocur 1173 in their T_1 triplet state. The lifetime of the T_1 triplet state influences the quantum yield Φ_R. When the lifetime of the T_1 triplet state increases, the quantum yield Φ_R decreases. The lifetimes of the triplet state of DMPA is less than 0.1 ns, which results in a high Φ_R value of 1.[7] The lifetime of T_1 triplet state of Darocur 1173 is approximately 30 ns, which results in a lower Φ_R value of 0.25.[7,8]

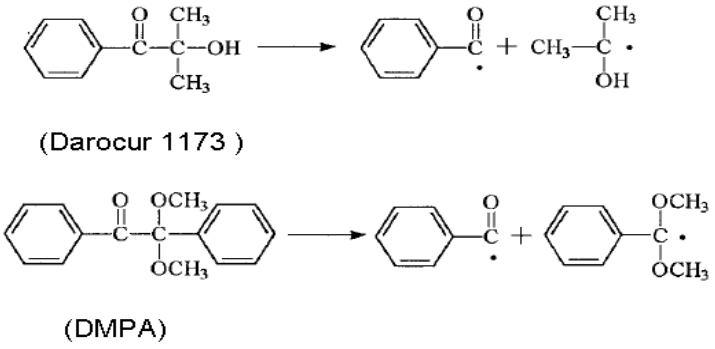

Figure 1.2 Photofragmentation of Darocur 1173 and DMPA.[6]

The quantum yield Φ_{RM} is defined as the initiator efficiency, $f = \Phi_{RM}$. Initiator efficiency is influenced by the ability of radicals to diffuse from the solvent cage to the reaction site, which has been termed the 'cage effect'. The $CO(C_6H_6)$ radical and $C(OCH_3)_2(C_6H_6)$ radical of DMPA exhibit fair reactivity.[7] The radical $COH(CH_3)_2$ of Darocur 1173 is more reactive than its radical $CO(C_6H_6)$.[7] The reactivity of radicals affects the starting macromolecular growth. The f value of

DMPA with 0.7 M MMA in the benzene at 25 ℃ is 0.031.[7,9] The *f* value of Darocur 1173 with methyl methacrylate (MMA) at 25 ℃ is 0.25.[7]

Several literature studies reported the quantum yield, Φ, of DMPA and Darocur 1173 in the presence of oxygen for fabrication of various materials.[7-14] Oxygen can quench the exited triplet state photoinitiator molecules and scavenge radicals. The Φ value of DMPA was reported to be 0.031 with 4.7 M MMA in benzene,[7] 0.1 in triacrylate monomer,[10] 0.25 in butyl acrylate,[11] and 0.4 in aliphatic polyurethane-diacrylate.[12] In addition, Darocur 1173 was shown to have Φ value of 0.15 in *t*-butyl acrylate,[13] 0.2 in methyl methacrylate (MMA),[14] and 0.25 in butyl acrylate.[11] The Φ value of DMPA in presence of nitrogen is reported to be 0.7 in methacrylate.[15] Quantum efficiency of Darocur 1173 is indicated to be 0.73 - 0.88 times the quantum efficiency of DMPA using a fluorescence probe technique.[16] Hence, the Φ value of 1173 could be up to 0.62.

1.2.1.2 The Rate of Initiation

The rate of initiation, R_i, is affected by the quantum yield, Φ, and absorbed light intensity by initiator molecules. Based on the mechanism for photoinitiated free radical polymerization in Reaction 1.1 and 1.2, the rate of initiation of photopolymerization can be represented by[1]

$$R_i = 2\Phi k_i[I] = 2\Phi I_{\varepsilon \ell c} \tag{1.9}$$

where $[I]$ is the concentration of initiator, $I_{\varepsilon \ell c}$ is the moles of absorbed light per liter-second, which is defined by Beer's law, and Φ is the number of propagating chains initiated per photon absorbed. The R_i increase with the amount of absorbed light. The factor of 2 in Eq. 1.9 is used when two identical radicals are produced during the initiation. It may be changed with generation of two different reactive radicals from decomposition of initiator. However, although two

different reactive radicals generated from decomposition of Darocur 1173, Dickey et al. still used the factor of 2 in Eq. 1.9 in their investigation of quantum yield.[13]

1.2.1.3 The Depth of Reaction System

The absorbed light to initiate polymerization is affected by the depth of the reaction system. The absorbed light intensity $I_{\varepsilon\ell c}$ for photopolymerization in thick layers is obtained from the Beer-Lambert law:

$$I'_{\varepsilon\ell c} = I_0 - I_0 e^{-\alpha[I]D} \tag{1.10}$$

where I_o is the incident light intensity (with units of mol cm^{-2} s^{-1}), $I'_{\varepsilon\ell c}$ is the intensity of absorbed light on a layer at a distance D (cm) into the reaction system (with units of mol cm^{-2} s^{-1}), α is the absorption coefficient of initiator (with units of L mol^{-1} cm^{-1}) and [I] is the concentration of initiator (with units of mol L^{-1}). I_o and $I'_{\varepsilon\ell c}$ are surface area intensities of light. $I_{\varepsilon\ell c}$ in Eq. 1.9 is volumetric light intensity.

$I_{\varepsilon\ell c}$ varies with depth of penetration D into the reaction system due to decrease of light intensity through the depth in a thick sample.[17-19] The variation of $I_{\varepsilon\ell c}$ with depth, D, is obtained as differential of $I'_{\varepsilon\ell c}$ with respect to D.

$$I_{\varepsilon\ell c} = \frac{dI'_{\varepsilon\ell c}}{dD} = \alpha[I]I_0 10^3 e^{-\alpha[I]D} \tag{1-11}$$

where the factor of 10^3 is used to convert $I_{\varepsilon\ell c}$ from units of mol cm^{-3} s^{-1} to mol L^{-1} s^{-1}. $I_{\varepsilon\ell c}$ is proportional to concentration of initiator and the absorption coefficient of initiator.

1.2.1.4 The Geometry of Reaction System

When the reaction system is a square cuvette with b cm of path length, the absorbed light intensity $I'_{\varepsilon\ell c}$ is equal to ($I_o - I_o e^{-\alpha[I]b}$). For a spherical reaction system, the average path length of light through the sphere (I_{av}) is dependent on the position of the illumination source.[20] Horowitz et al. calculated the path length through a sphere using an assumption that light sources were isotropic, light came from an infinite distance (parallel light rays) (C_∞).[21] Based on the C_∞ assumption, the average path length I_{av} for a sphere is equal to 4R/3, where R is radius of sphere. The average path length I_{av} for a circle is πR/2 for C_∞ assumption, where π is mathematical constant. Hence, the absorbed light intensity is dependent on the shape of reactors, such as 4R/3 of a sphere and πR/2 of a circle in average path length. The absorbed light intensity in solutions in a vial (with a circular cross-section) changes with the shape of the vial.

The shape of my droplet reactor on superhydrophobic surface and sphere is similar, and hence the average path length of light in droplet can be obtained from the average path length of light in sphere. However, the average path length should be corrected due to the refraction of light from nitrogen into droplet. Refraction is described by Snell's law, $Sin\theta_1 / Sin\theta_2 = n_2/n_1$, where θ_1 is the angle of incidence, θ_2 is the angle of refraction, n_1 is refractive index of nitrogen ($n_1 = 1$) and n_2 are the refractive index of 1.40 M acrylamide ($n_2 = 1.35$). Hence, the average path length in a droplet with a perfectly spherical shape should be longer than that value from assumptions of Horowitz et al.

The average path length I_{av} of a perfectly spherical droplet of 1.40 M acrylmaide can be calculated by modifying the average path length defined by Horowitz et al. by including the refractive index of the solution. A two dimensional circle (cross-section of a sphere) in Fig. 1.3A

is used to explain the assumptions for the path length of light. The length of $\overline{AB}$ in Fig. 1.3A is 4R/3 using assumptions of Horowitz et al. $\overline{AB}'$ in Fig. 1.3A represents the average path length I_{av} considering refraction. When $\overline{AB}$ is 4R/3, $\overline{AB}'$, θ_1, θ_2 are calculated to be 1.67R, 48.2° and 33.5° using Snell's law, respectively.

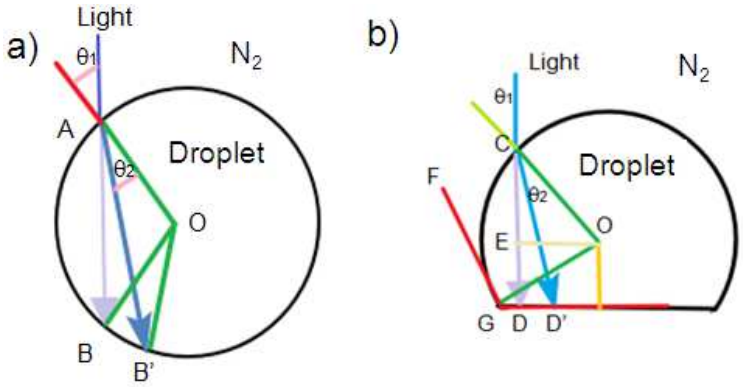

Figure 1.3 Illustration of refraction of light in 1.40 M acrylamide. (A) The light path from nitrogen into 1.40 M acrylamide droplet with perfect sphere. (B) The light path in a droplet on a surface.

However, the shapes of droplets on surfaces are not perfectly spherical. The average path length I_{av} of 1.40 M acrylamide droplet on a superhydrophobic or a hydrophobic surface should be calculated. A two dimensional imperfect circle in Fig. 1.3B is used to explain the path length of light in the droplet on the surface. $\overline{CD}'$ in Fig. 1.3B represents the average path length I_{av} when refraction is considered. A contact angle of a droplet on my superhydrophobic surfaces is 155°, and hence ∠OGD' is 65°. $\overline{CD}'$ is calculated to be 1.63R using refractive index of two media, θ_1 of 48.2° and θ_2 of 33.5°.

For a hydrophobic surface, where the droplet is approximately hemispherical, the contact angle of droplet is 95° and ∠OGD' is 5°. $\overline{CD}'$ is obtained to be 0.78R using refractive index of two media, θ_1 of 48.2° and θ_2 of 33.5°.

1.2.2 Reaction Rates

1.2.2.1 Reaction Rates Using a Steady-State Assumption

Based on the mechanism for photopolymerization in Reaction 1.3 and 1.4, the rate of propagation and termination of photopolymerization can be represented by[1]

$$R_p = k_p[M][R\bullet] \tag{1.12}$$

$$R_t = 2k_t[R\bullet]^2 \tag{1.13}$$

where k_p is the propagation rate constant, k_t is the termination rate constant, [M] is the monomer concentration and [R•] is the total concentration of chain radicals.

Equation 1.12 is not directly used for obtaining rate of polymerization due to the measurement difficulty of concentration of radicals. In order to eliminate [R•] from Eq. 1.12, a steady-state assumption is made that the concentration change of radicals per second remains zero during the polymerization. Thus, the rate of initiation R_i is equal to rate of termination R_t. Based on Eq. 1.9 and 1.13, [R•] is equal to $(\Phi I_{\varepsilon\ell c}/k_t)^{0.5}$. The [$R$•] of Eq. 1.12 can be substituted by $(\Phi I_{\varepsilon\ell c}/k_t)^{0.5}$, and then rate of polymerization is re-written to be:

$$R_p = -\frac{d[M]}{dt} = k_p[M]\left(\frac{\Phi I_{\varepsilon\ell c}}{k_t}\right)^{0.5} \tag{1.14}$$

Equation 1.14 indicates that polymerization rate is dependent on the square root of the quantum yield, Φ, and $I_{\varepsilon\ell c}$. Combining Eq. 1.11 and 1.14, the rate of polymerization is a function of depth

$$R_p = k_p[M]\left(\frac{\Phi\alpha[I]I_o 10^3 e^{-\alpha[I]D}}{k_t}\right)^{0.5} \tag{1.15}$$

The rate of polymerization in Eq. 1.15 is used for polymerization in a narrow layer, where light gradient and reaction gradient are small. Cai et. al. reported that the rate is independent of the depth when 40 μm thin sample of 3,4-epoxy-cyclohexyl-methyl methacrylate was cured with 0.25 wt % DMPA under 100 mW/cm^2 UV light in the presence of nitrogen.[18]

Since rate of polymerization changes with the depth of light penetration into the reaction system, the layer-averaged polymerization rate $\overline{R_P}$ is given by integrating the rate of polymerization over the path length of light and dividing by path length of light.[17]

$$\overline{R}_p = 2k_p[M](\frac{\Phi I_o 10^3}{\alpha[I]k_t})^{0.5}(\frac{1-e^{-\alpha[I]D/2}}{D}) \quad (1.16)$$

Zhang et al. reported that reaction rate is dependent on the depth of the sample using a 4 mm thick sample under 0.130 mW/cm^2 UV light in the presence of oxygen (Fig. 1.4).[19] The cure curve of eighty 0.05 mm thin layers with 0.2 wt % DMPA for analysis of the 4 mm thick sample is shown in Fig. 1.4A. The results indicate the rate at the surface and the bottom of the sample with 0.2 wt % DMPA has a significant difference since the light intensity decreases with depth. However, when the concentration of DMPA is reduced to 0.05 wt %, the difference between the rate at the surface and the bottom of the sample is much smaller as shown in Fig. 1.4B. The rate at the bottom of sample with 0.05 wt % DMPA is faster than that with 0.2 wt % DMPA. The reaction with less photoinitiator is more homogeneous because high concentration initiator absorbs more light to form reaction gradient with increasing depth.

Based on the report of Zhang et al., polymerization distribution difference in a droplet of diameter 2.7 mm with initiator concentration from 0.16 wt % to 0.016 wt % in the presence of nitrogen is expected to be small (see Appendix II), but in a vial, with a path length of ~10 mm, a

significant reaction gradient could occur. Stirring even such a small volume of solution would be required to assure reaction uniformity.

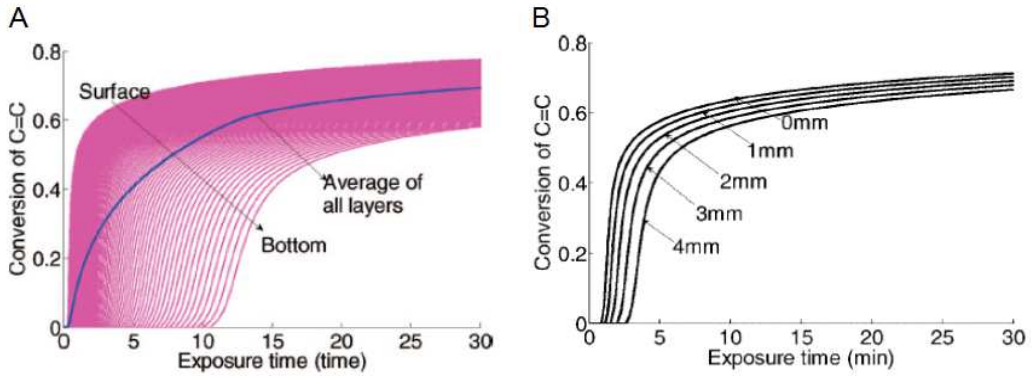

Figure 1.4 Predicted UV cure kinetics of an oligomer, ethoxylated (4) Bisphenol-A dimethacrylate (CD540) at different depths under 0.130 mW/cm^2 (A) 0.2 wt % DMPA and (B) 0.05 wt % DMPA.[19]

1.2.2.2 Reaction Rates Under Non-Steady Conditions

The kinetic of photopolymerization has been extensively investigated using a steady-state assumption. In addition, Eq. 1.14 is used as basis of classical free-radical polymerization kinetics. However, the steady-state assumption is not always applicable. The concentration of radicals will vary as a function of time, especially at the end of the polymerization process. This condition, where the concentration of radicals is not constant, is termed the non-steady condition. The non-steady condition can be carried out using the dark polymerization technique,[22] where the reaction system is exposed by UV light for short time and then placed in the dark, and used to evaluate the rate of polymerization. The change in radical concentration under non-steady conditions is given by[1]

$$\frac{d[R\bullet]}{dt} = R_i - 2k_t[R\bullet]^2 \tag{1.17}$$

Therefore, the rate of polymerization becomes[23]

$$\frac{[M]_t}{(R_P)_t} - \frac{[M]_i}{(R_P)_i} = \frac{k_t}{k_p} \times t \tag{1.18}$$

where the subscripts *i* and *t* refer to the monomer concentration and rate of polymerization at the onset of the dark polymerization and after a given time, respectively. Polymerization rate can be monitored or analyzed by nuclear magnetic resonance (NMR), Fourier-transform infrared spectroscopy (FT-IR), Raman, dilatometry and other techniques. It is useful for evaluation of the kinetic of polymerization.

1.2.2.3 Methods of Determining the Individual Rate Coefficients (k_p and k_t)

An important factor in the assessment of the kinetics of polymerization is to determine the individual rate coefficients k_p and k_t. Common experimental methods for obtaining individual values of k_p and k_t is to use a pulsed laser polymerization – size-exclusion chromatography (PLP-SEC) method and a single pulse-pulsed laser polymerization (SP-PLP), respectively.[22] The pulsed laser polymerization allows the radicals to form for a brief time and propagate until radicals are terminated by a radical at the subsequent pulse.

The individual k_p and k_t values also can be determined using a two step procedure, steady-state and non-steady state polymerization processes. Decker et al. demonstrated this method in an investigation of the kinetics of polymerization of UV-cured surfaces of polyurethane-acrylate.[22] A steady-state polymerization was performed using continuous UV and recorded using real-time Fourier transform infrared (RTIR) spectroscopy (Fig. 1.5A). A $(k_p^2/k_t)^{0.5}$ value was obtained using Eq. 1.15. A non-steady-state polymerization process was performed using dark polymerization, where the reaction system was exposed to UV for 100 ms and then placed in the dark. The polymerization processes was followed using RTIR. A k_p/k_t value at brief time was obtained using Eq. 1.18. Then, k_p and k_t are calculated from the $(k_p^2/k_t)^{0.5}$ and k_p/k_t values.

Figure 1.5B shows that the k_p values remain relatively constant in the initial stage, but decrease above 30% conversion, where propagation becomes controlled by diffusion due to increasing mobility restrictions. The values of k_t rapidly decrease as a function of conversion due to diffusion control termination. The stability of k_p with a rapid decrease in k_t is typical for photopolymerization due to the rapid increase in viscosity which significantly reduces chain mobility. In this example, the low value of k_t illustrates the rapid polymerization rate of multifunctional monomers using the UV-curing technology.

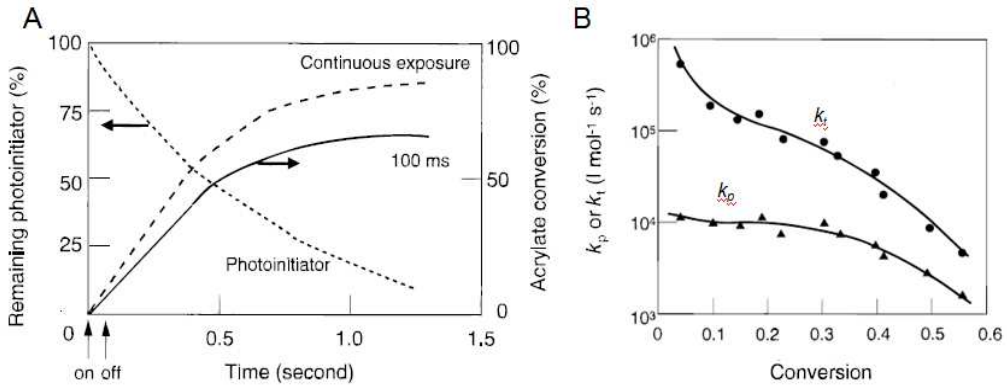

Figure 1.5 (A) Polymerization profiles of monomer under continuous (---) or 100 ms (___) UV exposure of 80 mW/cm^2. Decay profile of initiator (.....). (B) Conversion dependence of the rate coefficients k_p and k_t.[22]

1.2.3 Molecular Weight

The kinetic chain length, υ, is defined as average number of polymerized monomer molecules units per radical and obtained from the ratio of the rate of propagation to the rate of initiation. Using the steady-state assumption, the kinetic chain length is given by Eq. 1.9, 1.12, and 1.14.[1]

$$\nu = \frac{R_p}{R_i} = \frac{k_p[R\bullet][M]}{2\Phi I_{\varepsilon\ell c}} = \frac{k_p[M]}{2(\Phi I_{\varepsilon\ell c} k_t)^{0.5}} \tag{1.19}$$

The number average degree of the polymerization, $\overline{X}_n$, is defined as the average number of monomer molecules contained in a polymer molecule. Disregarding any chain transfer effect, the kinetic chain length is proportional to $\overline{X}_n$.

$$\overline{X}_n \propto \nu = \frac{k_p[M]}{2(\Phi I_{\varepsilon\ell c} k_t)^{0.5}} \tag{1.20}$$

The number-average molecular weight of polymer is give by $M_n = M_0 \overline{X}_n$, where M_0 is the molecular weight of the monomer.

When the termination process occurs only by disproportionation, one polymer is produced per every kinetic chain and $\overline{X}_n$ is equal to υ.[1] When termination process occurs only by coupling, one polymer is produced per two kinetic chains and $\overline{X}_n$ is equal to 2υ.[1] However, disproportionation and coupling can simultaneously occur in actual polymerization reactions. Coupling is the predominate termination mechanism reported for acrylamide, which is the monomer used in my research.[24-27] The coupling/ disproportionation ratio will be addressed in Chapter 4, section 2.11.

Taking chain transfer into account, the number average degree of polymerization is generally given by[1]

$$\frac{1}{\overline{X}_n} = \frac{(2-a)k_t}{k_p^2[M]^2} R_p + C_M + C_s \frac{[S]}{[M]} + C_I \frac{[I]}{[M]} + C_P \frac{[P]}{[M]} + C_T \frac{[T]}{[M]} \tag{1.21}$$

where a is the fractions of termination reaction by coupling, C_M, C_s, C_I, C_P, C_T are chain transfer constants for solvent S, initiator I, polymer P, and added chain transfer agent T. $C_M = k_{tr}^M/k_p$, $C_S = k_{tr}^S/k_p$, $C_I = k_{tr}^I/k_p$, $C_P = k_{tr}^P/k_p$, and $C_T = k_{tr}^T/k_p$, where k_{tr} is the chain-transfer rate constant.

In this research, the effect of chain transfer to water, and Darour 1173 is not anticipated to be significant as the chain-transfer rate constant to water for acrylamide, C_S, at 25 ℃ is zero,[28] and to the initiator (Darour 1173) for acrylamide, C_I, at 25 ℃ is also zero.[29] The number average degree of polymerization for the acrylamide reaction system is given by

$$\frac{1}{\overline{X}_n} = \frac{(2-a)k_t}{k_p^2[M]^2} R_p + C_M \qquad (1\text{-}22)$$

The monomer chain-transfer constant of acrylamide, C_M, at 25 ℃ is 1.2×10^{-5}.[1] Hence, $\overline{X}_n$ of acrylamide could be affected by chain-transfer reaction, if the $k_t R_p/(k_p^2[M]^2)$ is close to or smaller than C_M.

The mean kinetic chain length of low molecular weight polymers can be determined by the content of initiator molecules in polymers using NMR. For higher molecular polymers, the mean kinetic chain length can be obtained using Gel Permeation Chromatography (GPC), Light Scattering, Viscometry, and Mass Spectroscopy. For this research, GPC and a calibration curve based on polyacrylamide standards are used to characterize the molecular weight of polyacrylamide.

1.2.4 Activation Energy and Frequency Factor

Temperature influences the polymerization rate and polymer molecular weight, which depend on rate constants for propagation and termination. The relation of temperature and rate constants can be expressed by an Arrhenius-type relationship, $k = Ae^{-\frac{E}{RT}}$, where A is the collision frequency factor, E is the Arrhenius activation energy, R is the gas constant with a value of 8.314×10^{-3} kJ K^{-1} mol^{-1} and T is the Kelvin temperature. [1,2] Equation 1.14 can be expressed by

$$\ln R_p = \ln[k_p[M](\frac{\Phi I_{\varepsilon \ell c}}{k_t})^{0.5}] = \ln(\frac{A_p}{A_t^{0.5}}) + \ln[(\Phi I_{\varepsilon \ell c})^{0.5}[M]] - \frac{E_P - E_t/2}{RT} \quad (1.23)$$

where E_p-E_t/2 is overall activation energy for the rate of polymerization, E_R. A plot of lnR_p vs 1/T, the (E_p-E_t/2)/R will be obtained by slope. The E_R for photopolymerization is about 20 kJ mol^{-1}.[1] Equation 1.22 can be expressed by

$$\ln\frac{1}{\overline{X}_n} = \ln[\frac{(2-a)(k_t\Phi I_{\varepsilon \ell c})^{0.5}}{k_p[M]} + C_M] = \ln[\frac{(2-a)(A_t e^{-\frac{E_t}{RT}}\Phi I_{\varepsilon \ell c})^{0.5}}{A_P e^{-\frac{E_P}{RT}}[M]} + C_M] \quad (1.24)$$

Hence, the rate polymerization increases and the degree of polymerization decreases with increasing temperature.

1.2.5 The Effect of Diffusion on the Termination Reaction

The termination reaction occurs by coupling and/or disproportionation. Termination by disproportionation has higher activation energy.[30] Termination by coupling has lower activation energy and so it is controlled by diffusion.[30] Hence, termination of acrylamide, which is reported to be predominated by coupling, is controlled by diffusion. For general bulk linear polymers, the effect of diffusion becomes more significant as the percent conversion reaches 40-50% as the higher viscosity and chain entanglements decrease the ability of the growing polymer chains to diffuse.[31] Based on Smoluchowski theory, where the termination mechanism is completely diffusion controlled, the rate constant for diffusion limited termination of bulk polymerization of methyl methacrylate is defined by the encounter frequency of the two reacting species.[31]

$$k_t = 4\pi D R_c N_{AV}/1000 \quad (1.25)$$

where k_t is rate constant of termination, D is the reaction diffusion, R_c is a capture radius of termination and N_{AV} is Avogadro's number. The behavior of D is expressed by the Stokes-Einstein equation.[32]

$$D = \frac{k_B T}{6\pi R \eta} \tag{1.26}$$

where k_B is the Boltzmann constant, T is (absolute) temperature, R is the hydrodynamic radius of polymer, and η is the viscosity of the reaction mixture. When polymer chains are unable to move freely, diffusion is reduced, which reduces their sphere of mobility and reduces opportunities to encounter other radical chains. When this occurs, termination does not occur rapidly and k_t is small. Similarly, polymerization at low temperatures, in high-viscosity solvents or in poor solvents also shows low diffusion, and hence lower values of k_t.[30]

A special phenomenon, where the reaction rate increases with increasing conversion, is called autoacceleration or the Trommsdorff effect. Figure 1.6 shows the polymerization of methyl methacrylate (MMA) at different concentrations in benzene.[1] The polymerization behavior of 10% v/v MMA is well-controlled and follows expected kinetics. In the bulk, however, the reaction of MMA accelerates very significantly beyond 20% conversion. The autoacceleration occurs at lower percent conversion with increasing concentration of monomer. This autoacceleration behavior is usually ascribed to the increasing viscosity of the system, which retards translational diffusion of the chain radicals, and so the termination reaction becomes controlled by diffusion of monomer.[33]

Stirring and convective mixing in reaction systems is able to improve the mobility of chain radicals, increasing the encounter opportunities for chain radicals, and smooth out reaction gradients as well as temperature gradients.[34,35,46] Nunes et al. reported that cross-linked

acrylonitrile-divinylbenzene particles with narrow size distribution were produced in mechanical stirring conditions (300 and 400 rpm) using semi-suspension polymerization.[36] In some microfluidic systems, the design of macrochannels can improve the mixing of reactants. When small droplets are generated in microfluidic channels, the interior of droplet can be mixed using pressure-driven flows in sinusoidal channels (Fig. 1.7).[37] The uniform mixing of reactants in droplets increases the uniformity of the reaction and the mobility of chain radicals.

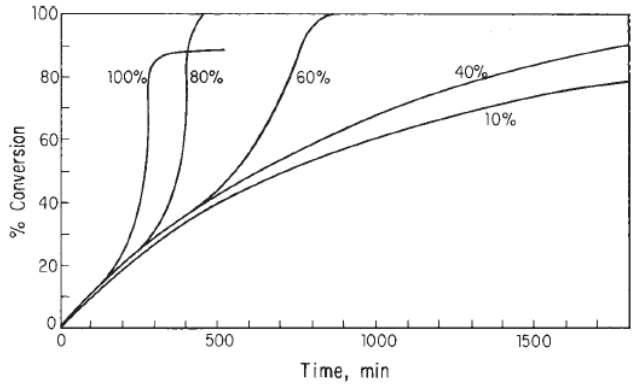

Figure 1.6 Autoacceleration in benzoyl peroxide-initiated polymerization of methyl methacrylate in benzene at 50 °C.[1]

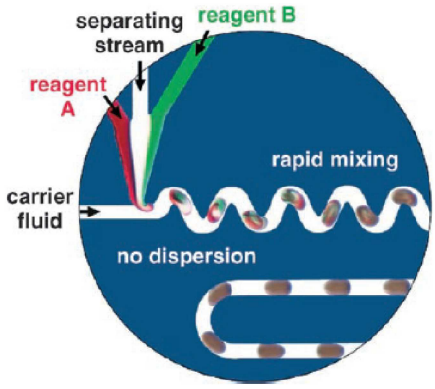

Figure 1.7 Droplets formed within microfluidic channels can be considered as microreactors. In this example, reagent A, reagent B, and separating stream are converged to form a droplet using a carrier fluid. The reagents are rapid mixed in the droplet in the sinusoidal channel. After mixing, the reactions can be performed within the droplet.[37]

However, the fabrication processes for some materials requires that no mixing occurs in order to retain their dispersed phases. The fabrication process for Janus particles is one example.[38-44] Janus particles are composed of two separate materials joined together such that each hemisphere of the particle has a different composition. When small droplets are formed by combination of two aqueous phases in a continuous oil phase, the droplets can be crosslinked rapidly by photopolymerization, before diffusion can occur. Thus, the two aqueous phases combine without mixing to form Janus particles. Yuet et al. demonstrated the fabrication of multifunctional superparamagnetic Janus particles 48 μm ± 1.8 μm in diameter (Figure 1.8).[38]

To reduce the mobility of chain radicals to fabricate high molecular weight polymers, some polymerizations are performed by cycling between high and low temperatures. Holtze et al. demonstrated this method in a free radical miniemulsion polymerization, which was initiated in a microwave oven, to obtain ultra-high molecular weight polystyrene.[45,46] The mechanism of the miniemulsion polymerization is predominantly based on droplet nucleation, where the monomer droplet acts as reactor, and hence the nucleation step of ab initio emulsion polymerization is avoided (Fig. 1.9). In their reaction system, radicals were generated during short pulse of high temperature (9-12 s), and polymer chains alternately grew in a droplet 100 nm in diameter at 0 ℃ for 15 min. The molecular weight of polymers was not dependent on the concentration of initiator but limited by chain transfer to monomer (in accordance with transfer limit). For example, the transfer limit of polystyrene at 80 and 0 ℃ are about 10^6 and 10^7 g mol^{-1}. Hence, ultra-high molecular weight polystyrene was obtained because a great number of radicals were formed at high temperature, but due to rapid cooling, were allowed to grow at low temperature (0 ℃) until the molecular weight achieved the chain transfer limit.

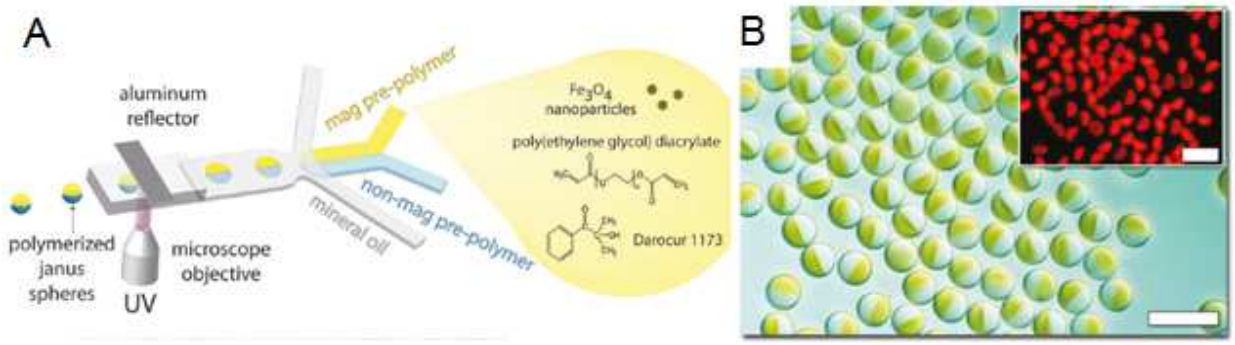

Figure 1.8 (A) Schematic of Janus particles synthesis in microfluidic channels. (B) Camera and corresponding fluorescent (insert) image of magnetic Janus particles, containing magnetic nanoparticles and rhodamine B. The scale bars are 100 μm wide.[38]

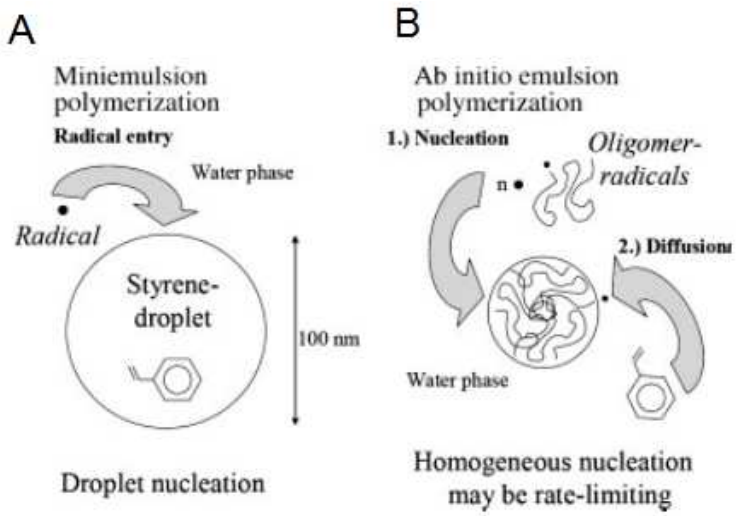

Figure 1.9 (A) Droplet nucleation in a pulse temperature technique. (B) Nucleating step in ab initio emulsion polymerization.[46]

In larger droplets (e.g. 2 - 3 mm in diameter), like the ones described in this thesis, the reaction conditions exhibit both similarities and differences relative to the smaller droplets studied in microchannels and miniemulsion. The size is much greater and so single radical reactions, like those found in a pulsed miniemulsion, are not likely. However, isolated 2 - 3 mm droplets on a superhydrophobic surface will experience a uniform temperature across the volume. In addition, since evaporation can be limited by control of the droplet environment, evaporation can be completely suppressed, and so convection within the droplet would not occur. Thus,

molecules within an isolated large droplet would experience significant essentially no mixing and would behave more like a droplet within a straight microchannel.[47] Hence, low diffusion of chain radicals in the droplets could promote the synthesis of high molecular weight polymers with relatively narrow molecular weight distributions.

1.2.6 Studies of Acrylamide Polymerization

Acrylamide and its polymers were selected for study as both are soluble in water, a solvent required to achieve spherical droplets on a superhydrophobic surface. A second reason to study acrylamide is that the polymerization reaction is well understood and kinetic investigations have been published.[24-26,48]

The propagation rate coefficient (k_p) of acrylamide (AAm) in water has been determined by the PLP-SEC method.[24] The results show that k_p values are dependent on the initiator concentration, monomer concentration and temperature. As the concentration of initiator (uranyl nitrate or 2,2'-azobis(2-amidinopropane)dihydrochloride also known as V-50), increases from 0.002 M to 0.010 M, the value of k_p value decreases from 6.56×10^4 to 5.50×10^4 L mol^{-1} s^{-1}. Similarly, as the concentration of acrylamide increases from 0.32 M to 1.40 M, k_p value decreased from 6.84×10^4 to 6.32×10^4 L mol^{-1} s^{-1}. The value of k_p also increases with increasing temperature from 3.40×10^4 to 9.61×10^4 L mol^{-1} s^{-1} as the temperature increased from 5 ℃ to 50 ℃. Searbook et al. reported that the concentration dependence of k_p results from solvent effects (thermodynamic effects) and activation energy changes (effects of the solvent on the structure of the reactant and transition state).

The termination rate coefficient (k_t) of acrylamide with uranyl nitrate in water was investigated at 50 ℃ using γ-radiolysis relaxation, where γ-radiation provides a means whereby

initiation can be stopped and polymerization rate monitored over time; this technique is sensitive to radical-loss processes. [25] The k_t value ranged from 8×10^6 to 3×10^7 L mol^{-1} s^{-1} as the weight fraction of polymer ranged from 0.002 to 0.0035, which is lower than the low conversion values for styrene (2×10^8 L mol^{-1} s^{-1}).[25] The relatively slow diffusion of large polymer chains were found to be primarily responsible for the low value of k_t; the relatively high value of k_p also contributes to the low k_t value. The results were explained by a chain-length-dependent model of free-radical polymerization kinetics, where termination kinetics are expressed in terms of a diffusion controlled encounter of radicals.[25]

The polymerization rate of acrylamide with initiator, UO_2^{2+}, V-50 or persulfate, in water at 25 ℃ was studied using situ Raman spectroscopy.[26] The dependence of polymerization rate on initiator concentration and initiator type show that the classical free-radical polymerization kinetics provides an acceptable description for this system.

Dainton et al. reported that the propagation rate constant of acrylamide initiated by hydrogen peroxide in aqueous solution at 25 ℃ is $(1.80 \pm 0.15) \times 10^4$ L mol^{-1} s^{-1}.[48] The termination rate constants is $(1.45 \pm 0.20) \times 10^7$ L mol^{-1} s^{-1}. They reported that chain transfer to monomer, $k_{tr,m}$, is 2.2×10^{-1} L mol^{-1} s^{-1} and chain transfer to initiator, $k_{tr,i}$, is 9 L mol^{-1} s^{-1}. Hence, the ratio $k_p/k_t^{0.5}$ was calculated as 4.7 ± 0.7 L$^{0.5}$ mol$^{-0.5}$ s$^{-0.5}$ as shown in Table 1.1.

Table 1.1 The kinetic parameters for 0.48 M acrylamide in water or aqueous solution.

Researcher	k_p (L mol^{-1} s^{-1})	k_t (L mol^{-1} s^{-1})	$k_p/k_t^{0.5}$ (L$^{0.5}$ mol$^{-0.5}$ s$^{-0.5}$)	Initiator	T[(a)] (℃)
Seabrook[24-26]	8.98×10^4	2.30×10^7	19	0.002 M UO_2^{2+}	50
Seabrook[24] from model	4.40×10^4	1.12×10^7	13	0.002 M UO_2^{2+}	20
Dainton[48]	1.80×10^4	1.45×10^7	4.7	0.001 M H_2O_2	25

(a) Temperature.

Kinetic parameters of photopolymerization for 0.48 M acrylamide in water are summarized in Table 1.1. The values of k_p and k_t both increase with increasing temperature however k_p is much more sensitive to temperature. The values of k_p are more strongly affected by initiator. The range of $k_p/k_t^{0.5}$ values is form 19 to 4.7 $L^{0.5}$ $mol^{-0.5}$ $s^{-0.5}$ between 50 and 20 ℃. These investigations provide a foundation on which to base my research.

1.3 Applications in a Droplet on a Superhydrophobic Surface

Photopolymerization has been investigated[49-50] and widely applied in surface coatings and ink[51] as well as in the fabrication of microchannels,[52-54] superhydrophobic surfaces,[55-57] and hydrophilic surfaces,[58] as heating is not required and due to its simple experimental procedure. In addition, it was performed in droplets to fabricate spherical,[59-63] non-spherical,[64-68] or multifunctional particles,[38-44] because droplet size is beneficial in reducing the possibilities of temperature gradients and reaction gradients inside the droplet during polymerization.[19,69] In addition to these applications, the design of reaction systems that can precisely control the size and function of materials has attracted great attraction.[70]

Numerous studies of reactions in droplets have been performed in microfluidic systems,[38-44,59-68] where droplets are generated using microchannels with two immiscible liquids and pressure-driven flows. Interest in droplet-based microfluidic systems has increased since the Nakajima group first demonstrated the formation of oil-in-water and water-in-oil droplets in silicon microchannels in 1997.[58] Microfluidic methods offer the advantage of high throughput of uniform droplets, as well as controlled mixing and efficient thermal exchange in small droplets.[71] Various materials, such as cells, DNA, proteins, and small molecules, can be introduced into droplets and used to for measurement of kinetics of enzymatic activity, polymerase chain

reaction (PCR), small-molecule synthesis, self-assembly of materials and UV photopolymerization.[71] The volumes of droplets in microfluidic systems are in the femtoliter to microliter range (10^{-15} to 10^{-6} L) for various reactions.[38-44,59-71]

One of the drawbacks of the microchannel approach, however, is that it is difficult to separate the droplets from the continuous oil phase. To address this issue, Khan et al.[72] reported an air-liquid segmented flow to synthesize colloidal silica in hydrophobic microfluidic devices in 2004. Due to the relatively weak forces between droplets and the hydrophobic surfaces, movement of the droplets could be achieved by a directed flow of air. Since only air surrounds the droplet, there is no oil phase to contaminate the droplet. However, a superhydrophobic surface would provide additional benefits due to reduced friction and contact area between the droplets and the surfaces.

Properties of surfaces are evaluated by measuring the wetting properties of water droplets on the surface. When water contacts a smooth surface, it forms a droplet with a characteristic shape and forms an angle with the surface that depends upon the balance of forces between the liquid-solid, solid-vapor and vapor-liquid interfaces. This contact angle is described by the Young equation, $\cos\theta = \frac{y_{SA} - y_{SL}}{y_{LA}}$, where y_{SA} and y_{SL} are the surface energies of the solid against air and liquid, and y_{LA} is the surface energy of liquid against air. If the surface is roughened the liquid may still completely contact the solid surface as shown in Fig. 1.10A. This is called the Wenzel state.[73] The apparent contact angle between liquid and solid is described by the Wenzel equation: $\cos\theta_{roung} = r\cos\theta_{flat}$, where θ_{rough} is the apparent contact angle of water on a rough surface, θ_{flat} is intrinsic water contact angle on a smooth surface and r is the roughness factor. However, if the surface is made of a low-energy material with sufficient roughness, then

water on the surface will span across rough features. This is called the superhydrophobic or Cassie state. In this state, water at the lower interface contacts both air and the raised portions of the solid surface as shown in Fig. 1.10B.[73] The contact angle of a liquid in this state can be calculated using the Cassie-Baxter equation: $Cos\theta_{roungh} = \Phi_s \times Cos\theta_{flat} - (1-\Phi_s)$, where Φ_S is the fraction of solid surface that contacts water. Properties of surfaces are directly evaluated by water contact angle (CA), an expression of wettability.[74] A surface on which water forms a CA that is larger than 150° is called a superhydrophobic surface. With a CA between 150° and 90°, it is called a hydrophobic surface. When the CA is less than 90°, the surface is called a hydrophilic surface.

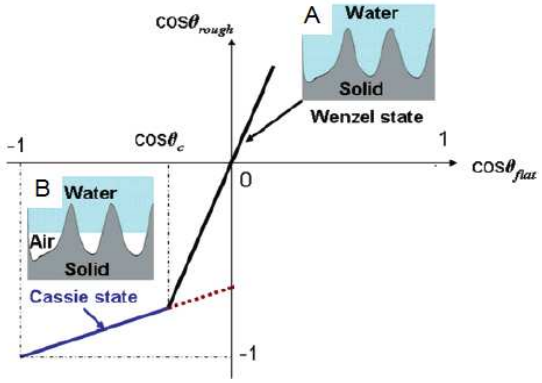

Figure 1.10 Relationship of $\cos\theta_{rough}$ with $\cos\theta_{flat}$. (A) Wenzel state, and (B) Cassie-Baxter state.[73]

Evaporation of droplets on these two types of hydrophobic surfaces proceeds differently. When a droplet in a Wenzel state evaporates, the perimeter along the liquid-solid-vapor triple contact line (TCL) remains constant; the droplet shrinks from the liquid-air interface downward. On a superhydrophobic surface, however, the TCL is not pinned and lateral contraction of the droplet can occur as shown in Fig. 1.11.

Experimental methods for characterizing superhydrophobic surfaces include the measurement of the contact angle of droplets on the surface as well as the tilt angle required for a

drop to slip along the surface.[75-84] The size of water droplet on superhydrophobic surface is dependent on the diameter of needle and usually from 1 to 20 μL due to the low-adhesive properties of surface.[75-83] While the adherence of the surface of needle is larger than that of the surface or than mass of the droplets, the droplets do not move to the surface.

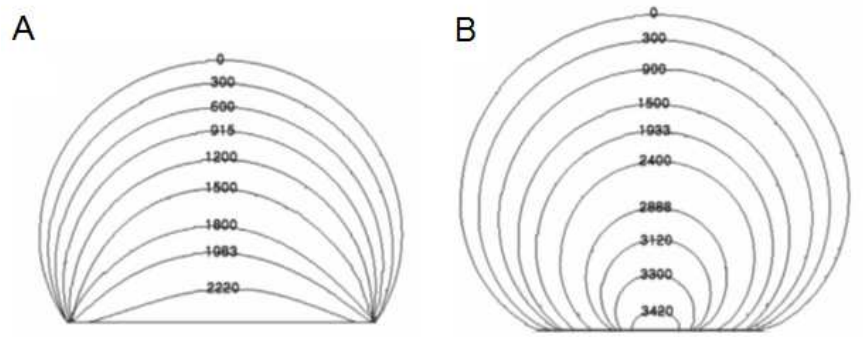

Figure 1.11 Drying droplet side profile from digital images. The numbers on contours indicate time in second. The innermost profile corresponds to final shape. (A) A droplet on a hydrophobic surface. (B) A droplet on a superhydrophobic surface.[80]

At present, only a few investigations of reactions in a droplet on a superhydrophobic surface have been reported.[85-89] Su et al. performed fluorescence quenching reaction and gas- or precipitate- forming reactions in a 20 μL droplet.[85] Ueda et al. reported a method for encapsulating fluorescent cells in an isolated microliter-size droplet on a superhydrophilic-superhydrophobic patterned surface.[86] Accardo et al. demonstrated coalescence and reactive mixing of droplet-based microreactors, $CaCl_2/Na_2CO_3$ solutions, using a superhydrophobic electrowetting-on-dielectrics device (SHEWOD).[87]

Lima et al. demonstrated the fabrication of temperature-responsive hydrogel particles with a protein on the superhydrophobic surface using photoinitiated polymerization (Fig. 1.12).[88] At first, Poly(N-isopropylacrlamide) (PNIPAAm) was synthesized in water at room temperature using 0.88 M NIPAAm, a redox initiator (0.035 M ammonium persulfate (APS)), and a

crosslinking agent (0.019 M N,N-methylenebisacrylamide (MBIS)). Then, a mixture of 0.012M Darocur 1173 and 0.002 M protein (bovine serum albumin (BSA)) and 0.00008 M Dextran-MA was prepared and then added into PNIPAAm solution. Finally, the reactants were dropped on surface to form 5 µL droplets and then polymerized using UV light (254 nm). After 10 min irradiation time, hydrogel particles were obtained and easily detached by inclining the surface. The diameter of particles is about 1.0 - 1.5 mm.

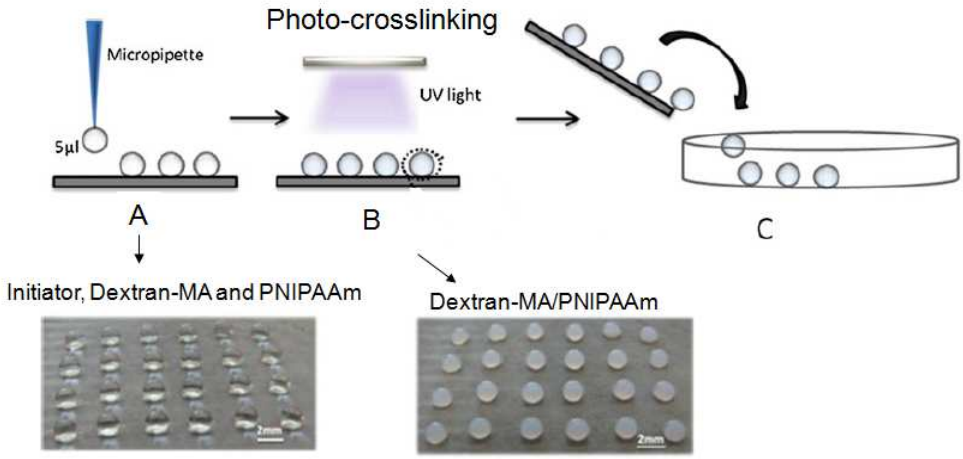

Figure 1.12 Schematic of superhydrophobic surface used to synthesize hydrogel particles. (A) Dropping of initiator, Dextran-MA and PNIPAAm solution on surface. (B) Droplets photocrosslinking (UV light). The diameter of sphere shaped particles is 1 - 1.5mm. Scale bar is 2 mm.[88]

Lima et al. did not illustrate that photocrosslinking was performed under saturated vapor pressure, where the composition of droplets did not change before polymerization. When reaction condition is under a reduced vapor pressure of water, polymerization and evaporation of the droplet occur simultaneously. In addition, they did not indicate the size distribution of particles, which would demonstrate the advantage of the method for the fabrication of the particles. Hence, although Lima et al. provide a rapid method to fabricate particles, they did not study droplet stability or reaction kinetics.

1.4 Motivation and Approach

The ability to easily create small mobile droplets on a superhydrophobic surface enables the study of polymerization reactions in these small reactors. Accurate real-time monitoring of polymerization in a droplet is an important method to understand the kinetics of the reaction. In this thesis, the polymerization of droplets was studied in an environmental chamber with controlled stability such that the volume of the droplets could be controlled. A micro-dilatometry technique for monitoring polymerization kinetics in isolated small (~ 10 microliter) aqueous droplets on a surface is introduced. The micro-dilatometry technique uses a digital contact angle goniometer to record droplet volume during polymerization. The rate of polymerization is determined from the shrinkage of the droplet and confirmed by ^{1}H NMR. Since the droplets can be easily lifted off the surface, the droplets could be characterized either by NMR or the polymer molecular weight determined by GPC. Figure 1.13 shows schematics of a 10 µL droplet on a hydrophobic and a superhydrophobic surface. Because of the small size and uniform temperature, convection does not occur within the droplets and so no mixing occurs during polymerization. As a result, the growing chains are expected to be relatively immobile and termination of polymerization reactions would be limited by diffusion.

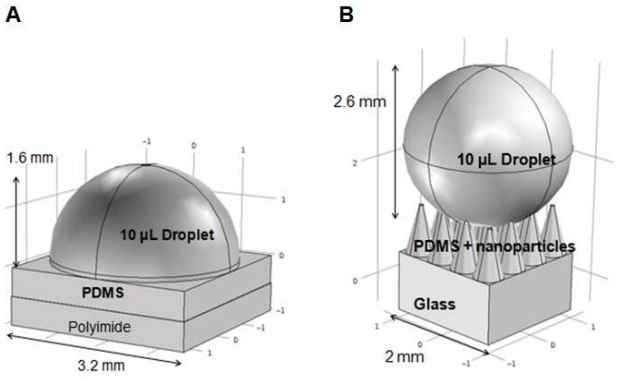

Figure 1.13 Schematic of my experiment for a 10 µL droplet on (A) a hydrophobic surface and (B) a superhydrophobic surface used to synthesize polymers.

1.5 Conclusion

Photopolymerization is a valuable tool for the design and synthesis of novel materials as well as understanding the kinetic of polymerization. The polymers can be prepared under facile reaction conditions using a multitude of photoinitiators and monomers with accessible chain functionalities. The kinetics of photopolymerization can be investigated by studying the rate of polymerization as well as the molecular weights of polymers. The rate of polymerization can be characterized by real-time Raman, real-time FT-IR, NMR, and dilatometry. The molecular weight can be obtained by GPC, Light Scattering, Viscometry, and Mass Spectroscopy.

Superhydrophobic surfaces can be used as substrates during the photopolymerization reaction, due to their water-repellent and low-adhesive properties. These properties of superhydrophobic surfaces reduce the possibility that products will adhere to the surface and so facilitate the analysis of small quantities of materials. A technique to study polymerization kinetics in real time, called micro-dilatometry, will be presented in Chapter 2. The factors limiting the applicability of micro-dilatometry will be discussed in Chapter 3.

Given that the droplets are static and stable such that no mixing or convection occurs within the droplet, the kinetics of polymerization in this unique environment can be carefully studied. The effect of this environment on the ability of growing chain radicals to diffuse and how this, in turn affects termination rates, will be explored in Chapter 4.

Chapter 2. Micro-Dilatometry: A New Method for the Real-Time Monitoring of Polymerization Reactions in Aqueous Droplets

In this chapter, a new technique for monitoring polymerization kinetics in small (~ 10 microliter) aqueous droplets using a contact angle goniometer is presented. This technique, termed micro-dilatometry, can be used to calculate polymerization rates by continuously monitoring the change in droplet volume during the course of a polymerization reaction using a digital image processing system. Adding to the efficacy of the technique is the use of a superhydrophobic surface on which a nearly spherical aqueous droplet is formed. Superhydrophobic surfaces allow for easy removal of the partially polymerized sphere for external characterization. Percent conversion was calculated from volume changes using the contraction factor for polymerization and confirmed using ^{1}H NMR for reactions up to 18% conversion. The use of a temperature and atmosphere controlled environmental chamber was key to maintaining stable solvent volumes by insuring an equilibrium solvent vapor pressure, eliminating extraneous evaporation or condensation of water.

2.1 Introduction

Individual droplets can be used as small volume reactors for chemical or biological compounds and have received much attention because they offer opportunities for precise analysis of products, as well as for the fabrication of valuable new materials.[71,89] Use of droplets streams for micro PCR reactions is especially valuable for analyzing the genetic make-up of cells, where the quantity of available material is limited. [71] One challenge with droplet scale reactions has been the ability to rapidly and accurately monitor reaction processes in real time without affecting the kinetics. Such monitoring would enhance the ability to study and control these reactions as well as to tailor the products synthesized.

Superhydrophobic surfaces offer a unique environment in which to study droplet reactions. Water can form nearly spherical droplets on the superhydrophobic surface and easily roll off at low tilt angles.[74,90] Because of the high surface roughness, the actual contact area between droplet and surface is much lower (<5%) than the apparent liquid-solid contact area. This results in significantly reduced liquid-solid forces allowing droplets to be easily and completely lifted off the surface for further analysis.[85,88,91] Recently, superhydrophobic surfaces have been used to study reactions in individual droplets.[85,88] Fabrication of polymeric particles in 1 ~ 20 μL droplets have been reported. [85,88]

Droplets on a superhydrophobic surface are essentially thermally isolated from the surface because the minimal contact area between droplet and surface increases the effective thermal resistance at the interface.[88] In comparison, droplets on a hydrophobic surface share a large liquid-solid interfacial area and are in good thermal contact the substrate.[76,92,93] Isolated small (~ 10 μL) droplets on a superhydrophobic surface would thus be expected to have a uniform temperature. In addition, there would be no external sheer forces. Hence, when polymerization is performed in an isolated and static monomer droplet on a superhydrophobic surface, several advantages for studying reactions would be realized, including: uniform temperature distribution, no external shear forces (i.e. no mixing), higher purity (no surfactants are required), reduction of waste, and efficient use of precious reactants. However, until now, kinetic studies of reactions within droplets suspended on superhydrophobic surfaces were focused primarily on the evaporation of either pure water droplets[55,95,96] or assemblies of particles inside drying water droplets.[81,96-98] In this paper, we focus our aqueous droplet reaction studies on photopolymerization of a water soluble monomer. To our knowledge, the monitoring of

polymerization reactions within droplets on a superhydrophobic surface has not been previously reported.

Microfluidic systems are common techniques to provide routes to form a stream of individual droplets by the geometric design of microchannels, the consideration of viscosities and densities of immiscible fluids, as well as the control of imposed pressure drops for volumetric flows.[66,70,99-109] Barnes et al.[110] demonstrated that Raman spectroscopy could be used to monitor the real-time kinetics of benzyl methacrylate photopolymerization in a microfluidic device. However, the use of Raman for real-time monitoring of polymerization in a small isolated droplet on a superhydrophobic surface is difficult because of various experimental challenges, including the heating of the droplet by the laser light source which can cause temperature gradients as well as evaporation of water. To overcome this challenge, a novel approach for monitoring polymerization in small droplets is required.

Here, we use a digital contact angle (CA) goniometer to monitor the polymerization kinetics of droplets in a static environment. We name this technique "micro-dilatometry" for the small scale of the reactor (a droplet) and dilatometry which is a technique used to measure volume changes caused by a physical or chemical process, including polymerization. During polymerization, the overall droplet volume decreases as a result of the decreased intermolecular distance between monomer units when monomers react to form a polymer chain. The reduction in volume is monitored using the video system and software of a contact angle goniometer, which calculates the volume of the droplet as a function of time. Droplet volume change is converted to percent conversion of monomer to polymer, thereby yielding polymerization rate information.

Acrylamide was chosen as the monomer in this experiment because it and polyacrylamide are highly soluble in water.[111] Solutions of the monomer and polymer form nearly spherical droplets on superhydrophobic surfaces. In addition, these systems are thoroughly studied and contraction factors are available.[25,112,113] Photoinitiated free radical polymerization was used to convert acrylamide to polyacrylamide to minimize temperature changes and thus avoid complications arising from uncontrolled solvent (i.e. water) evaporation. The photo-initiator 2-hydroxy-2-methyl-1-phenyl-propan-1-one (Darocur 1173) was chosen because its photocleavage does not produce gas.[114,115]

In this chapter, an experimental apparatus and procedure for conducting micro-dilatometry measurements is presented. Techniques for minimizing extraneous evaporation of the droplet, such as temperature uniformity and atmosphere vapor pressure control, are discussed and investigated and the formation of stable droplet volumes is demonstrated. To demonstrate the micro-dilatometry technique, the polymerization conversion rate of acrylamide, dissolved in 10 μL droplets on both hydrophobic and superhydrophobic surfaces, was determined using a temperature-controlled chamber and confirmed by NMR analysis. Results from these experiments will be presented and discussed.

2.2 Experimental Section

2.2.1 Temperature-Controlled Environmental Chamber

A temperature-controlled environmental chamber purchased from ramé-hart (P/N 100-07) was modified for these droplet experiments. The chamber was placed on the sample holder of a ramé-hart contact angle goniometer (Model 250). Figure 2.1 shows a schematic of the temperature-controlled environmental chamber setup. Two parallel widows (A) on the front and

back surfaces of the chamber allowed an external lamp (B) to backlight the droplet in the chamber while the drop profile was monitored using a digital video camera (C) mounted on the opposite side of the chamber. The position of a droplet could be adjusted by the location of the 22 gauge solution dispensing needle (D) as well as by using an externally controlled stage (F), which could translate the chamber height, and thus translate the droplet perpendicular to the optical axis. An additional micrometer (not shown) could translate the internal stage (E) orthogonal to both the light path and the direction controlled by (F). ramé-hart's proprietary DROPimage software was used to measure contact angles as well as the volume of the backlit droplet.

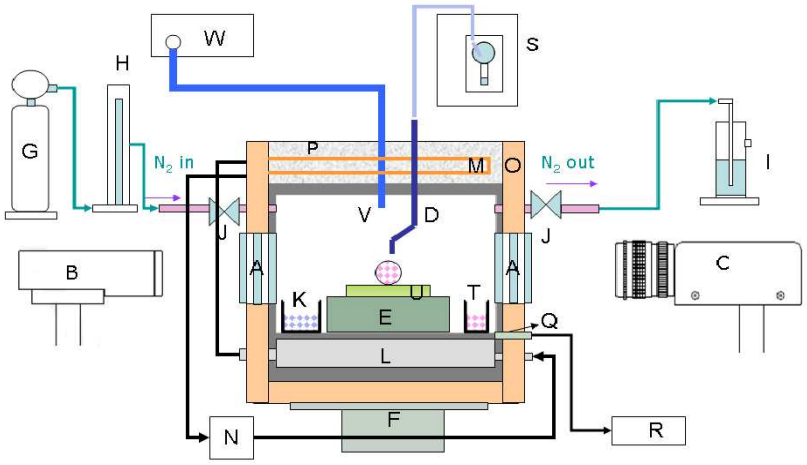

Figure 2.1 Schematic of the temperature-controlled environmental chamber setup. A. windows. B. illuminator. C. digital camera. D. 22 gauge dispensing needle. E. translation stage. F. sample stage. G. nitrogen tank. H. flowmeter. I. bubbler. J. valves. K. solvent for reservoirs. L. base of the chamber. M. upper chiller tube. N. chiller. O. rigid foam insulation. P. polyester fiberfill. Q. thermocouple. R. thermometer. S. automated dispensing system. T. sample source. U. substrate. V. lightguide. W. UV source.

Atmosphere Control

It was critical to control the composition of the atmosphere within the chamber to minimize the presence of oxygen, which would quench radicals, as well as insure a stable and controlled

solvent (i.e. water) vapor pressure. Nitrogen gas (purity: 99.998%) was used to purge oxygen from the chamber. A 1A cylinder of nitrogen gas was regulated to a pressure of 5 psi (G) and the flow rate was controlled with a flowmeter (H) before the gas entered the chamber. Upon exiting the chamber, the nitrogen gas was passed through a bubbler filled with 20 mL of water (I) to create a small backpressure and prevent air ingress. Valves (J) mounted along the input and output tubing paths were used to isolate the chamber, allowing the solvent vapor pressure within the chamber to equilibrate.

By insuring good seals, no leak in the chamber could be detected. Chamber leak rate was monitored using the nitrogen system. When the chamber was purged with nitrogen at a flow rate of 20 mL/min, a valve (J) along the output tubing path was turned off. Then, the flowmeter reading gradually reduced to 0 mL/min, demonstrating that the chamber was well sealed. Measurable nitrogen flow rates indicated leaks which were detected (with soap solution) and sealed before experiments began.

Vapor pressure within the chamber was controlled by placing three reservoirs using 14 mm diameter aluminum caps (K) inside the chamber. These reservoirs were filled with the appropriate solvent, such as pure water or aqueous solutions of acrylamide with the desired concentration. After the nitrogen valves were closed, the solvent vapor pressure within the chamber was allowed to equilibrate over the course of at least 12 hours before droplets were placed on the surface for measurement.

Temperature Control

Uniform temperature of the droplet and all chamber surfaces was necessary to provide not only uniform reaction conditions, but also to insure uniform solvent vapor pressure and to avoid uncontrolled condensation on relatively cool surfaces (such as external chamber walls). A chiller

(Neslab RTE 740, Thermo Scientific) (N) was used to circulate water with the desired temperature (accuracy ± 0.1 ℃). Channels machined into the base of the chamber (L) and a copper tube (M) mounted above the top of the chamber were connected to the chiller to insure a stable and uniform temperature. Rigid foam insulation (O), 2 cm thick, was adhered to the exterior side surfaces of the chamber and polyester fiberfill (P), 6 cm thick, was placed above the top of the chamber within walls created by the rigid foam sidewalls, to keep the thermal stability of chamber to within ± 0.1 ℃. Openings were cut into the rigid insulation to provide optical access to the chamber interior. These openings were covered with glass windows creating a 20 mm air gap to prevent condensation on the interior windows at low temperatures. The temperature of the chamber was monitored using a type K thermocouple (Q) connected to a Fluke model 52 digital thermometer (R) mounted into the chamber base. The temperature of the chamber could be accurately maintained anywhere between 15 and 35 ℃.

Droplet Formation

An automated dispensing system (S) (Part No. 100-22-100, ramé-hart) with a 22 gauge needle (D) was used for controlling the volume of the droplet and delivering the sample to the substrate. The syringe was mounted through a rubber septum inserted into a hole in the top of chamber and connected with Teflon tubing to the computer controlled dispenser. By bending the needle appropriately, it could be rotated within the chamber such that the reactant solution could be withdrawn from the sample source (an 11 mm diameter vial) (T), and then deposited onto the substrate. A typical droplet volume was 10 μL which could be measured to within 0.01 μL using the DROPimage software. The drop was dispensed only after the vapor pressure in the chamber was allowed to stabilize.

UV Illumination

The polymerization reactions under investigation were initiated with UV light. A flexible, 3 mm diameter liquid-filled lightguide (V) was connected to the top of the chamber using a gas-tight machined Teflon fitting. The position of the lightguide over the center of the chamber was 23.9 ± 0.1 mm above the substrate surface (U). The lightguide was connected to a broadband UV spot light source (W) (Bluewave^{TM} 200, Dymax) with an output ranging from 300 - 450 nm. The droplet on the surface was moved into the central area of UV light using the translation stage (E). The UV power was measured using a wide-range power meter (Accu-cal^{TM}-50, Dymax) at the distance between them was 23.9 ± 0.1 mm. A range of UV powers from 0.50 mW/cm^2 to 0.20 mW/cm^2 was used for this study.

2.2.2 Materials

Acrylamide (AAm) (electrophoresis-grade, 99%; Sigma–Aldrich), 2-Hydroxy-2-methyl-1-phenyl-propan-1-one (Darocur 1173; Ciba Specialty Chemicals), and deuterium oxide (Cambridge Isotope Laboratories, Inc.) were all used as received. Milli-Q water (Milli-Q Plus 18.2 Ωcm filter) was used in all instances.

2.2.3 Sample Preparation

For a typical sample preparation, a 1.40 M aqueous acrylamide solution was prepared by dissolving 0.995 g acrylamide in 10.0 mL of Milli-Q water. The photo-initiator, Darocur 1173, was added to 1.40 M acrylamide aqueous solutions with vigorous stirring at room temperature. The solution was stored in a refrigerator at 4 ℃ under air in order to inhibit photodissociation.[24,25,26]

2.2.4 Substrates

Two types of substrates were fabricated: (1) a hydrophobic surface and (2) a superhydrophobic surface. Approximately 20 sample surfaces were required for these experiments.

Smooth and planar films of polydimethyl siloxane (PDMS) (Dow Corning® 3140 RTV) were used as the hydrophobic surface. A doctor blade technique was used to coat the PDMS on a thin 0.05 mm polyimide (PI) film to make a PDMS film that was 0.05 microns thick. These thickness values were chosen to insure mechanical stability and flatness as well as to insure rapid thermal equilibrium with the goniometer stage. The PI film was first cleaned in deionized water and then oven dried at 60 ℃ for 1 hour. To achieve reproducible thickness, two pieces of tape of 0.05 ± 0.01 mm thickness were placed on the film approximately 1 cm apart. PDMS was coated on each PI film and cured at 60 ℃ for 2 hours. Using the goniometer, the contact angle of 10 μL water droplets on these PDMS surfaces ranged from 90 to 96° which is consistent with published values for hydrophobic PDMS surfaces.

Superhydrophobic surfaces were prepared by a 3D printing process[116] which will be briefly summarized here. Glass microscope slides were used as the substrate and were cleaned in deionized water and then oven dried at 60 ℃ for 1 hour before use. PDMS (DAP® 688 clear aquarium silicone sealant, a room temperature vulcanizing hydroxy-terminated dimethyl siloxane, manufactured by Dow Corning) was transferred to a 10mL syringe with 27 gauge steel tip (Nordson EFD). The syringe was connected to an air-powered dispenser (Performus™ V; Nordson EFD) and secured to a desktop robot (JR2000N Series; Janome). To dispense a PDMS post, the robot was brought to a dispense height just above the glass surface. The dispenser was then triggered and the robot was translated vertically up from the surface creating a post with a

"Hershey kiss" or circular base conical shape.[116] The robot was translated 500 μm and the dispense cycle was repeated. Dispense parameters for each dispense event were 55 psi for 155 ms. The position of syringe relative to the glass substrate was adjusted with a high-accuracy CCD micrometer (LS-7601; Keyence).

An array of 21 rows × 21 columns produced a surface area of one square-centimeter. Immediately after printing, the PDMS post arrays were coated with hydrophobic nanoparticles (Cab-O-Sil TS-530; Cabot) using a pipette to dust the area; excess particles were removed. The slide was placed in a 60 ℃ oven and the array was cured for 2 hours. Each PDMS post which formed the superhydrophobic surface was cone-shaped with base diameter 380 ± 20 μm and height 830 ± 20 μm as measured using a Nikon SMZU-15 stereo microscope with an ImagePro image analysis system. The measured contact angle of water on this printed PDMS array ranged from 150 to 155°, which is characteristic of a superhydrophobic surface.

2.2.5 Photopolymerization in the Chamber

To conduct a photopolymerization measurement, the chamber was stabilized at the desired temperature and then 0.5 mL of the monomer solution was transferred to the small sample reservoir (T). The reservoirs used to control the water vapor pressure within the chamber (K) were filled with 3.0 mL of 1.40 M aqueous acrylamide solution without initiator (or other solutions as defined in the results section). The substrate was placed on the aluminum translation stage and the chamber was sealed and purged with N_2 (5 psi., 170 mL/min) for 30 min. The 22 gauge needle was rotated into the sample reservoir and 250 μL of the monomer-initiator solution was withdrawn. Then, the valves of the nitrogen system were turned off. Approximately twelve hours were allowed to elapse to insure that the vapor pressure of water within the chamber reached equilibrium.

After oxygen was excluded and the vapor pressure was at equilibrium, the syringe tip was rotated over the substrate and a 10 μL droplet was dispensed. The needle was rotated out of UV light path, the droplet position was adjusted and the system was focused so that volume measurements could begin. After monitoring volume for 10 min to insure volume stability, the droplet was exposed to the UV light for a specific time. Throughout, the droplet volume was monitored every 12 s using the goniometer. After the specified time, the experiment was stopped. The droplet was picked up with a syringe inserted through a septum in the top of the chamber. In some cases, the droplet was transferred to a NMR tube for further analysis. The syringe tip was then rotated into position and a second droplet was dispensed and the process repeated.

2.2.6 Data Collection from Micro-Dilatometry Technique

Volume and contact angle of each droplet was measured using a contact angle goniometer (Model 250, ramé-hart) with a 400 megapixel digital camera. Backlighting of the droplet provides a two dimensional black and white image that can be automatically tracked with ramé-hart's proprietary DROPimage software. DROPimage software calculations are based on Young-Laplace equations[117] as well as volume equations for a sphere and spherical cap.[118] The surface tension for sessile method was used.

To insure accurate data, the instrument was calibrated using the 4.000 mm diameter steel ball standard supplied with the instrument. A picture of the ball was taken using the camera and displayed in the capture window. The vertical hairline was moved to the center of the ball profile. Two horizontal base lines were moved to the top and the bottom of ball profile, respectively. The vertical and horizontal pixel size and aspect ratio of the sphere were calculated and presented as the calibration value. The minimum resolution of the contact angle of a droplet is ± 1°. The

minimum resolution of height and width of the droplet is ± 0.001 mm. The minimum resolution of the volume measurement is ± 0.01 μL.

Verification of the accuracy of the diameter and volume was obtained using both rigid metal spheres (ball bearings) of known diameter glued to glass slides as well as dispensed water droplets on hydrophobic and superhydrophobic surfaces. The diameters of the three metal spheres were 4.000 mm, 2.500 mm and 1.000 mm. The 4.000 mm and 1.000 mm diameter spheres were supplied by ramé-hart for calibration purposes; the 2.500 mm calibration sphere was purchased separately as it was similar in size to the 10 μL droplets used in experiments on a superhydrophobic surface. After a metal sphere was placed the on the stage of the goniometer, the image was focused, then captured and measured. After refocusing and measuring 10 times, the diameters of the three spheres were measured to be 4.000 ± 0.014 mm, 2.500 ± 0.006 mm and 1.000 ± 0.003 mm, respectively. These results demonstrate that the image processing system can measure the diameter of spherical objects accurately and with good precision. Precision of the system itself was 0.001 mm, as determined from multiple measurements of the same sphere without refocusing. Decreased precision, reflected in the above diameter values, resulted in variations due to refocusing.

Two experiments were conducted to determine the accuracy and precision of the measurement of aqueous droplets in this system. In the first experiment, the volume of droplets (1.40 M acrylamide), with a nominal dispense volume of 10.00 μL, on a hydrophobic and superhydrophobic surface in an environmental chamber with controlled humidity (vapor pressure equilibrated with 1.40 M acrylamide reservoirs) was determined to be 10.35 ± 0.06 μL and 10.08 ± 0.04 μL, respectively. These values are the average and standard deviation values derived from the measurement of 10 different droplets and include errors/variations associated with: the

dispensing system and partial occlusion of the liquid-solid interface. The droplets were placed in the exact same location and refocusing was not necessary. The accuracy of the volume measurement of a droplet on a hydrophobic surface is lower than in a droplet on a superhydrophobic surface because the liquid-solid contact line can be partially occluded by the substrate. However, precision values for water on these two surfaces are comparable to the precision for steel spheres, and so are sufficient for measuring 0.01 μL changes in volume.

A second measurement experiment was conducted with pure water where the system was refocused using 10 different droplets exposed to air. The refocusing and measuring process were finished within 5 s, and the volume of the droplet may have evaporated by 0.008 μL via calculation. After refocusing the imaging system, the volume of the water droplets on a hydrophobic and superhydrophobic surface was determined to be 10.54 ± 0.08 μL and 10.17 ± 0.06 μL, respectively.

Refocusing is the greatest source of error for both the accuracy and precision of the volume measurement for both standard spheres and aqueous droplets. It causes far more variability than that observed from the dispensing equipment. For example, on a superhydrophobic surface the values are 10.17 ± 0.06 μL and 10.08 ± 0.04 μL, for refocusing and dispensing, respectively. When the imaging system is used to measure changes in the volume of a single droplet, the precision is better than ± 0.01 μL Details of the calibration process are in Appendix I.

In all cases, after a droplet was placed on a surface, images of the droplet were digitized every 12 s and the volume, the contact angle, the height and the width of the droplet were recorded.

2.2.7 Kinetic Equations for Photo-Free Radical Polymerization

The degree of polymerization as a function of the volume change was determined with Eq. 2.1.[119]

$$\frac{\Delta[M]}{[M]} = \frac{(\frac{\Delta V}{V_o})}{C_f \times d_M} \tag{2.1}$$

where Δ [*M*] is the incremental change in monomer concentration [*M*] , *ΔV* is the change in volume from the initial volume of acrylamide, V_o, C_f is the contraction factor and d_M is the density of pure monomer. In the literature,[25,112,113] C_f for acrylamide was reported as 0.22 cm^3/g when the polymerization temperature was between 25 ℃ and 50 ℃. The contraction factor[25] C_f was determined using the Eq. 2.2.

$$C_f = \frac{1}{d_M} - \frac{1}{d_p} \tag{2.2}$$

where d_M and d_P are the densities of pure monomer (1.13 g/cm^3) and polymer (1.50 g/cm^3), respectively.

An initial droplet volume of approximately 10 μL, measured to an accuracy of ± 0.01 μL was used for the experiments. For a 10 μL 1.40 M acrylamide droplet, the volume of pure acrylamide would be 0.88 μL. Hence, when the volume of a droplet decreased by 0.01 μL (the minimum volume resolution of the instrument), the overall droplet volume changed by 0.10% and then monomer conversion to polymer was calculated to be (0.01 μL/0.88 μL)/(0.22 cm^3/g × 1.13 g/cm^3) or 4.5% using Eq. 2.1. Similarly, at 100% conversion, the overall theoretical volume shrinkage would be 2.18% based on the original volume. Therefore, the polymerization can be assumed to be finished after droplet volume shrinks to 97.82% of its original volume.

2.2.8 NMR Spectroscopy

The ^{1}H NMR spectra were obtained on a Varian NMRS 600MHz spectrometer at room temperature. A 10 μL droplet was completely dissolved in 0.6 mL deuterium oxide and tetramethylsilane was used as the chemical shift reference. Proton spectra were acquired at 599.94 MHz, using 32 k data points, spectral width 8 ppm, relaxation delay 30 s, acquisition time 2.05 s, pulse width 90° and 32 scans. The relaxation delay was set to 30 s to allow the spins to return to equilibrium and prepare the sample for subsequent pulses. The acquisition time of 2.05 s was found to be sufficiently long to allow the free induction decay (FID) to decay and avoid truncation errors and to ensure full spectral resolution. The pulse-repetition time, 32.05 s (relaxation delay + acquisition time) was found to be sufficiently long to allow adequate spin-lattice relaxation time between repeated scans.

2.3 Results and Discussion

2.3.1 Effect of Nitrogen Flow Rate

Since the volumetric shrinkage of the droplet is used to track the polymerization rate, the stability of the droplet volume, before polymerization, is essential. One influencing factor for droplet volume change is the flow rate of nitrogen. A nitrogen purge is important as oxygen can scavenge the photo-generated radicals, resulting in a long induction period where no polymerization would occur. However, if the flow rate of nitrogen was too high, the droplet would evaporate rapidly as water vapor would be continuously purged by the flowing nitrogen. As a result, the shrinkage from monomer conversion would be masked by this evaporation phenomenon.

The effect of nitrogen flow rate on a 10 μL droplet of pure water on a superhydrophobic surface, with pure water in the reservoirs, is shown in Fig. 2.2. The water droplet was observed to shrink at all nitrogen flow rates with the greatest shrinkage occurring at the highest flow rate. For example, after 600 s, the droplet shrank to 97.33% of its original volume at 50 cc/min, whereas at a flow rate of 350 cc/min, the droplet shrank to 93.67% of its volume. After turning off the nitrogen valves and waiting for 30 min, the volume of a droplet was relatively stable decreasing by about 0.1% per 200 s. The results indicate that equilibrium between evaporation and condensation was gradually achieved after the nitrogen valves were turned off for 30 min.

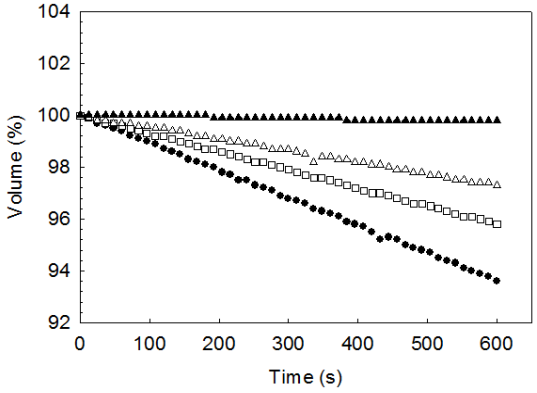

Figure 2.2 The effects of nitrogen flow rate on the volume of a 10 μL water droplet on superhydrophobic surface at 25 ℃. The flow rate is (●) 350 cc/min. (□)170 cc/min. (Δ) 50 cc/min. and (▲) 0 cc/min (after valves had been turned off for 30 min).

2.3.2 Effect of Reservoir Composition

In the closed system, the solvent in the reservoirs gradually evaporates until the vapor pressure of the solvent (water) reaches equilibrium. During this process, the droplet would tend to swell or shrink, depending upon the relative concentration of solvent in the droplet and the reservoir. Therefore, to stabilize the droplet volume, the composition of the reservoirs and the droplet should be the same. Figure 2.3 shows the effect of reservoir and droplet compositions on droplet volume change. Pure water and 6.0 M acrylamide solutions were used for the droplet or

the reservoir or both. In all cases, the initial 10 μL droplet was placed on a superhydrophobic surface at 25 ℃; 1 hour was allowed to insure equilibrium vapor pressure was established after the nitrogen valves were turned off.

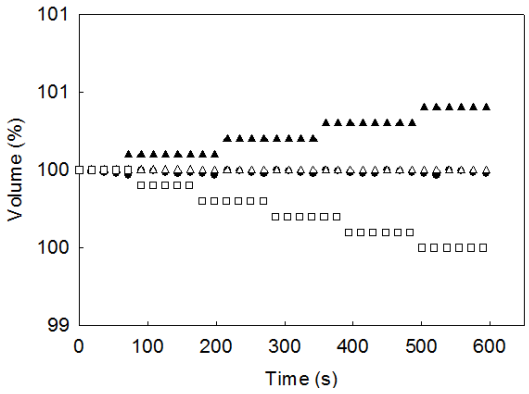

Figure 2.3 The volume of a 10 μL droplet as a function of time using either water or 6.0 M acrylamide solutions as droplet and/or reservoir. Droplets were placed on a superhydrophobic surface at 25 ℃. The chamber was allowed to equilibrate for 1 hour before droplets were dispensed. (▲) 6.0 M acrylamide droplet with water reservoir. (●) 6.0 M acrylamide droplet with 6.0 M acrylamide reservoir. (Δ) Water droplet with water reservoir. (□) Water droplet with 6.0 M acrylamide reservoir.

Clear differences in droplet volume stability were observed depending upon the relative compositions of the droplet and reservoirs as shown in Fig. 2.3. When the composition of the reservoirs and the droplet were the same (either both water or both 6.0 M acrylamide), the volume of the droplet was stable (<0.10% change after 600 s). When the reservoirs were filled with water and the droplet was an aqueous acrylamide solution, the volume of the droplet increased with time because the vapor from the water reservoirs would condense on and dilute the droplet as predicated by Raoult's Law (the vapor pressure of water and acrylamide[120] at 25 ℃ are 24 mmHg and 0.007 mmHg, respectively). The volume of the 6.0 M acrylamide droplet increased 0.40% after 600 s. When the solutions were reversed and a water droplet was measured in the presence of reservoirs filled with aqueous acrylamide solution, the volume of the droplet

decreased 0.70% after 600 s as the water vapor from the droplet condensed into the reservoirs. Similar results were observed with lower acrylamide concentrations, however, the rate of volume change was slower. Therefore, to insure stable droplet volumes, the solution concentration in the reservoirs should match the droplet composition.

2.3.3 Effect of Temperature Uniformity

Temperature is an important factor for the stability of the droplet volume because the temperature affects the vapor pressure of solvent. Chamber walls (or windows) that are cooler than the droplet will lead to droplet evaporation with condensation occurring on the cooler walls. To insure temperature uniformity, the chamber was thermally isolated from the environment (rigid foam side panels and polyester fiberfill top) and water, controlled to within ± 0.1 ℃, was circulated through the base of the chamber and a copper coil placed on top of the chamber, within the upper fiberfill insulation.

Without the insulation and liquid coolant, the droplet volume shrank by 1.95% within the first 600 s after the droplet was placed on the surface as shown in Table 2.1. When the chamber was partially insulated, the droplet volume shrank by 1.62 volume % at 25 ℃. However, when the chamber was properly insulated and cooled with the chiller, stable droplet volumes could be maintained at any temperature attempted, ranging from 15 to 35 ℃ as shown in Table 2.1. On average, droplets of 1.40 M acrylamide solution dispensed on a superhydrophobic surface decrease by 0.17 ± 0.05 volume % after 600 s over this temperature range.

2.3.4 Monitoring Droplet Polymerization: Hydrophobic Surfaces

On a hydrophobic surface, a droplet of 1.40 M acrylamide with 0.003 M Darocur 1173 forms a nearly hemispherical droplet with a static contact angle of 95°; a value which is

comparable for that measured for pure water. Figure 2.4 shows an image of a 9.50 μL droplet of this monomer solution on a hydrophobic PDMS surface under UV irradiation (0.30 mW/cm^2) at 25 ℃ after 6 s (A) and 300 s (B). After UV exposure, the droplet shape remains similar as the droplet CA remains within 1° and the liquid-solid contact diameter remains within 0.001 mm of the original droplet values. What does change upon monomer polymerization is the droplet height, decreasing by 0.013 mm (~1%). The relatively strong solid-liquid interactions between the solution and this hydrophobic surface account for the pinning of the solid-liquid-gas triple contact line (TCL) resulting in contraction only in the height and not in the width (i.e. diameter) of the droplet during polymerization induced shrinkage.

Table 2.1 The effect of chamber thermal insulation on the volume stability of a 10 μL droplet 600 s after placement with the environmental chamber controlled to different temperatures.

Temperature (^{o}C)	Droplet volume change 600 s after droplet placement (%)		
	Chamber (not insulated)	Partially Insulated Chamber	Fully Insulated Chamber
15	-	1.81	0.10
20	-	2.18	0.24
25	1.95	1.62	0.18
30	-	1.52	0.19
35	-	1.08	0.14

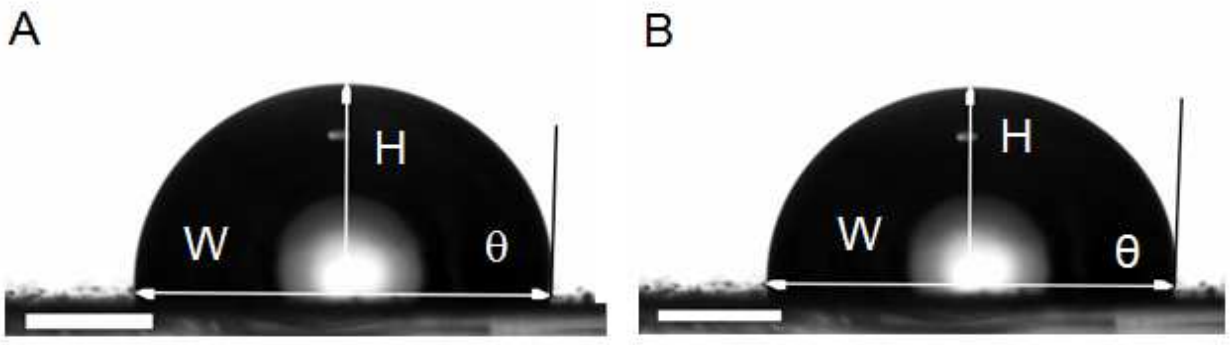

Figure 2.4 Optical images of a aqueous droplet (1.40 M acrylamide with 0.003 M Darocur 1173) on hydrophobic surface under UV light (0.30 mW/cm^2) at 25 ℃ (A) after 6 s (CA: 95°, height H: 1.568 mm and width W: 3.377 mm) and (B) after 300 s (CA: 94°, height H: 1.555 mm and width W: 3.376 mm). Scale bar = 1 mm.

Plots of the percent volume change and calculated percent conversion of monomer as a function of exposure time are shown in Fig. 2.5 for this 9.50 µL droplet. As can be seen, due to the polymerization reaction, the shrinkage occurs linearly with time and begins as soon as the UV light is turned on. Control experiments (not shown) confirm that when initiator is not added to the aqueous monomer droplet, shrinkage is less than ± 0.01 µL after the UV light is turned on. The calculated volume change for the droplet after 300 s UV exposure was 1.49%. This shrinkage correlates to a 60% conversion of monomer to polymer.

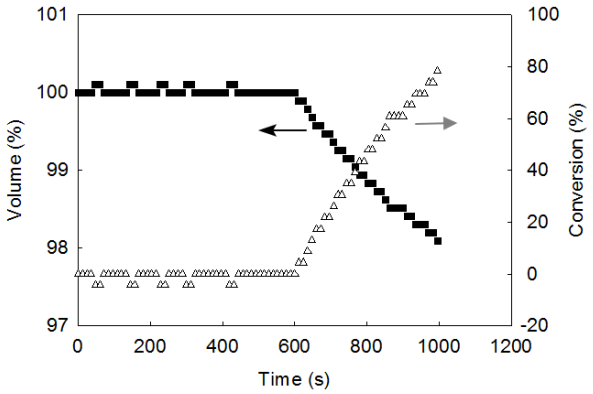

Figure 2.5 The percent volume change (■) and percent monomer conversion (△) of a droplet with 0.003 M Darocur 1173 on hydrophobic surface at 25 ℃. UV light (0.30 mW/cm^2) was turned on at 600 s.

To independently confirm the percent conversion of monomer to polymer, ^{1}H NMR was used to determine the percent monomer conversion within the droplet. The ratio of acrylamide to polyacrylamide was obtained by quantifying the peak areas specific to acrylamide (vinyl group protons 5.60 - 6.52 ppm) and polyacrylamide (aliphatic protons 1.22 - 2.40 ppm) in the ^{1}H NMR[121,122] as shown in Fig. 2.6. Based on the quantifying the peak areas in Fig 2.6a, the ratio of proton number between CH of acrylamide (6.12 - 6.30 ppm), CH_2 of acrylamide (6.00 - 6.12 ppm), and CH_2 of acrylamide (5.60 - 5.82 ppm) is 1 (32.78): 1 (33.14): 1 (34.09). The ratio of proton number between aliphatic CH of polyacrylamide (2.00 – 2.40 ppm), and aliphatic CH_2 of

polyacrylamide (1.22 – 1.80 ppm) is 1 (32.99): 2 (67.01) and shown in Fig. 2.6b. The accuracy of the calculated conversion from monomer to polymer via ^{1}H NMR is ± 1%. While the resolution of the total volume of a 10 µL droplet is ± 0.01 µL (0.1%) using the goniometer, the accuracy of the calculated monomer conversion from the droplet volume shrinkage is ± 4.5% due to the small volume changes measured (0.01 µL) and the 0.22 cm^3/g contraction factor.

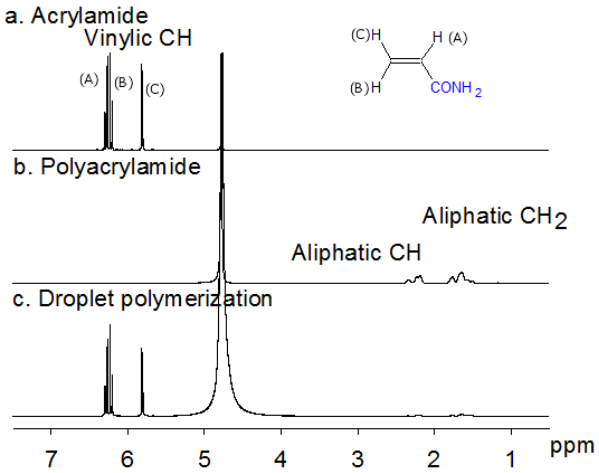

Figure 2.6 Typical ^{1}H-NMR spectrum of (a) acrylamide, (b) polyacrylamide and (c) 10 µL 1.40 M acrylamide droplet, with 0.003 M Darocur 1173 after 18% conversion to polymer on a hydrophobic surface under UV 0.30 mW/cm^2 for 105 s at 25 ℃.

The percent conversion of acrylamide to polyacrylamide, as determined by both micro-dilatometry and NMR, are shown in Table 2.2 for 10 µL droplets on a hydrophobic surface. The polymerization reaction was stopped at 5%, 9% or 18% conversion to insure adequate conversion for NMR analysis while preventing the droplet from adhering strongly to the hydrophobic substrate. Most kinetic studies of photo-free radical polymerization in the literature were limited to low conversion, typically ≤10% conversion, to maintain relatively constant monomer concentration and avoid significant viscosity changes.[123,124] Reaction in droplets were carried out to 5%, 9% and 18% in this work to insure compatibility with kinetics studies,

estimate the high range for % conversion, as well as synthesize sufficient amount of polymer for NMR analysis.

Table 2.2 Correlation between NMR and Micro-Dilatometry measurements for 10 μL droplets on a hydrophobic surface. (1.40 M acrylamide in DI water, UV power: 0.30 mW/cm^2). Reported UV exposure times and % conversion by NMR are averages of three experiments per condition except for 0.01 M 1173 in which only two samples were analyzed. All NMR values agree to within ± 1%.

Initiator [1173] (mole/L)	UV exposure Time (s)	Conversion from ^{1}H NMR (%)	Conversion from Micro-dilatometry (%)	Difference (%)
0.0005	215 ± 6	16± 1	18	-2
0.001	155 ± 3	17± 1	18	-1
0.003	32 ± 4	4± 1	5	-1
0.003	65 ± 3	8± 1	9	-1
0.003	105 ± 4	18± 1	18	0
0.005	99 ± 11	17± 1	18	-1
0.01	69 ± 1	17± 1	18	-1
0.01[(a)]	58 ± 4	18± 1	18	0

(a) UV exposure time value is for UV power at 0.5 mW/cm^2.

As can be seen in Table 2.2, the correlation between NMR and micro-dilatometry is excellent with the % difference ranging from 0 to 3%, which is within the experimental error of the dilatometry experiment (4.5%). As the concentration of Darocur 1173 increased from 0.0005 M to 0.01 M, the time to achieve 18% conversion decreased from 215 s to 69 s. Increasing the UV power density from 0.30 mW/cm^2 to 0.50 mW/cm^2 for droplets with 0.01 M 1173 resulted in a reduction of time to achieve 18% conversion from 69 to 58 s with no significant difference in accuracy (17 vs 18% respectively via NMR). Accuracy at a lower conversion of 5% (0.003 M initiator), achieved using shorter UV exposure times, was comparable to experiments run to 18% conversion. These results indicate that the micro-dilatometry technique can be used to study

photoinitiated free-radical polymerization reaction on a hydrophobic surface at conversions ranging from 5 to 18%.

2.3.5 Monitoring Droplet Polymerization: Superhydrophobic Surfaces

On a superhydrophobic surface, 10 μL of the 1.40 M aqueous monomer solution forms a nearly spherical droplet due to weak liquid-solid interactions. The contact angle of a droplet on the surface is 153° as shown in an optical microscope image in Fig. 2.7A. Under UV irradiation, the droplet maintains its nearly spherical shape as it contracts uniformly in both diameter and height. The contact angle remains constant within the measurement error. Images of a 10.40 μL droplet of monomer solution (1.40 M acrylamide with 0.003 M Darocur 1173) are shown in Fig. 2.7 after 6s (B) and 180 s (C) of UV radiation (0.20 mW/cm^2 at 25 ℃). The droplet decreased by 0.006 mm in both height and width but the CA remains essentially unchanged (151°). The volume change of the droplet in Fig. 2.7C was 1.24% and the percent conversion was calculated to be 50%.

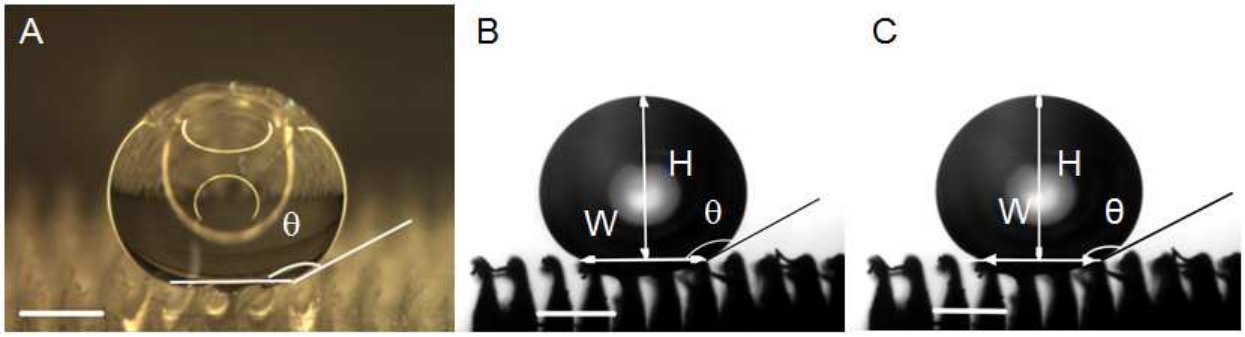

Figure 2.7 Optical images of a droplet containing 1.40 M acrylamide with 0.003 M Darocur 1173 on superhydrophobic surface at 25 ℃ (A) Stereo-microscope (∠θ = 153°) without UV exposure, (B) Goniometer: under UV 0.20 mW/cm^2 exposure after 6 s (measured angle θ: 151°, height H: 2.249 mm and width W: 1.767 mm) and (C) after 180 s. (measured angle θ: 151°, height H: 2.243 mm and width W: 1.761 mm). Scale bar = 1 mm.

Plots of the percent change in droplet volume and the calculated % conversion change with exposure time are shown in Fig. 2.8. As can be seen in this Fig. 2.8, the shrinkage due to the polymerization reaction occurred linearly with time and began as soon as the UV light was turned on. As with a droplet on a hydrophobic surface, when no initiator is added to the aqueous monomer solution, shrinkage was less than 0.01 μL when the UV light was turned on.

The relatively weak solid-liquid interactions enable the droplet to keep its spherical shape as shrinkage occurs during the polymerization reaction. The width and height shrink uniformly and the CA maintains a value greater than 150°. Maintenance of a spherical shape is consistent with studies of the evaporation of water droplets on superhydrophobic surfaces.[55,95]

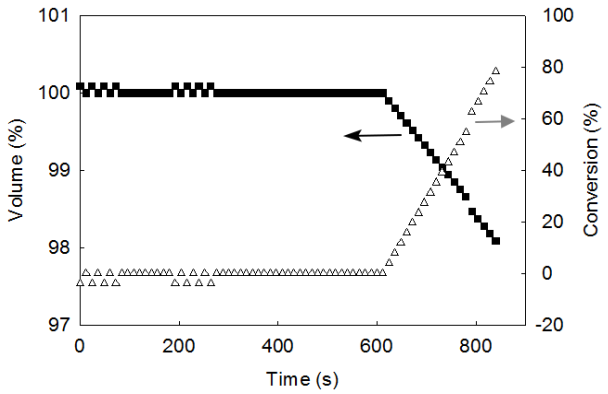

Figure 2.8 The percent volume change (■) and percent conversion (△) of a 10.40 μL monomer solution droplet (1.40 M acrylamide with 0.003 M Darocur 1173) on superhydrophobic surface at 25 ℃. UV 0.20 mW/cm^2 was turned on at 600 s.

Table 2.3 shows the percent monomer conversion to polymer as measured by both micro-dilatometry and NMR. The reaction was stopped when shrinkage corresponding to 5%, 9%, or 18% conversion as observed by micro-dilatometry. The droplets were then easily removed and analyzed by NMR. Percent conversion values agree to within 1% conversion across a range of initiator concentrations, reaction times, UV power levels and percent conversion values. The experiments conducted with solutions containing 0.003M of initiator (highlighted in Table 2.2)

demonstrate that the micro-dilatometry technique provides an accurate measurement of % conversion over the range from 5 to 18% conversion. Compared with Table 2.2, the polymerization rate in the droplet on a superhydrophobic surface is about 11% faster than on a hydrophobic surface.

One added advantage of using a superhydrophobic surface is that the partially polymerized droplet can be easily and completely removed from the chamber for external analysis without any loss of sample. As shown in Fig. 2.9, a droplet can be completely removed after 18% conversion. No fluid was observed on the surface after droplet removal. Removal of droplets from a hydrophobic surface was more problematic. In order to transfer a polymer droplet from a hydrophobic surface to a NMR tube, most of the droplet could be withdrawn using a syringe, but then the remaining polymer on the surface needed to be washed several times using D_2O.

Table 2.3. Correlation between NMR and Micro-Dilatometry measurements at 18% conversion for 10 μL droplets on a superhydrophobic surface. (1.40 M acrylamide in DI water, UV power: 0.30 mW/cm^2). Reported UV exposure times and % conversion by NMR are averages of three experiments per condition.

Initiator [1173] (mole/L)	UV exposure Time (s)	Conversion from ^{1}H NMR (%)	Conversion from Micro-dilatometry (%)	Difference (%)
0.0005	189 ± 3	17± 1	18	-1
0.001	142 ± 2	17± 1	18	-1
0.003	25 ± 2	5± 1	5	0
0.003	48 ± 2	9± 1	9	0
0.003	97 ± 3	17± 1	18	-1
0.005	85 ± 6	18± 1	18	0
0.01[(a)]	60 ± 1	17± 1	18	-1
0.01[(b)]	53 ± 4	17± 1	18	-1

(a) UV exposure time value is for UV power at 0.25 mW/cm^2.
(b) UV exposure time value is for UV power at 0.50 mW/cm^2.

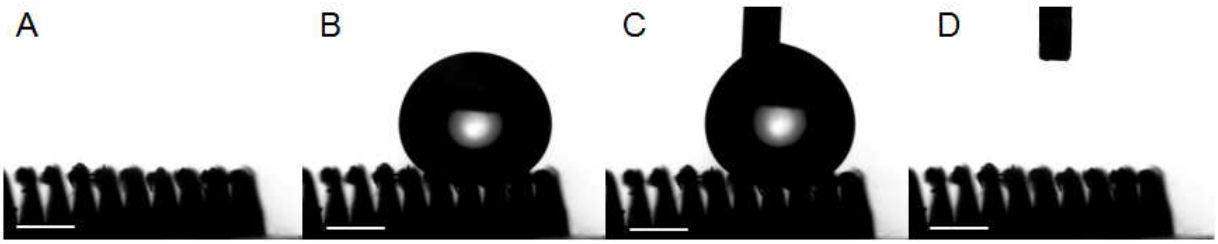

Figure 2.9. Image illustrating the dispensing and removal of a droplet on a superhydrophobic surface. (A) Original superhydrophobic surface. (B) Droplet after 18% conversion polymerization. (C) Droplet withdrawn into syringe. (D) After droplet removal.

2.4 Conclusion

A novel technique, micro-dilatometry, is described for monitoring the kinetics of a photo-initiated free radical polymerization reaction in small, 10 μL, droplets. By using a carefully insulated environmental chamber and by insuring the vapor pressure of the chamber is in equilibrium with the droplet, volume changes as small as 0.01 μL could be accurately measured in real time. Percent monomer conversion, ranging from 5% to 18%, could be measured to within ± 1% by micro-dilatometry as verified by NMR. Reactions on two surfaces: (1) a smooth hydrophobic PDMS surface which supported a hemispherical drop and (2) a superhydrophobic surface which supported a nearly spherical drop could be studied with comparable accuracy. The polymerized spherical droplet on a superhydrophobic surface was easy to completely remove for further analysis of physical and chemical properties, such as NMR and GPC. Thus, the micro-dilatometry technique, used with a superhydrophobic surface, is especially well suited for kinetic studies in small droplets when the amount of available monomers, or initiators are limited. It is also advantages as the environmental conditions can be carefully controlled. Furthermore, contact with a surfactants and/or oil can be completely avoided, unlike droplet polymerization reactions conducted by emulsion polymerization or in microfluidic environments.

On a hydrophobic surface, washing was required to complete recover all of the polymer synthesized. However, when hydrophobic surfaces are used, micro-dilatometry is not limited to aqueous reactions. Future work will investigate polymerization reactions in droplets with non-aqueous solvents on appropriate hydrophobic surfaces as a function of environmental conditions.

Chapter 3. Limits of Micro-Dilatometry: High Percent Conversions

In chapter 2, micro-dilatometry was shown to be an accurate technique for monitoring the progress of polymerization reactions in droplets. Good agreement was demonstrated for polymerization of acrylamide to polyacrylamide over the range from 5 to 18% conversion as measured by micro-dilatometry and NMR. However, deviations in percent conversion were observed for these two techniques at percent conversions above 18%. In this chapter, the deviation between micro-dilatometry and NMR results will be quantified and explanations for the differences will be discussed in detail. In addition, the effect of surface type (hydrophobic vs superhydrophobic) on the quality of microcalorimetry measurements will be presented.

3.1 Results and Discussion

3.1.1 The Polymerization in Droplets Beyond 18% Conversion

In the previous chapter, the efficacy of micro-dilatometry for monomer conversions $\leqq$ 18% was demonstrated. In order to determine the limitations of the micro-dilatometry technique, photopolymerization of monomer solution droplets was performed to high percent conversions. Plots of the percent volume change and calculated percent conversion of monomer as a function of time for a 9.51 μL droplet of 1.40 M aqueous acrylamide solution with 0.003 M Darocur 1173 at 25 ℃ on a superhydrophobic surface are shown in Fig. 3.1. The UV light (0.20 mW/cm^2) was turned on after 600 s and off at 1330 s. Before UV illumination, the droplet was stable in the chamber (average rate of volume percent change = 1.51×10^{-6} s^{-1}). During illumination, the droplet volume decreased linearly, at first, followed by a slowing of the shrinkage rate. After the UV illumination was turned-off (1330 s), the droplet continued to shrink, but at a significantly slower rate during the subsequent 300 s with a volume percent shrinkage rate of -5.11×10^{-4} s^{-1}.

Based on the measured volume change of the droplet, the conversion of monomer would need to be 127% after 730 s of total illumination to solely account for the shrinkage.

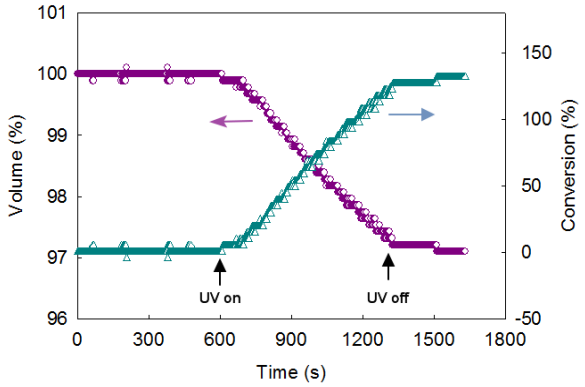

Figure 3.1 The volume change (◯) and conversion change (△) of 9.51 μL 1.40 M acrylamide with 0.003 M Darocur 1173 on superhydrophobic surface at 25 ℃ UV (0.20 mW/cm^2) was turned on at 600 s and turned off at 1330 s.

Given the large volume change, the conversion of monomer to polymer cannot be the sole mechanism by which the droplet shrinks during these long exposure times. Extraneous evaporation of the solvent (i.e. water) must also be occurring. The objective of this chapter is to determine the mechanism(s) for solvent evaporation at long reaction times. Two possible mechanisms are explored: (1) excess heat from the exothermic polymerization reaction is dissipated by evaporation of water and (2) the vapor pressure of the water in the droplet increases relative to the vapor pressure in the reservoirs during the course of the reaction as the total number of molecules in the droplet decreases during the polymerization reaction.

3.1.2 Comparison Between Micro-Dilatometry and NMR Above 18% Conversion

The effect of UV exposure time on the extent of polymerization in droplets on a superhydrophobic and hydrophobic surface was studied and the results summarized in Table 3.1 and Fig. 3.2. All reactions contained the same initiator concentration (0.003 M Darocur 1173) and were exposed to 0.20 mW/cm^2 of UV light. After irradiation, the percent monomer

conversion was calculated by micro-dilatometry and measured by NMR analysis (Tables 3.1). The percent conversion obtained from micro-dilatometry is found to be equivalent to the correspondent values obtained from NMR analyses when conversion is at 18% or below for both surface environments. At higher percent conversions, the deviation between micro-dilatometry and NMR results diverge, with the difference between the two techniques increasing with increasing polymerization time.

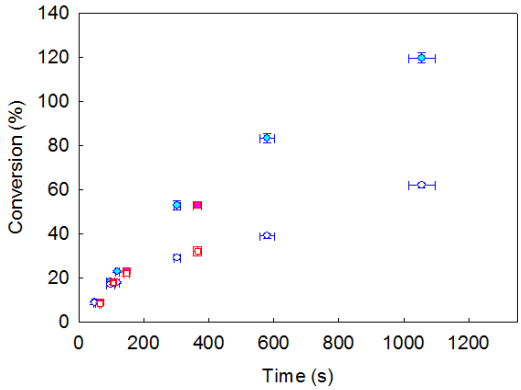

Figure 3.2 The conversion of 10 μL 1.40 M acrylamide droplets under UV 0.20 mW/cm^2 at 25 °C. (●) Micro-dilatometry and (○) NMR data for a droplet on a superhydrophobic surface. (■) Micro-dilatometry and (□) NMR data for a droplet on a hydrophobic surface.

Overall, the trends for hydrophobic and superhydrophobic surfaces are similar. At 18% conversion, both surfaces yield good correlation between micro-dilatometry and NMR results. At ~30% conversion (~330 s), both surfaces show a significant disparity between micro-dilatometry and NMR with an average difference of -21% and -24% respectively which is within the experimental error of the micro-dilatometry measurement. At intermediate conversions (~22%) the difference between the two surface types is somewhat more pronounced with an average difference of -1% and -5% for the hydrophobic and superhydrophobic surfaces, respectively. These differences are still within the experimental error for micro-dilatometry of 4.5%, but may reflect a small additional solvent loss on the superhydrophobic surface.

Table 3.1 The conversion of polymerization in 10 μL 1.40 M acrylamide droplet with 0.003 M Darocur 1173 on a superhydrophobic (SH) and hydrophobic surface (H) under UV 0.20 mW/cm^2.

Surface	UV exposure Time (s)	Conversion from ^{1}H NMR (%)	Conversion from Micro-dilatometry (%)	Difference (%)
SH	46	9	9	0
SH	48	8	9	-1
SH	50	9	9	0
SH	94	17	18	-1
SH	96	17	18	-1
SH	100	18	18	0
SH	112	18	23	-5
SH	120	18	23	-5
SH	122	19	23	-4
SH	292	28	50	-22
SH	300	30	55	-25
SH	302	29	53	-24
SH	314	30	53	-27
SH	560	40	85	-45
SH	582	39	81	-42
SH	600	38	84	-46
SH	1020	61	117	-56
SH	1050	62	121	-59
SH	1100	63	121	-58
H	62	7	9	-2
H	66	8	9	-1
H	68	8	9	-1
H	102	17	18	-2
H	104	18	18	0
H	110	18	18	0
H	138	21	23	-2
H	146	22	23	-1
H	154	23	23	0
H	352	30	53	-23
H	364	32	53	-21
H	378	34	53	-19

At longer reaction times, the percent conversion values obtained by micro-dilatometry were significantly higher than those determined by NMR as shown in Table 3.1 and Fig. 3.2. The disparity between these two techniques increased as the percent conversion increased. After the polymerization in a droplet on a superhydrophobic surface for 300 s, micro-dilatometry results

measured sufficient shrinkage to account for 53% conversion, whereas NMR measured only 29% for a difference of 24%. However, after 1060 s, micro-dilatometry results measured sufficient shrinkage to account for 120% conversion of monomer to polymer whereas NMR measured a 61% conversion for a difference of almost 60%. These longer term experiments were not conducted on hydrophobic surfaces due to the difficulty in removing the extensively cured droplets from the surface. Since the measurement accuracy of micro-dilatometry would not account for these large disparities, mechanisms which could explain excess evaporation were investigated.

3.1.3 Heat Generation and Dissipation in Droplets: Effect of the Substrate

The micro-dilatometry technique used with the superhydrophobic surface is highly suited for kinetic studies due to easy withdrawal of the products for further analysis (e.g. NMR and GPC). However, the superhydrophobic surface is highly thermally insulating and so the heat generated within an aqueous droplet during the exothermic polymerization reaction on the superhydrophobic surface cannot be conducted easily into the substrate. The heat within the droplet on the superhydrophobic surface could accumulate and cause an increase in temperature which accelerates evaporation of the solvent.

In order to understand how the heat of polymerization influences droplet volume on a superhydrophobic surface, the temperature of a 10 μL 1.40 M acrylamide droplet with and without 0.003 M Darocur 1173 under UV (0.20 mW/cm^2) illumination was monitored (Fig. 3.3). Without initiator, the temperature of a 10 μL droplet of 1.40 M acrylamide remained stable. This result is consistent with the observation, discussed in the previous chapter, that a 10 μL droplet of 1.40 M acrylamide solution (no initiator) under the same UV power for 30 min shows no

decrease in volume. Thus, UV light is not significantly absorbed by the droplet or substrate and does not cause the monomer to polymerize or the solvent to evaporate.

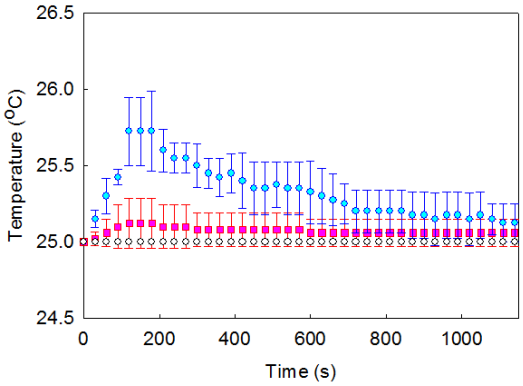

Figure 3.3 The temperature of a 10 µL 1.40 M acrylamide droplet under UV 0.20 mW/cm^2 for 1200 s at 25 ℃. (◯) a droplet without Darocur 1173. (●) a droplet with 0.003 M Darocur 1173 on a superhydrophobic surface. (■) a droplet with 0.003 M Darocur 1173 on a hydrophobic surface.

Upon addition of the photoinitiator, a small increase in the temperature of the droplet can be observed. In Fig. 3.3, the maximum temperature of a 10 µL droplet of monomer solution with 0.003 M Darocur 1173 increased by 0.7 ℃ and 0.1 ℃ on a superhydrophobic and hydrophobic surface during UV illumination, respectively. This indicates the heat of polymerization is responsible for the small temperature increase in the droplet. The magnitude of the measured temperature increase may not represent all the heat released by the polymerization reaction as some heat would be expected to be transferred to the thermocouple (0.25 mm diameter stainless steel), nitrogen environment, the substrate, and the ambient via evaporation. Evaporation of water, caused by the heat of polymerization, would lead to droplet shrinkage as well as a decrease in the measured temperature of the droplet due to the highly endothermic heat of vaporization of water (2444 J/g at 25 ℃).

For a thermally adiabatic system, the high enthalpy of polymerization for acrylamide[125,126] (ΔH_p = 81.6 kJ/mol) would lead the 10 μL 1.40 M acrylamide droplet to release 1.14 J of heat after 100% conversion of monomer to polymer. If 100% of this heat was dissipated by evaporation, the volume of the droplet would decrease by 0.47 μL (4.7 volume %), which would generate 212% pseudo-conversion in order to carry away all heat.

At 18% conversion, if all the heat generated by polymerization (0.21 J) was dissipated by evaporation, then the volume change would be 0.084 μL. If this volume change indeed occurred, then micro-dilatometry would detect shrinkage equivalent to 39% conversion of monomer to polymer. If polymer shrinkage was included, then the total expected shrinkage would be equivalent to 56% conversion of monomer to polymer. Since the measured deviation between micro-dilatometry and NMR is less than 5%, most of the heat is not removed from the droplet by thermally driven evaporation, but by other mechanisms.

Some of the heat would be dissipated by increasing the temperature of the droplet. From Fig. 3.3, the temperature rise of the droplet is estimated to be at most 1 ℃. Raising the temperature of a 10 μL droplet by 1 ℃ would require 0.042 J (or 20% of the heat generated at 18% conversion). This temperature increase would increase the vapor pressure of water by 6% (from 3.2 to 3.4 kPa). However, this temperature rise is temporary as Fig. 3.3 indicates that the elevated temperature lasts for <600 sec before the heat is dissipated. The temperature rise would leave 0.16 J to be dissipated through other mechanisms such as conduction into the substrate as well as convection and radiation into the nitrogen ambient. A small amount of evaporation could also occur. For example, if it is assumed that the larger deviation between micro-dilatometry and NMR results on a SH surface is a result of evaporation (rather than experimental error), then the excess evaporation, equivalent to 4% conversion, would equal to 0.0088 μL of water (4% of

0.218 μL). Evaporation of this amount of water would dissipate 0.02 J leaving 0.14 J (0.16 J – 0.02 J = 0.14 J) to be dissipated by other mechanisms. Thus, thermally driven evaporation at these low % conversions, is a minor contributor to the observed errors.

The relative ability of the superhydrophobic and hydrophobic surfaces (SH and H) to conduct heat into the environmental chamber was estimated. Figure 3.4 shows schematics of a droplet on a SH and H surface with associated parameters related to the thermal resistance values. T_1 and T_4 are the temperatures of the droplet on the SH and H surfaces, respectively. Temperatures of interfaces include: PDMS-glass (T_2), glass-chamber (T_3), PDMS-polyimide (T_5) and polyimide-chamber (T_6). For the SH surface, a simplified model was used to approximate the complex shape of the conical PDMS posts coated with nanoparticles. The PDMS posts were separated into three parts (1) a particle layer, (2) a narrow, cylindrical PDMS post, and (3) a larger PDMS posts.

Assuming that heat is uniformly generated in the droplet during polymerization, the thermal resistance through the superhydrophobic substrate (R_{SH}) can be given by[75,127]

$$R_{SH} = \frac{1}{n_{posts}}[R_{Particles} + R_{PDMS-sm} + R_{PDMS-lg}] + R_{glass} \tag{3.1}$$

where n_{posts} is the number of posts on which the droplet is supported and through which the heat is conducted in parallel. R_x is the thermal resistance of each layer (particles, smaller PDMS cylinder, larger PDMS cylinder and the glass substrate). $R_{particles}$ is also composed of a series of parallel thermal resistors, such that

$$R_{Particles} = \frac{1}{n_{particles}}[R_{silica}] = \frac{1}{n_{particles}}[\frac{h_{silica}}{k_{silica}A_{particles}}] \tag{3.2}$$

Substituting Eq. 3.2 into 3.1 gives:

$$R_{SH} = \frac{1}{n_{posts}}[(\frac{1}{n_{particles}} R_{silica}) + R_{PDMS-sm} + R_{PDMS-\lg}] + R_{glass} \tag{3.3}$$

The various thermal resistance values are obtained by

$$R_{PDMS} = [\frac{h_{PDMS}}{k_{PDMS} A_{PDMS}}] \tag{3.4}$$

$$R_{glass} = [\frac{h_{glass}}{k_{glass} A_{glass}}] \tag{3.5}$$

where h_a is the average thickness of the material $\boldsymbol{a}$, k_a is the thermal conductivity of material $\boldsymbol{a}$, and A_a is the contact area between two adjacent media.

Nitrogen is approximately 6 times less conductive than PDMS (0.026 vs 0.15 W/mK), but due to the larger area, the thermal resistance of the air layer is included for completeness. For the air conduction portion:

$$R_{Air} = \frac{h_{Air}}{k_{Air} \times A_{Air}} = \frac{0.001\ m}{0.026 \frac{W}{mK} \times \left[\left(4mm^2 - 1.13mm^2 \right) \times \frac{1m^2}{10^6 mm^2} \right]} = 1.34 \times 10^4 K/W \tag{3.6}$$

And the total thermal resistance of the Posts and Air in parallel would be:

$$\frac{1}{R_{TOTAL}} = \frac{1}{R_{SH}} + \frac{1}{R_{Air}} \tag{3.7}$$

Table 3.2 lists values used for the calculation of the thermal resistance of the superhydrophobic surface. It is assumed that a 10 μL droplet contacts 16 posts, forming 16 parallel paths for heat conduction. Assuming that 1% of the tip area of the small PDMS cylinder is in contact with water, then $A_{silica} = 2.5 \times 10^{-5}$ mm^2 per post, or 3,000 particle contacts per post. For the configuration used in the simplified model of Fig. 3.4, R_{SH} was determined to be 1.03 ×

10^4 K/W. Combining R_{SH} and R_{Air} results in a total thermal resistance of 5.80×10^3 K/W. The actual thermal resistance would be somewhat lower if convection occurred to a significant degree.

It is interesting to note that the correlation between micro-dilatometry and NMR is similar for the H and SH surfaces even though the difference in thermal resistance between these two surfaces is large. This indicates that conduction through the substrate is not a significant thermal dissipation mechanism.

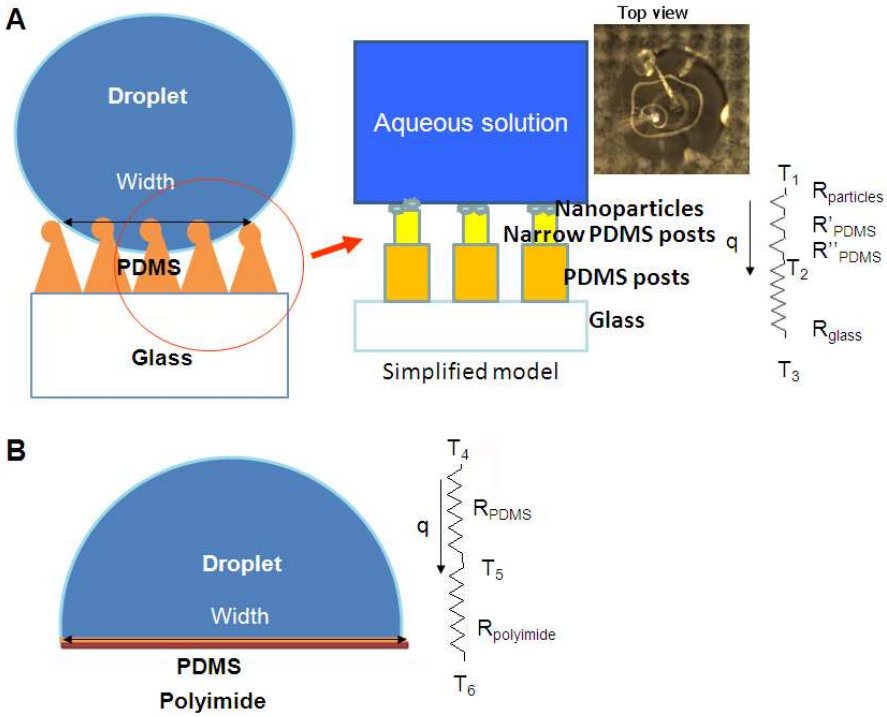

Figure 3.4 Schematic drawings of the droplet on (A) a SH and (B) H surface with relevant thermal resistance values indicated.

Similarly, the thermal resistance (R_H) of the hydrophobic surface is calculated by

$$R_H = R_{PDMS-H} + R_{polyimide} = \frac{h_{PDMS-H}}{k_{PDMS} A_{PDMS-droplet}} + \frac{h_{polyimide}}{k_{polyimide} A_{polyimide-PDMS}} \quad (3.8)$$

Table 3.3 lists the values used for the calculation of the thermal resistance of the hydrophobic surface. For the configuration used in Fig. 3.4B, R_H was calculated to be 81 K/W. This calculation suggests the thermal resistance of the SH surface is approximately 72 times greater than the H surface and so the heat generated by the polymerization reaction would transfer more slowly to the substrate when a SH surface is used.

Table 3.2 Numerical values for the calculation of heat resistance of superhydrophobic surface. Assumptions: 16 posts contact one droplet and total nanoparticle-water contact area is equal to 1% of the narrow PDMS post surface area.

Medium	Average thickness h (mm)	Thermal conductivity k (W/mK)	Diameter (mm)	Specific contact area (mm^2)	Total Contact Area A (mm^2)
Nanoparticles layer	0.0001	1.1[129]	0.0001	7.8×10^{-9} /particle	2.5×10^{-5} /post
Narrow PDMS posts	0.10	0.15[129]	0.1	7.8×10^{-3} /post	0.12 / droplet
Columnar PDMS posts	0.75	0.15[128]	0.3	0.07/post	1.13 / droplet
Glass	1.0	1.1[129]			4.00

Table 3.3 Numerical values for the calculation of heat resistance of hydrophobic surface.

Medium	Average thickness h (mm)	Thermal conductivity k (W/mK)	Contact area A (mm^2)
PDMS layer	0.05	0.15	8.90
Polyimide layer	0.05	0.128[130]	8.90

3.1.4 The Effect of the Vapor Pressure

A second mechanism that could account for excessive shrinkage of droplets is the difference in vapor pressure between the droplet and the reservoirs during polymerization. At the beginning of the experiment, the concentration of acrylamide in the droplet and the solvent reservoirs is the same. As the polymerization reaction proceeds, the concentration of monomer in

the droplet decreases as polymer is formed. According to Raoult's law, the vapor pressure of water is proportional to the number of solute molecules in solution, regardless of molecule size. The vapor pressure of the droplet according to Raoult's law at 0, 18, 29, 39, 62 and 100% conversion is 3.12, 3.13, 3.14, 3.15, 3.17 and 3.20 kPa, respectively. This difference in vapor pressure may not be large, however it is constant and cannot be mitigated by achieving thermal equilibrium. Due to the relatively large volume of the reservoir, evaporation will not mitigate the difference in vapor pressure between partially polymerized droplet and reservoir.

To further separate the effects of thermally generated evaporation and vapor pressure differences, the rate of droplet evaporation at different values of percent conversion was measured. To do this, the droplet volume was monitored continuously by micro-dilatometry with the UV light being turned on for 130 s followed by a 450 s period with the UV light off (dark time).

Figure 3.5 shows the decrease in volume of a droplet (1.40 M acrylamide initial concentration) with 1.40 M acrylamide reservoirs and 0.003 M initiator at 25 ℃ as a function of time under periodic UV illumination. The UV power (0.20 mW/cm2) was turned on after allowing the droplet to stabilize for 600 s. After 130 s of illumination, the light was turned off for 450 s. This process was then repeated 5 times (6 illumination periods total). Due to the decreasing monomer concentration in the droplet, the shrinkage rate of the droplet under UV light gradually decreased with UV illumination. After the first of these cycles, the percent conversion of monomer to polymer was 23%. The volume then remained stable during the dark periods (% volume change <0.1%). During the fourth period, the droplet exhibited continuous shrinkage, exhibiting 0.2% volume loss during the 450 s dark period. The droplet exhibited more obvious shrinkage during following dark periods. One explanation of this result, as discussed in

the previous section, is that the heat generated by the exothermic polymerization reaction causes water to evaporate. Another explanation is that the composition of the droplet changes during the course of the polymerization reaction which affects the vapor pressure of the droplet. As the polymerization reaction proceeds, the number of molecules in the droplet decreases which results in a gradually higher vapor pressure of water compared to that of the reservoirs where the monomer concentration remains constant throughout the experiment. Therefore, the droplet vaporizes until the vapor pressure of droplet approaches that of 1.40 M acrylamide reservoir solution.

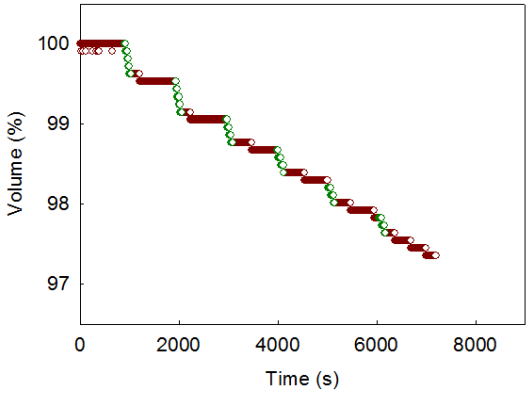

Figure 3.5 The effect of 1.40 M acrylamide reservoirs for a 10 µL droplet with 0.003 M Darocur 1173 polymerization on a SH surface at 25 ℃ under 0.20 mW/cm^2 UV illumination. The exposed period was 130 s and each dark period was 450 s.

To separate the effect of thermally induced evaporation from the decrease in the number of solute molecules, the effect of reservoir solution composition on droplet stability was studied and is shown in Fig. 3.6 and 3.7. Figure 3.6 shows the effect of using pure water reservoirs for a 10 µL droplet of 1.40 M monomer polymerized on a SH surface at 25 ℃ under intermittent UV illumination. As in the previous experiment, the UV power (0.20 mW/cm^2) was maintained for 130 s and then followed by 450 s of dark time. The initial volume of the droplet does not remain stable (before the first UV illumination) as it is absorbing water. The droplet exhibited

continuous swelling before the fourth dark period because of the large number of monomer molecules in the droplet, relative to the pure water solvent in the reservoirs. At longer times, the vapor pressure of the droplet at high conversion approaches that of water. The volume of the droplet gradually stabilized during the dark periods after the fourth dark period.

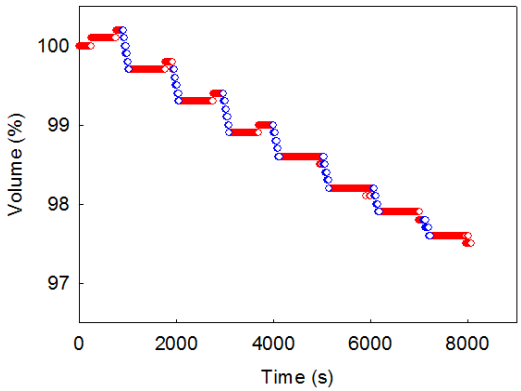

Figure 3.6 The effect of water reservoir for 10 µL 1.40 M acrylamide with 0.003 M Darocur 1173 polymerization on a surface at 25 ℃ under 0.20 mW/cm^2 UV illumination. The exposed period was 130 s and each dark period was 450 s.

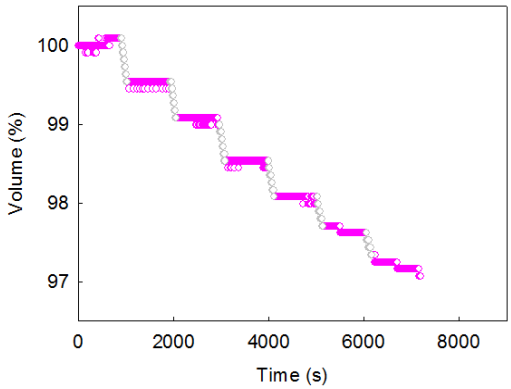

Figure 3.7 The effect of 0.70 M acrylamide reservoir for 10 µL 1.40 M acrylamide with 0.003 M Darocur 1173 polymerization on a surface at 25 ℃ under 0.20 mW/cm^2 UV illumination. The exposed period was 130 s and each dark period was 450 s.

Figure 3.7 shows the effect of 0.70 M acrylamide reservoirs on the 10 µL droplet polymerized at the same conditions. The droplet exhibited swelling before UV illumination. The volume of the droplet then remained stable during subsequent four dark periods. Then, the

droplet started to exhibit shrinkage after the fifth dark period. The droplet swelled initially because the vapor pressure of the droplet was lower than that of 0.70 M acrylamide reservoirs. The shrinkage of the droplet at high conversions occurs because the vapor pressure of the droplet becomes higher than the 0.70 M acrylamide reservoirs. At intermediate % conversions, the droplet volume is stable during the dark periods because the relative concentrations of monomer in the droplet and reservoir are similar.

The effects of the three reservoirs on the rate of droplet volume change during dark times are plotted in Fig. 3.8. For a pure water reservoir (red line with circles), the rate of droplet volume increase is initially fast. As the concentration of acrylamide gradually decreases, the rate of volume change becomes slower. The droplet eventually stabilizes and shows a small decrease at the end of the experiment. When the droplet and reservoir compositions are the same at the start of the experiment (reservoir with 1.40 M acrylamide black line with triangles), the droplet is stable during the initial dark period, then exhibits shrinkage once the volume decreased to 99.15% of its initial size (38% conversion). The rate of shrinkage increases at progressively faster rates as polymerization proceeds. When an intermediate reservoir composition is used (purple curve with squares), the droplet initially swells (total volume change <99.54%), then stabilizes and finally shrinks after the total droplet volume decreases to 97.7%.

3.1.5 The Relative Influence of the Two Mechanisms

These experiments, where the relative composition of the droplet and the reservoir are varied, demonstrate that the primary mechanism which accounts for excess water evaporation is the relative concentrations of molecules in the droplet and the reservoir. Heat generated by the exothermic polymerization reaction may account for a small amount of solvent evaporation, but its significance is secondary. Two experimental observations support this conclusion.

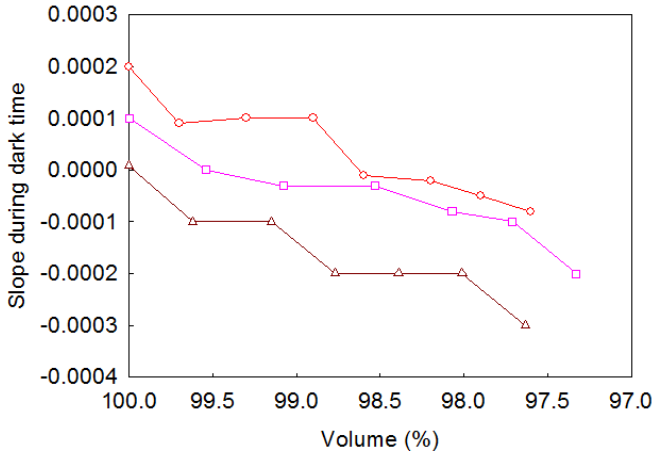

Figure 3.8 The slope of volume change during dark time for the polymerization in a 10 μL droplet with 0.003 M Darocur 1173 on a surface with (-○-) water reservoirs, (-□-) 0.70 M acrylamide reservoirs, or (-△-) 1.40 M acrylamide reservoirs at 25 ℃ under 0.20 mW/cm^2 UV illumination. Each dark time was 450 s.

If significant thermal power was generated in the droplet, which needed to be dissipated into the substrate, then significant evaporation differences between SH and H surfaces would be expected since the thermal resistance of the SH and H substrates are different by a factor of 72 times. However, the correlation between micro-dilatometry and NMR results are very similar on the two types of surfaces. Both exhibit excellent correlation through 18% conversion whereas both exhibit a similar deviation at 30% conversion (difference between micro-dilatometry and NMR: SH surface -24 ± 2%; H surface -21 ± 2%). The incrementally higher deviation observed for the SH surface (3 ± 2%) is within experimental error, but could be due, in part, to thermally induced evaporation resulting from the higher thermal resistance of the substrate (and higher droplet temperature).

The effect of reservoir composition on droplet volume strongly supports the effect of relative solvent vapor pressures as the primary mechanism driving excess evaporation. When the composition of droplet and reservoir are similar, the droplet volume is stable, regardless of the

extent of polymerization that had occurred. For example, when the initial droplet and reservoirs are of the same composition, the droplet volume (dark time) is stable at the beginning of the experiment, and then shrinks at a progressively faster rate as the polymerization proceeds. . However, when the reservoir is pure water, the droplet swells during the initial dark periods, but remains stable after extensive polymerization occurs (~98% total volume). Shrinkage does occur during the dark time, at a slow rate, only once the reaction approaches completion (97.5% volume). If significant heat was dissipated by evaporation of water, droplet stability would not be expected at these high percent conversions. The low shrinkage rate observed toward the end of the experiment may be due to some thermally induced evaporation. Further supporting evidence comes from when the composition of the reservoir is intermediate (0.7 M acrylamide). Under these conditions, droplet stability occurs only during intermediate conversions.

Although micro-dilatometry is well suited for monitoring polymerization reactions at conversions below ~20%, the technique is not well suited for the studies of polymerization reactions at high conversions due to the dynamic change in droplet vapor pressure vs the static vapor pressure of the reservoirs. Adjusting the initial reservoir composition can extend, somewhat, the range of conversions that can be studied reliably. At high conversions, the rate of volume change of the droplet is affected by the relative concentration of the monomer in the reservoir and the droplet. However, micro-dilatometry can accurately monitor the photo-initiated free radical polymerization at low percent conversions as the vapor pressure of the droplet is stable due to the relatively small changes in the number of molecules in the droplet.

3.2 Conclusion

In this chapter results from micro-dilatometry experiments conducted to high percent conversions were studied. It was shown that the accuracy of micro-dilatometry decreases significantly above ~ 18% conversion of monomer to polymer. At ~30% conversion, micro-dilatometry significantly over-estimates the extent of polymerization by 55% (53% conversion observed by micro-dilatometry, vs 29% measured by NMR). At higher percent conversions, the deviation increases even further, eventually exceeding 100% (120% vs 62% conversion by micro-dilatometry and NMR).

Two mechanisms are proposed to explain the observed deviations: evaporation due to heat evolved during polymerization and the change in droplet vapor pressure as the number of molecules in the droplet decreases when monomer is converted to polymer. Although both mechanisms will operate on the droplet, vapor pressure differences were shown to be the dominant mechanism by systematically varying the composition of the reservoir solution. As vapor pressure differences drive solvent evaporation, the process will inevitably cool the droplet, thereby minimizing the impact of the exothermic polymerization reaction. Only as the polymerization reaction approaches completion can the effect of thermally driven evaporation be observed.

Droplet polymerization reactions conducted on SH and H surfaces exhibit similar behavior with the correlations between micro-dilatometry and NMR being essentially the same at ~30% conversions. A slightly higher increase in shrinkage observed on a SH surface compared to a H surface is within experimental error, but may also reflect a small amount of thermally induced evaporation due to the higher thermal resistance of the SH substrate. Polymerization of droplets on the SH surface enhances the utility of micro-dilatometry as the reaction can be conducted to

any arbitrarily large percent conversion and the droplet can be completely removed for subsequent use and/or characterization by external instruments. The thermally insulating properties of these SH surfaces does not significantly affect droplet temperatures or percent conversion measurements.

Chapter 4. The Kinetics of Photopolymerization in Static Droplets

Previous experiments, described in Chapter 2, demonstrated that photopolymerization could be performed with good control in a static droplet on a superhydrophobic or hydrophobic surface inside an environmental chamber. In this chapter, static droplets are used as small (~ 10 μL) reaction containers in which to perform a detailed kinetic study of photopolymerization using a wide range of UV power densities (from 0.050 to 0.130 mW/cm^2) and initiator concentrations (from 0.010 to 0.003 M). Experimental results show that, as expected, the rate of polymerization in a droplet on a surface is proportional to the square root of absorbed light intensity. Compared to reactions in stirred vials, however, the rates of polymerization in droplets are approximately 2 times faster. The mechanisms that could be responsible for the increased polymerization rates in these small droplets will be discussed. GPC experiments were conducted and support a mechanism, where the rate of termination by combination of growing radicals is reduced in droplets relative to reactions of the same solution in a well-mixed vial. The reduced termination rate is caused by a lack of mixing and convection within in these small droplets restricting the mobility of the growing chain radicals.

4.1 Introduction

Free-radical polymerization provides a facile method for fabricating a wide variety of products and its kinetics are well characterized.[1] The kinetics of polymerization reactions are typically studied during only the initial reaction phase (2 - 10% conversion)[124] to minimize the impact of changes to monomer concentration and viscosity as the impact of these effects increase with increasing conversion. At high conversions, the growing polymer radicals become entangled and their motion becomes restricted. This leads to a reduced frequency of polymer chain radicals encountering each other and so a lower termination rate (smaller k_t)[11,13] is obtained. This effect, known as autoacceleration in free-radical polymerizations, can be observed at

percent conversions greater than 40%, especially in bulk systems.[131] Below the onset of autoacceleration, the kinetics are well behaved. As the conversion increases, however, the viscosity of the system can increase significantly which reduces the efficiency of mixing and the mobility of the growing chains (i.e reduced translational diffusion of the center-of-mass of the polymer chains).[31] Although the termination rate decreases, the propagation reaction is only weakly affected by the reduction in the translational motion of the polymer radicals as the smaller monomer molecules remain mobile.[132] As the termination reaction rate decreases without a significant change to the propagation rate, the overall rate of polymerization increases with time[131] during autoacceleration. Autoacceleration is typically detrimental as the reaction cannot be well-controlled, the molecular weight can become too high and the polydispersity becomes too broad.[133,134] To prevent autoacceleration from occurring, reactions are carried out in solution[1,33] or with high shear mixing[17,135] to insure that the frequency of the polymer chain radical encounters is maintained.

In most cases, the shape and size of the reaction vessel does not affect the kinetics so long as the systems are well mixed. When geometries are constrained, however, translational diffusion of polymer chain radicals can become limited and autoacceleration effects can occur. For example, a reduction in the termination rate has been observed in thin polymer coating systems cured by UV light.[13] In these high viscosity coatings, no mixing occurs and monomer is converted to polymer most rapidly at the coating surface. As a result the growing chains rapidly become entangled, reducing k_t, and the polymerization rate increases. The value of k_t was reduced by two orders of magnitude (from 10^6 to 10^4 L mol^{-1} s^{-1}) as the percent conversion increased from 20 to 50%, whereas k_p did not change significantly.[13] Similarly, autoacceleration was observed for polymerization reactions conducted in the pores of nanoporous support

materials.[134] The diffusion of chain radicals is confined by pore size. Compared to bulk systems (50%), autoacceleration occurred at lower percent conversions (18% ~ 40%) with decreasing pore size. The number average molecular weight was found to increase, with a concomitant increase in polydispersity, with decreasing pore size. Given that static environments have been shown to have a significant effect on polymerization kinetics and the resulting molecular weight of polymers, the effect of stable, static, and small (10 μL) droplet reactors on polymerization kinetics merits further investigation.

Use of small and isolated droplets as chemical reactors in microfluidic systems and on superhydrophobic (SH) surfaces has attracted interest because they reduce the quantities of reagents required as well as accelerate reaction times.[71,72,85,87,88,110,136-138] Polymerization reactions in droplets with diluted reactants provide a convenient and economical way to obtain polymers.[72,88,110,137-138] Although polymerization reactions in droplets in microfluidic channels have been reported, where the polymerization conversion percentage was measured by Raman spectroscopy,[110] real-time monitoring of the rate was not conducted and detailed kinetic studies have not been reported. Polymerization reactions in droplets on a SH surface have been reported,[88] however, no kinetic studies were included.

Detailed kinetic studies have been reported for most polymerization reactions in well-mixed solutions. For the study of droplets on a SH surface, a water soluble system is required. Acrylamide is a suitable monomer to study as both it, and the polymer are water-soluble. Polyacrylamide is used commercially in wastewater treatment, soil condition, cosmetics and agriculture, owing to its solubility, nontoxicity, and biocompatibility.[139-141] Therefore, it is important to understand the kinetics of acrylamide photopolymerization to polyacrylamide to achieve the desired properties are well understood.[24-26,48,112,113,121,142-144]

Several groups have reported on the kinetics of acrylamide polymerization in homogeneous aqueous systems using a variety of techniques, such as dilatometry,[25,48,142] FT-IR,[143] gel permeation chromatography (GPC),[24] Raman,[26] and NMR.[121] The dilatometry technique for monitoring the kinetics of photoinitiated radical polymerization in a static droplet is especially appropriate because volume shrinkage, which occurs during polymerization, can be monitored in real-time. For continuously recording the volume change of droplets, we developed a micro-dilatometry technique which records the volume of droplets using a digital camera as described in Chapters 2 and 3. The measured volume data is converted to percent conversion to polymer values using the contraction factor.[112,113,144] Accuracy of the percent acrylamide conversion determined by micro-dilatometry was confirmed with data obtained from ^{1}H NMR for reactions up to 18% conversion. Here, the kinetics of polymerization in droplets of acrylamide solution on SH and hydrophobic (H) surfaces were obtained using micro-dilatometry and compared to kinetics determined in a well-mixed 1.0 mL vial obtained by Raman spectroscopy.

For this kinetic study of photopolymerization in droplets, analysis of the UV light path length and light intensity absorbed by the initiator in the droplet was necessary. Absorption coefficient of Darocur 1173 and the percent light reflected by surfaces were measured by UV-VIS spectrometry and UV specular reflection spectroscopy, respectively. The percent light entering the curved surface of the droplet and reflected within the droplet, were calculated at specific angles using the Fresnel equation and Snell's law. Detailed descriptions of these calculations are shown in Appendix III and IV for droplets and the vial, respectively. The effect of light power density and initiator concentration is discussed and the values of $\Phi^{0.5}(k_p / k_t^{0.5})$ were estimated. The influence of the three environments (droplet on a SH, a H surface, as well as a well-mixed vial) on the polymerization kinetics was determined using the polymerization rates

as well as the molecular weights of the synthesized polymer. An explanation for the faster polymerization rates and higher molecular weights found in droplets, compared to the well-mixed vial, is presented.

4.2 Experimental Section

4.2.1 Materials

Acrylamide (AAm) (electrophoresis-grade, 99%; Sigma–Aldrich), 2-Hydroxy-2-methyl-1-phenyl-propan-1-one (Darocur 1173; Ciba Specialty Chemicals), and hydroquinone (Sigma Aldrich) were all used as received. Milli-Q water (Milli-Q Plus 18.2 Ωcm filter) was used in all instances.

4.2.2 Substrates

Two substrates, (1) a SH surface and (2) a H surface, were fabricated as described in chapter 2.2.4.

4.2.3 Sample Preparation

1.40 M acrylamide aqueous solutions with initiator Darocur 1173 were prepared as described in chapter 2.2.3. A 5% (w/v) hydroquinone in water solution was prepared and used to inhibit polymerization reactions.

4.2.4 Photopolymerization on Substrates

Photopolymerization in a droplet on substrates in an environmentally controlled chamber was described in chapter 2.2.5

4.2.5 Photopolymerization in a Vial

1.0 mL of 1.40 M acrylamide solutions with 0.003 M Darocur 1173 was transferred into a 2.0 mL glass vial (National Scientific) (Fig. 4.1 C) with a magnetic stirring bar (Fig. 4.1 D) and sealed with rubber septa with 13 mm diameter (Fig. 4.1 B). The vial was then placed in a custom-made aluminum holder (Fig. 4.1 E) which was set up above a magnetic stirrer (Fig. 4.1 H) (IKA, model: TOPOLINO S1) and in the sample position of Raman (see below for experimental details). The mirror (Fig. 4.1 J) is used to reflect the Raman laser (Fig. 4.1 I). The temperature of holder is controlled by a chiller (Fig. 4.1 G). The distance between the UV lightguide (Fig. 4.1 F) and the vial was 10 mm. After the sample temperature was stabilized, N_2 (flow rate of 10 cc/min) was conducted into the samples by a needle and air was removed by another needle (Fig. 4.1 A). The contents of the vial were stirred using a magnetic stir bar at 1500 rpm. A bubbler (not shown) created a slight backpressure and prevented air ingress. After purging for 30 min, Raman spectra were collected every 30 s using a Raman laser power of 500 mW. After baseline data were collected for 5 min, the UV lamp was turned on and spectra were collected until polymerization conversion reached 18%. Then, 0.2 mL inhibitor solution was injected into the vial and the sample was stored in the refrigerator until retrieved for NMR or GPC experiments.

4.2.6 Data Collection from Micro-Dilatometry Technique

Volume and contact angle of each droplet were measured using a contact angle goniometer (Model 250, ramé-hart), equipped with a 400 megapixel digital camera and white light source. The volume of the droplet was automatically tracked with ramé-hart's proprietary DROPimage software. The calibration process was described in Chapter 2. Droplets, containing monomer

(1.40 M acrylamide) with initiator Darocur 1173 (0.01 M~0.003 M), were placed on a surface in the environmental chamber and illumined with UV light as described in Chapter 2.2.6.

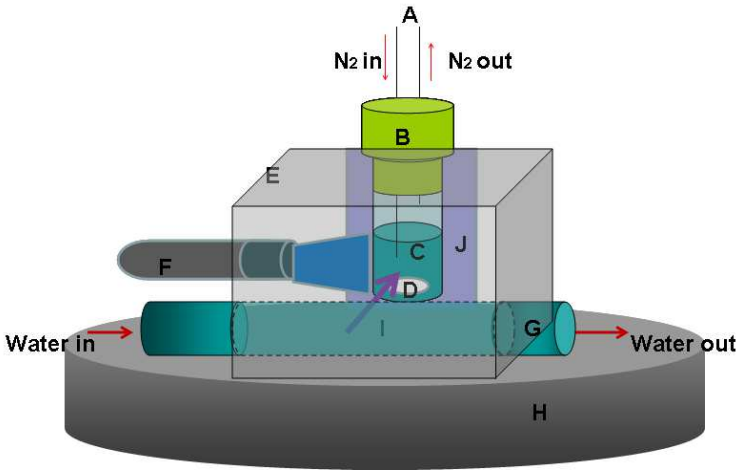

Figure 4.1 Schematic of vial setup for in-situ Raman measurements. A. needles for N_2. B. rubber septa. C. glass vial. D. magnetic stirring bar. E. custom-made aluminum holder. F. UV lightguide. G. water base connected to a chiller. H. magnetic stirrer. I. path of Raman laser. J. mirror.

4.2.7 Data Collection from Raman Spectroscopy

Raman spectra were obtained using a Bruker MultiRam spectrometer (RFS27 FT-Raman, Bruker Instruments Inc.) with 1064 nm Nd:YAG laser and Ge detector. Spectra were collected in the wavenumber range from 3600 to 1100 cm^{-1}. The laser power used was 500 mW, and 10 scans were accumulated at a nominal resolution of 4 cm^{-1}. The spectra from a sample were collected every 30 s via Bruker's OPUS software. Scanning of the sample in a vial before and during photopolymerization was recorded. Figure 4.2 indicates the Raman spectrum of 1.40 M acrylamide before the polymerization. The OH band (3257 cm^{-1}) does not change during the polymerization and is used as an internal standard. Raman bands at 3089 and 3040 cm^{-1}, generated by asymmetric and symmetric CH_2 stretching vibrations, disappear during the polymerization.[145] A CH_3 bending band appears at 2930 cm^{-1} during the polymerization.[146] Three bands at 1663, 1631, 1599 cm^{-1} are assigned to C=O stretching, C=C stretching, and NH_2

bending vibrations, respectively.[147] The peak of C=C stretching disappears during polymerization. The peaks of C=O stretching and NH_2 bending vibrations shift slightly to 1660 and 1600 cm^{-1} during the polymerization due to a change in the environment. A band at 1435 cm^{-1} is assigned to CH_2 bending and NH_2 stretching vibrations. After polymerization, they shift to 1457 and 1433 cm^{-1}, respectively. The CH_2 stretching vibration at 1287 cm^{-1} gradually disappears during polymerization. A broa d aliphatic C-H bending vibration appears at 1325 cm^{-1} after the polymerization.

Since this monomer CH_2 band (1287 cm^{-1}) is easily distinguished and completely disappears during the polymerization reaction, the area of this band was monitored to determine polymerization rate. The monomer CH_2 stretching vibration was integrated between 1310 and 1265 cm^{-1} and the water vibration was integrated between 3560 and 3137 cm^{-1}. The baseline for integrating the area of each peak was determined by a perfectly horizontal line as shown in Fig. 4.2. The OH peak areas were used as an internal standard so that spectra could be normalized between samples. The ratios of integration areas of CH_2 (1287 cm^{-1}) and OH (3257 cm^{-1}) peaks are defined as polymerization conversion.[26]

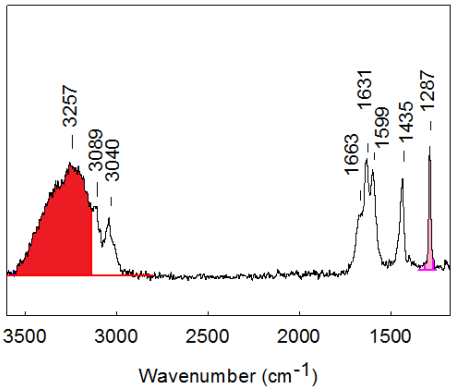

Figure 4.2 Raman spectrum of 1.40 M acrylamide before the polymerization.

4.2.8 Gel Permeation Chromatography (GPC)

The molecular weight and molecular weight distribution of polyacrylamide were characterized using a Waters Breeze HPLC system, equipped with an isocratic HPLC PUMP (Waters 1515) and a refractive index detector (Waters 2414). A set of two columns of PL-aquagel-OH mixed 8 μm were used in the GPC and were protected by one column of PL-aquagel-OH Guard 8 μm. The aqueous phase used was 0.1 M $NaNO_3$ to increase the ionic strength of the solution and prevent polymer molecule elongation. This aqueous phase has been used previously in the GPC measurements for both Polyethylene oxide (PEO) and polyacrylamide.[148] The aqueous phase was vacuum-filtered through a HPLC filtration system (pore size of 0.02 μm, ULTRA-WARE, KONTES) and used as eluent at a flow rate 0.75 mL/min at 30^{o}C. Polyacrylamide standards (American Polymer Standards Corporation) (Mp was from 46,100 to 6,500,000) were used for calibrations. All samples were filtered with a PVDF 0.45 μL syringe filter (National Scientific) as they were injected into the GPC. Air dissolved in the eluent could come out of solution and become trapped as bubbles in the pump which would significantly affect elution times of the sample and solvent. To minimize this effect, air accumulation was minimized by continuously flowing the eluent. In addition, air was periodically purged from the pump. Average elution time of the solvent was calculated based on the elution times of the solvent in each molecular weight standard sample run. Shift times of solvent for standard samples varied from 0 to 4 seconds. This average solvent elution time value was used to correct (linearly shift) the elution times observed for each experiment. The elution time of the synthesized polymer sample was linearly shifted by the same amount of time as the solvent peak shift. Peak positions of polymer samples were reproducible after time shifting. The calibration curve for the molecular weight standards was recalculated based on the corrected

elution times of the standards. Molecular weights and molecular weight distributions of samples were determined using the corrected calibration curve. The symmetry describes the shape of the peaks is calculated as 0.97 using the peak widths at two side of the perpendicular at the peak apex measured at half of peak height. It means well dispersion of polyacrylamide in 0.1 M $NaNO_3$, and the 0.97 is acceptable in GPC analysis.[149,150]

4.2.9 UV-Visible Spectroscopy

The UV reflection spectra and UV absorption spectra were obtained using a PerkinElmer Lambda 650 UV/Vis spectrophotometer at room temperature. Spectra were collected from 280 to 450 nm. Solutions of the photoinitiator, Darocur 1173, were prepared with specific concentrations and aliquots transferred to a 10.0 mm path length quartz cuvette for UV absorption spectra. The transmission spectrum of the 300 nm bandpass interference filter (full width-half max 40 nm, P/N: 67817, Edmund Optics) was obtained with the same instrument. Reflection properties of various substrates were determined using the Perkin Elmer specular reflectance accessory with a 6° angle of incidence (Part No. B0086703).

4.2.10. Refractometer

Refractive index of 1.40 M acrylamide at 25 ℃ was measured by a model Abbe-3L refractometer (Bausch&Lomb).

4.2.11. Kinetic Equations for Photo-Free Radical Polymerization

The degree of the polymerization[119] was determined as a function of the volume change of reactants as discussed in Chapter 2 (Eq. 2.1 in section 2.2.7)

$$\frac{\Delta[M]}{[M]_O} = \frac{(\frac{\Delta V}{V_O})}{C_f \times d_M} \qquad (4.1)$$

where Δ [M] is the incremental change in monomer concentration [M], ΔV is the change in volume from the initial volume of acrylamide, V_o, C_f is the contraction factor and d_M is the density of the pure monomer.

As also discussed in Chapter 2 (Eq. 2.2 in section 2.2.7), the contraction factor, C_f, was calculated by[25]

$$C_f = \frac{1}{d_M} - \frac{1}{d_p} \tag{4.2}$$

where d_M and d_P were the densities of pure monomer and polymer, respectively. In the literature, the C_f of acrylamide was reported to be 0.22 cm^3/g between 25 and 50 ℃[112-113] as well as 0.23 cm^3/g between 45 and 60 ℃.[144] In this chapter, the polymerization was performed at 25 ℃, and hence C_f of acrylamide is taken as 0.22. The density of acrylamide is 1.13 g/mL.

The focus of this chapter is the polymerization rate. The rate of photopolymerization, R_p', is given by[26,151]

$$R_P^{'} = \frac{-d\ln([M]/[M]_0)}{dt} = k_p\left(\frac{\Phi I_{\varepsilon\ell c}}{k_t}\right)^{0.5} \tag{4.3}$$

where [M] is the monomer concentration at time t, and $[M]_o$ is the initial monomer concentration, $I_{\varepsilon\ell c}$ is the moles of absorbed light per liter-second, which is defined by Beer's law, Φ is the number of propagating chains initiated per photon absorbed, k_t is the termination rate coefficient, and k_p is the propagation rate coefficient. Eq. 4.3 is used for obtaining the rate of polymerization in a vial.

Gilbert et al. reported that the photoinitiated polymerization of acrylamide conformed to classic polymerization, where relation between $\ln([M]/[M]_o$ and time is linear.[26] Hence, the

polymerization rates for the droplet experiments were obtained by substituting ($[M]/[M]_o$) (as defined in Eq. 4.1) into Eq. 4.3.[26]

$$R_P' = \frac{-d\ln(1-\frac{(\frac{\Delta V}{V_O})}{C_f d_M})}{dt} = k_p(\frac{\Phi I_{\varepsilon\ell c}}{k_t})^{0.5} = \Phi^{0.5}(\frac{k_p}{k_t^{0.5}})I_{\varepsilon\ell c}{}^{0.5} \qquad (4.4)$$

Eq. 4.4 is used as the basis for determining the polymerization rate as well as the $\Phi^{0.5}(k_p / k_t{}^{0.5})$ value.

A method to determine the $1/\Phi^{0.5} \times (k_p / k_t{}^{0.5})$ value is to obtain number-average molecular weight of a polymer synthesized by a photopolymerization reaction. The number-average molecular weight of a polymer (e.g. polyacrylamide) is described by Eq. 4.5[152]

$$\frac{1}{\overline{M_n}} = \frac{1}{M_o \overline{X_n}} = \frac{1}{M_o}(\frac{(2-a)(k_t{}^{0.5}\Phi^{0.5})}{k_p[M]} I_{\varepsilon\ell c}{}^{0.5} + C_M) = \frac{1}{M_o}(\frac{(2-a)}{[M]}\frac{k_t{}^{0.5}}{k_p}\Phi^{0.5} I_{\varepsilon\ell c}{}^{0.5} + C_M) \qquad (4.5)$$

where $\overline{M_n}$ is the number average molecular weight of the polymer, M_o is the molecular weight of the monomer (e.g. acrylamide), $\overline{X_n}$ is the number average degree of polymerization, a is the fraction of propagating chains terminated by a coupling termination process, and C_M is the chain-transfer to monomer constant. The $\overline{M_n}$ of polymers formed with complete termination by coupling (a=1) is 2 times of that formed by complete termination by disproportionation (a=0). The average coupling fraction value, a, for acrylamide was determined as 0.74 by an ultrasonic depolymerization technique, where the decrease of molecular weight of a polymer and rate of decrease are observed during breaking of its backbone without causing any changes in its chemical nature, has been reported.[27] The C_M of acrylamide at 25 ℃ is 1.2×10^{-5}.[152]

4.3 Results and Discussion

4.3.1 Polymerization in Droplets

Droplets, placed on a SH and a H surface form a nearly spherical shape and a nearly hemispherical shape, respectively, are prepared for performing photopolymerization reaction.

4.3.1.1 UV Absorbance of Initiator Darocur 1173

In order to understand the effect of concentration of the initiator on the absorbance, a Darocur 1173 solution was placed into a rectangular quartz cuvette with 10 mm path length and characterized by UV-vis spectrometry. Figure 4.3 indicates that the initiator Darocur 1173 absorbs UV light between 280 nm and 360 nm. UV absorbance decreased linearly with decreasing initiator concentration as shown in Fig. 4.4. The 0.010 M Darocur 1173 solution absorbs 95% of the light at 300 nm and even more strongly below 300 nm. The 0.0005 M Darocur 1173 has very weak UV absorbance beyond 300 nm. The experiment results are consistent with the results for 0.004 M Darocur 1173 in acetonitrile reported by Dickey et al.[13]

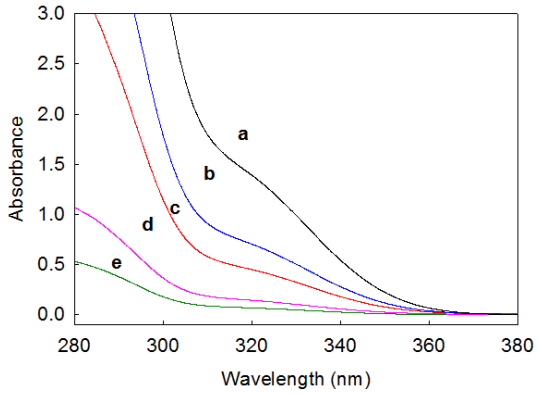

Figure 4.3 UV absorption spectra of the initiator Darocur 1173 dissolved in water using a 10 mm path length cuvette at concentrations of (a) 0.010 M (b) 0.005 M (c) 0.003 M (d) 0.001 M and (e) 0.0005 M.

UV absorbance values for different concentrations of Darocur 1173 were determined at 300 nm. Absorption coefficient of initiator Darocur 1173 was determined using the Beer-Lambert equation $A = \varepsilon \ell c$, where A is the absorbance, ε is the absorption coefficient, ℓ is the path length of light and c is the concentration of initiator. The absorbance and the concentration of initiator have a linear relationship (Fig. 4.4) with a correlation coefficient of 0.998. The absorption coefficient was calculated to be 362 L mol^{-1} cm^{-1}.

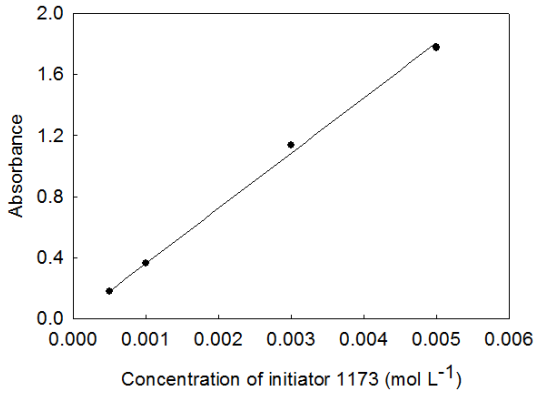

Figure 4.4 The relation of absorbance and concentration of initiator Darocur 1173 at a 300 nm.

The UV absorption of monomer did not have a significant effect on the photopolymerization reaction. Absorbance of the highest and lowest concentration of Darocur 1173 used in the photopolymerization studies is compared with the absorbance of the monomer solution (1.40 M acrylamide) in Fig. 4.5. The 1.40 M acrylamide solution absorbs strongly below 300 nm, but the absorption decreases rapidly above 290 nm such that the absorbance is 0.110 at 300 nm and the absorption coefficient is 0.0787 L mol^{-1} cm^{-1} at this wavelength. In contrast, the 1173 solution absorbs strongly above 300 nm. The average absorption ratio (over the range from 300 - 340 nm) of 1.40 M acrylamide to 0.003 M Darocur 1173 is less than 0.01. The average absorption value of 1.40 M acrylamide is significantly lower at higher 1173 concentrations. So the absorption of monomer does not significantly affect the measured absorption of 1173. In

addition, no polymerization was observed in control experiments where the photopolymerization of 1.40 M acrylamide was conducted in a vial with no initiator (UV= 0.733 mw/cm^2).

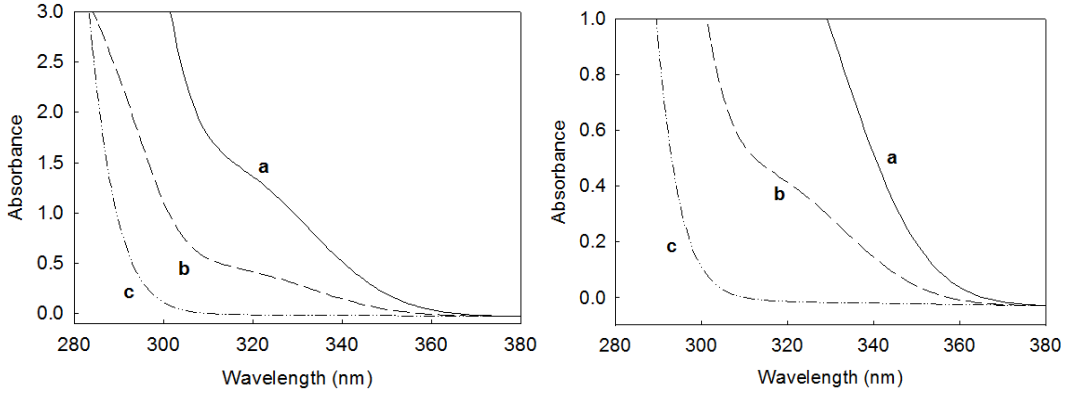

Figure 4.5 UV absorption spectra of (a) 0.010 M Darocur 1173, (b) 0.003 M Darcur 1173, and (c) 1.40 M acrylamide dissolved in water using a 10 mm path length cuvette.

4.3.1.2 UV Path inside Droplets and UV Light Absorbed by Initiator

The path length of UV light and the UV light absorbed by initiator play important roles in the kinetics of the photopolymerization in a droplet. Only when the light path goes through the droplet can the light be absorbed by the initiator molecules and the polymerization reaction begin. In a cuvette, the light path is well controlled and absorbed UV light is easily measured due to parallel walls normal to the light source, thereby minimizing reflections. However, for small droplets, the light path must be carefully considered because the droplet's curved surface means that the incident angle of light will vary across the droplet (assuming that the incoming light is normal to the surface). The angle of incidence affects both the percent of light reflected as well as the path through the droplet. Figure 4.6 illustrates how the UV path is distributed into reflective and refractive paths as UV light enters a droplet on a SH or a H surface. The rays **b**, **c**, and **g** in Fig. 4.6A are absorbed by initiator in a droplet on the SH surface. The rays **b**, **e**, and **h** in Fig. 4.6B are absorbed by initiator in a droplet on the H surface. Other rays in Fig. 4.6 are transmitted or reflected by the media.

A. Reflection, Refraction, Path Length and Relative Power of UV Light Interacting with a Droplet. How the incident light intensity is divided between the reflected and refracted rays is provided by the calculation of reflectance (ρ), which is based on Fresnel equations for unpolarized light and is equal to the average reflectance for the perpendicular ($sin^2(\theta_i - \theta_r)/sin^2(\theta_i + \theta_r)$) and parallel polarizations ($tan^2(\theta_i - \theta_r)/tan^2(\theta_i + \theta_r)$).[153] The ρ is as a function of the incidence angle and refraction angle.[154]

$$\rho = \frac{1}{2}\left[\frac{\sin^2(\theta_i - \theta_r)}{\sin^2(\theta_i + \theta_r)} + \frac{\tan^2(\theta_i - \theta_r)}{\tan^2(\theta_i + \theta_r)}\right] \tag{4.6}$$

where θ_i is incident angle and θ_r is refraction angle which is calculated using Snell's law, $sin\theta_i / sin\theta_r = n_2 / n_1$, where n is the refractive index of the medium.

Light will encounter the droplet at different incident angles, depending upon where on the droplet's curved surface the light is incident. Since UV light uniformly illuminates the droplet from above, the light rays can be assumed to be parallel (perpendicular to the substrate) with a range of incident angles between 0 and 90°. Based on Fresnel equations, Snell's law and the refractive index of 1.40 M acrylamide at 25 ℃ (1.35), the fraction reflected increases with increasing incidence angle (Fig. 4.7). At a 50° angle of incidence, only 4% of the light is reflected. However, at 75° angle of incidence, 22% is reflected and at 85°, 59% is reflected.

A.1. Superhydrophobic Droplet Surface. To estimate the fraction of light entering a 10 μL droplet, the illuminated surface (upper half of droplet) was sliced up into small segments; 360 triangles at incident angle of 0.1° and 32400 trapezoids between incident angles of 0.1° and 90° for the calculation of reflected light as illustrated in Fig. 4.8. Over all angles on the three-dimensional surface of the droplet, the percent of the average reflected light ray **a** (Fig. 4.6A) is

7.2% and the percent of the average refracted light ray **b** (Fig. 4.6A) is 92.8% of incident light. The calculations are shown in Appendix III.

Once the fraction of incident light that enters a droplet is determined, the angle and path length within the droplet must be calculated. Due to the refraction of light in the droplet, the range of angles of refracted light ray **b** in Fig. 4.6A is between 0 and 48° with respect to the incident light path.

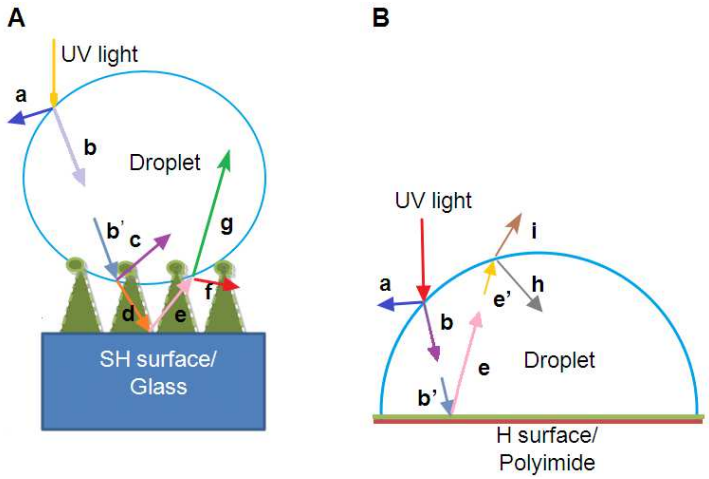

Figure 4.6 Schematic of UV light path for the photopolymerization of the droplet on (A) a SH and (B) a H surface: (a) reflection by the droplet, (b) refraction as UV light enters the droplet, (b') transmitted ray, (c) reflection at the lower nitrogen interface, (d) refraction as UV light enters nitrogen, (e) reflection by the surface, (e') transmitted ray, (f) reflection by the droplet, (g) refraction as UV light enters the droplet, (h) reflection at the upper nitrogen interface, and (i) refraction as UV light enters nitrogen.

As **b** travels through the droplet, some of it is absorbed by initiator molecules. Most of the light (ray **b'**), however, reaches the liquid-nitrogen interface of the bottom surface of the suspended droplet. Based on the incident angle and the ratio of refractive index of nitrogen and acrylamide, 3.0% of the incident light (ray **b'**) will be internally reflected and make a second transit across the droplet (ray **c** in Fig. 4.6A). Additional light will be absorbed during this transit.

Although 3.0% of the incident light is internally reflected, most of the light (97.0%) will exit the droplet and impinge upon the SH surface (ray **d** in Fig. 4.6A).

The percent reflectance of a bare SH surface was measured by specular reflection spectroscopy and was found to be 2.1% of the incident light. This is shown as ray **e** in Fig. 4.6A. The effect of the PDMS posts on rays **d** and **e** is assumed to be small given their small area fraction. Approximately 97.0% of the light incident on the bottom surface of the droplet (ray **e**) will enter the droplet at the nitrogen-liquid interface and travel across the droplet (ray **g** in Fig. 4.6A). The other 3.0% of the light will be reflected back into the nitrogen (ray **f** in Fig. 4.6A). The results are summarized in Table 4.1.

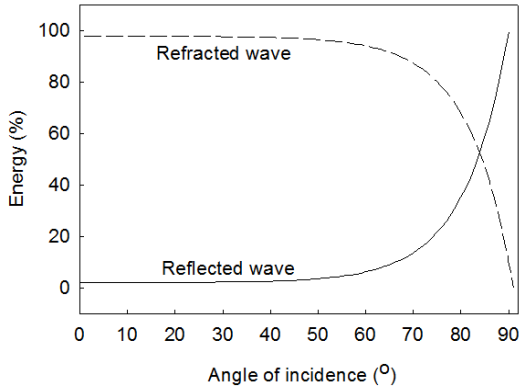

Figure 4.7 The percent of the energy reflected and refracted when an incident wave in nitrogen falls on 1.40 M acrylamide (n=1.35). Data calculated using Eq. 4.6.

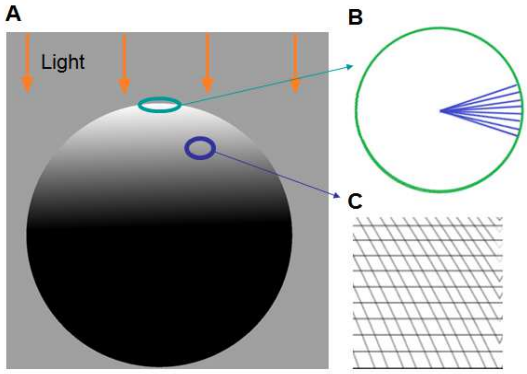

Figure 4.8 Schematics of (A) illuminated sphere, (B) the triangle pieces on the top of the sphere and (C) the trapezoid pieces on the side of the sphere.

A.2. Hydrophobic Droplet Surface. On a H surface, the UV light interaction with the droplet is shown in Fig. 4.6B. Similar to a droplet on a SH surface, the percent of the average reflected light ray **a** and refracted ray **b** (Fig. 4.6B) is 7.2% and 92.8% of the incident light. Ray **b** is absorbed by the solution and so its power is decreased as it reaches the substrate (ray **b'**), where it is partially absorbed by the substrate and partially reflected to form ray **e**. The power of ray **e** is 7.5% of the incident light (ray **b'**) as determined from a measurement of the scattered light on a bare H surface. As ray **e** is transmitted across the droplet and reaches the liquid-nitrogen interface, the power is reduced (ray **e'**) due to absorption by the initiator. Ray **e** is scattered by H surface, and hence the incident angle of ray **e'** at the liquid-nitrogen interface is smaller than 60^{o}. If it is assumed that ray **e** is reflected by the H surface, ray **e'** primarily escapes into the nitrogen (ray **i**, 96.3%), whereas 3.7% of the light is internally reflected (ray **h**). The details are shown in Appendix III. If we assume ray **e** is scattered, rather than reflected, off the liquid-solid interface, some of the angles of incidence of **e'** at the liquid-nitrogen interface will be greater than 45^{o}. This would increase the percent of internal reflection (increase the **h/i** ratio) but would not have a significant impact on the overall absorbed light as the power of ray **e'** is very small and does not have significant influence on the total amount of absorbed UV. The results are summarized in Table 4.1.

Table 4.1 The various UV rays and their relative power for a 10 μL droplet on a SH and a H surface.

	ray **a**	ray **b**	ray **c**	ray **d**	ray **e**	ray **f**	ray **g**	ray **h**	ray **i**
SH	7.2% of incident	92.8% of incident	3.0% of ray **b'**	97.0% of ray **b'**	2.1% of ray **d**	3.0% of ray **e**	97.0% of ray **e**		
H	7.2% of incident	92.8% of incident	-	-	7.5% of ray **b'**			3.7% of ray **e'**	96.3% of ray **e'**

B. UV Absorption within A Droplet. To calculate the amount of light absorbed by initiator molecules, the Beer-Lambert law was used. The transmission is a function of the incident light and the absorbance as shown in the following equations.[30]

$$I_T = I_o \times 10^{-A} = I_o \times 10^{-\varepsilon \ell c} \tag{4.7}$$

$$I_A = I_o - I_T = I_o \times (1 - 10^{-\varepsilon \ell c}) \tag{4.8}$$

where I_T is the transmitted intensity, I_o is the incidence intensity, and I_A is the absorbed intensity.

B.1. Average Path Length. The path length of UV light in the droplet determines the UV light absorbance for solutions with the same absorption coefficient and concentration. Two approaches were used to calculate the average path length of ray **b**, the ray that accounts for the majority of the absorption within a droplet on either a SH and H surface.

In the first method for calculating the average path length across a droplet the light was assumed to be at an infinite distance from the droplet. In this method, the sphere was divided into segments (360 triangles and 32400 trapezoids as described previously and shown in Fig. 4.8) and the Fresnel equation and Snell's law was used to calculate the average path length for each segment. Based on these calculations, the average path length for SH and H surfaces was determined to be 1.63R and 0.77R, respectively, where R is radius of the droplet. The details are shown in Appendix III.

In the second approach, the geometrical calculations based on the work by Horowitz et al.[21] were used and then modified to take into account the refractive index of the acrylamide solution. In their study, two conditions were examined. In one case (C_∞), the light source was assumed to be at an infinite distance from the sphere and so the rays were mutually parallel. In the other case (C_0), the light source was assumed to be distributed about the surface of the sphere. The average

path length of light traversing a sphere was shown to equal to 4/3R or R for case C_∞ and C_0, respectively.[21] However, these assumptions did not account for a change in the refractive index of the medium. By including the nitrogen to acrylamide solution transition, the average path length of light for a perfectly spherical droplet would be 1.66R and 1.53R for case C_∞ and C_0, respectively. Taking into account actual droplet shape, for a droplet on a SH surface, where the contact angle is 155° (as opposed to a perfect sphere, where the contact angle = 180°), the average path length would be 1.63R and 1.50R based on assumptions C_∞ and C_0, respectively.

On a H surface, where the droplet forms a contact angle of 95° with the surface, the average path length across the droplet is 0.78R and 0.63R, based on assumptions C_∞ and C_0, respectively. The radius, R, is obtained by the measured volume of droplet on a surface, $R = (V/(4/3 \times \pi\text{-}1/3 \times \pi \times (2\text{-}3 \times \cos(180°\text{-}95°) + \cos(180°\text{-}95°))))1/3$.[81]

The C_∞ values calculated using the method of Horowitz are in good agreement with the values calculated using the first method, validating the calculation approach. Due to diverging of the UV light from a lightguide and the relatively short (23 mm) distance between lightguide and droplet, the incident light is not perfectly parallel. However, the difference in path length between the parallel (C_∞) and divergent (C_0) cases is less than 7% for the superhydrophobic droplet. Path length values based on the assumption that the incident light is at an infinite distance from the droplet and perpendicular to the substrate (1.63R and 0.78R for the SH and H drop, respectively) will be used.

B.2. Calculation of Absorbed UV Power. The absorbed rays **b**, **c**, and **g** in Fig. 4.6A and the rays **b**, **e**, and **h** in Fig. 4.6B for a 10 μL droplet with 0.003 M Darocur 1173 were calculated and shown in Table 4.2. The incident light power was measured using a Nova II Laser Power/Energy Monitor (OPHIR) with a Photodiode Sensor (PD 300) and a 25 mm diameter filter

with center wavelength 300 nm/ full width-half max 40 nm (Edmund). The intensity of UV light of wavelength between 300 and 500 nm from manufacturer's data is shown in Fig. 4.9A. The intensity of UV light of wavelength between 350 and 500 nm with filter and without filter is detected by Ocean Optics and shown in Fig 4.9B. After light went through the filter, the light of wavelength between 380 and 500 nm was not included. During the polymerization, UV light with wavelength between 300 and 500 nm illuminated the droplet. However, the light with wavelength between 300 and 360 nm was absorbed by initiators. To measure the light absorbed by initiator, the detector was set up at a distance of 23 mm from the UV light guide with filter, which replicated the distance between droplet and lightguide in the environmental chamber. The incident light on a droplet was then determined by multiplying the light power density by the area of intersection between the light and droplet. For a droplet, the area of intersection would be the projected area of the droplet onto the substrate, which is a circle with the same radius as the 10 μL droplet on a SH surface (R = 0.13 cm, projected area = 0.053 cm^2) and for a droplet on a H surface, the area of contact is comparable to the area of contact between droplet and the solid surface (R= 0.16 cm, projected area = 0.080 cm^2).

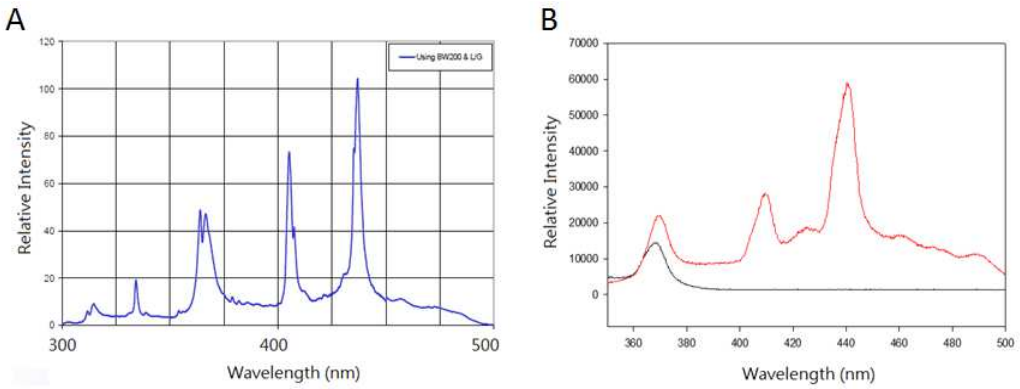

Figure 4.9 Spectral output of UV light at wavelengths (A) between 300 and 500 nm from manufacturer's data,[155] as well as (B) between 350 and 500 nm with filter (—) and without filter (—).

Table 4.2 The absorbed UV power in a 10 μL droplet with 0.003 M Darocur 1173 on a SH and a H surface.

Surface	Incident power density $\times 10^3$ (mW/cm^2)	First absorbed power[(a)] $\times 10^3$ (mW)	Second absorbed power[(a)] $\times 10^3$ (mW)	Third absorbed power[(a)] $\times 10^3$ (mW)	Total power $\times 10^3$ (mW)
SH	74[(b)]	from ray **b**[(d)] 1.5	from ray **c**[(d)] 0.026	from ray **g**[(d)] 0.017	1.5
H	74[(c)]	from ray **b**[(e)] 1.5	from ray **e**[(e)] 0.081	from ray **h**[(e)] 0.0022	1.6

(a) Data were calculated using the Beer-Lambert law.
(b) Two-dimensional projection of light onto a sphere, which is equal to a circle with the same radius as the 10 μL droplet on a SH surface: 0.053 cm^2.
(c) Two-dimensional projection of light onto a half sphere of a 10 μL droplet on a H surface is 0.080 cm^2.
(d) Fig. 4.6A.
(e) Fig. 4.6B.

The amount of light absorbed during the first transit across the droplet (ray **b** in Fig 4.6A and 4.6B) is calculated using the Beer-Lambert Law, where ε is 362 L mol^{-1} cm^{-1}, and ℓ is 1.63R or 0.78R for droplets on a SH and a H surface, respectively. The light power of absorbed ray **b** for these two cases is 38% and 25% of the incident light power due to reductions from reflections off the curved surface. For the second transit (ray **c** or **e** for the SH and H drop, respectively), the same procedure is used. The light power of absorbed ray **c** and **e** for the droplets on the SH and H surface is 0.7% and 1.4% of the incident light power, respectively. For the third transit, the absorbed ray **g** and **h** intensities are 0.4% and 0.04% of the incident light power, respectively. As can be seen in Table 4.2, the light absorbed by the initiator molecules is dominated by the first light path transit which accounts for over 94% of the absorbed light power. Due to the shorter path length across a droplet and larger diameter on the H surface, the same incident light power (74 mW/cm^2) results in approximately the same absorption in H and SH droplets of the same volume. The first-pass absorption in a H droplet is equal to that in a SH (1.5

vs 1.5 × 10^{-3} mW) and the overall absorption values are calculated to be approximately 7% higher than in a SH (1.6 vs 1.5 × 10^{-3} mW).

4.3.1.3 Photopolymerization in a Droplet on a Surface

The volume change of a droplet during the polymerization on the surface is used to monitor the percent conversion in this polymerization kinetic study. The droplet experiments were performed in a temperature and atmosphere controlled environmental chamber to maintain stable droplet volume before polymerization. The rate of polymerization was determined by monitoring the change in volume of the droplet and converting to the percent monomer conversion using the contraction factor for acrylamide. The relation between the fractional conversions of acrylamide with respect to reaction time is shown for two representative droplets in Fig. 4.10 and Fig. 4.11 for droplets on a SH and a H surface, respectively.

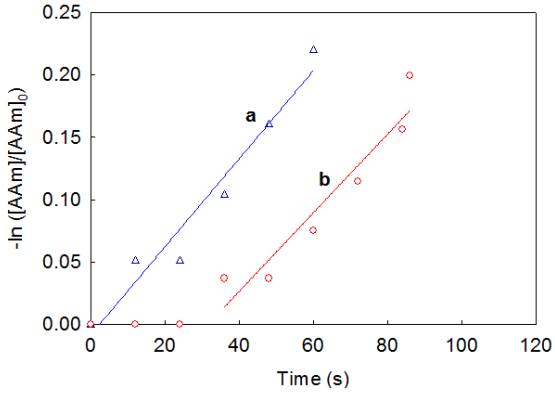

Figure 4.10 Fraction conversion, ln ([AAm]/[AAm]$_o$), as a function of time on a SH surface at 25 ℃ under UV at (a) (△) 0.090 mW/cm^2 (absorbed power: 0.0019 mW, *Rp'*=0.0035 s^{-1}, and R^2=0.955) and (b) (◯) 0.066 mW/cm^2 (absorbed power: 0.0014 mW, *Rp'*=0.0032 s^{-1}, and R^2=0.911). All droplets composed of 1.40 M acrylamide solution with 0.003 M Darocur 1173.

Figure 4.10 shows the results for two representative droplets; results for all droplets studied on a SH surface are shown in Table 4.3. The percent conversion in one of these droplets on a SH surface was 19% after 60 s under UV power of 0.090 mW/cm^2. Using a lower UV power density

of 0.066 mW/cm^2, the conversion for the second droplet was 18% after 86 s. Induction time for these two experiments was short (<4 s for 0.090 and <30 s for 0.066 mW/cm^2). Based on Eq. 4.4, the rates of polymerization (R_p') under UV 0.090 and 0.066 mW/cm^2 are 0.0035 and 0.0032 s^{-1}, respectively. In these cases, increasing the UV power density by 37% resulted in a 9% increase in polymerization rate.

Figure 4.11 shows the results for two representative droplets on a H surface; results for all droplets studied on a H surface are shown in Table 4.3. The percent conversion for these two droplets illuminated with different UV powers densities (0.11 and 0.074 mW/cm^2) is shown. Induction time for these two experiments are short (<30 s for 0.11 and 0.074 mW/cm^2). The droplet achieved 19 % conversion within 108 s and had a rate of 0.0028 s^{-1} when illuminated with light at power density of 0.11 mW/cm^2. The conversion for a droplet under UV 0.074 mW/cm^2 achieved 14 % within 84 s and gave a rate of 0.0022 s^{-1}. Increasing the UV power density by 49% resulted in a 27% increase in polymerization rate in Fig. 4.11.

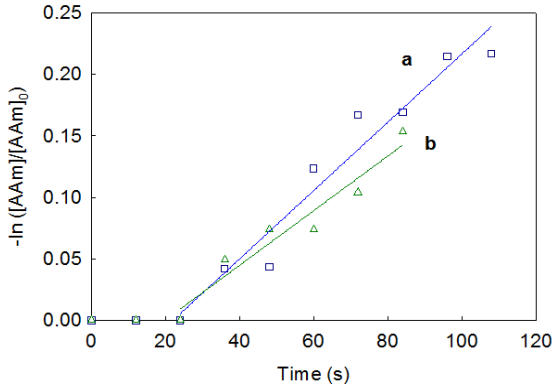

Figure 4.11 Fraction conversion, In ([AAm]/[AAm]$_o$), as a function of time of 1.40 M acrylamide droplet with 0.003 M Darocur 1173 on a H surface at 25 ℃ under (a) (□) 0.11 mW/cm^2 (absorbed power: 0.0023 mW, *Rp*'=0.0028 s^{-1}, and R^2=0.947) and (b) (Δ) 0.074 mW/cm^2 (absorbed power: 0.0016 mW, *Rp*'=0.0022 s^{-1}, and R^2=0.933).

Polymerization rates in droplets on SH and H surfaces for different concentrations of Darocur 1173 and different incident UV light power intensities are shown in Table 4.3. The absorbed UV light intensities shown in Table 4.3 were calculated as the photon flux at 300 nm in order to facilitate comparisons of the absorbed UV light in all experiments. The photon flux (E_p) is defined as the number of moles of photons per second per unit area on a surface using the equation $E_p = N\,hc/\lambda$, where N is Avogadro's number, h is Planck's constant, c is the speed of light and λ is the wavelength of incident light. E_p at 300 nm of wavelength is 6.63×10^{-19} Ws.

Table 4.3 The effect of initiator concentration on absorbed light and rate of polymerization of ca. 10 μL 1.40 M acrylamide droplets on SH and H surfaces. Reported rates are averages of three experiments per condition. Conversion from Micro-dilatometry for all experiments is 18 ± 2%.

Surface	[1173] $\times 10^3$ (mol L^{-1})	Incident power density$\times 10^3$ (mW/cm^2)	Absorbed light intensity[(a)] $\times 10^7$ (mol s^{-1} L^{-1})	Induction time (s)	R_p' (s^{-1})
SH	10.0	61	6.3	11 ± 3	0.0039 ± 0.0003
SH	5.0	126	9.3	14 ± 5	0.0046 ± 0.0002
SH	5.0	103	7.6	14 ± 5	0.0044 ± 0.0002
SH	5.0	95	7.2	14 ± 5	0.0038 ± 0.0002
SH	5.0	54	4.0	16 ± 7	0.0032 ± 0.0002
SH	3.0	90	4.7	14 ± 5	0.0034 ± 0.0002
SH	3.0	74	3.9	20 ± 7	0.0031 ± 0.0002
SH	3.0	66	3.5	22 ± 9	0.0030 ± 0.0002
SH	3.0	54	2.8	30 ± 15	0.0026 ± 0.0001
H	10.0	89	11	15 ± 8	0.0045 ± 0.0003
H	10.0	61	7.6	20 ± 7	0.0037 ± 0.0002
H	5.0	82	6.5	15 ± 8	0.0034 ± 0.0002
H	5.0	54	4.3	28 ± 15	0.0023 ± 0.0002
H	3.0	110	5.8	20 ± 7	0.0029 ± 0.0002
H	3.0	74	3.9	36 ± 12	0.0022 ± 0.0002
H	3.0	54	2.9	36 ± 12	0.0019 ± 0.0002

(a) Data were calculated using a 300 nm wavelength.

Several trends can be seen in Table 4.3. As the UV light power density increases, the rate of polymerization also increases; a detailed analysis of this relationship is discussed in section 4.3.3. Under the same incident UV power and the same surface, the rate of polymerization increases as

the initiator concentration increases. For example, the polymerization rate values for SH experiments under UV 0.054 mW/cm^2 become slower as initiator concentration changes from 0.005 M to 0.003 M. Using the same initiator concentration, the polymerization rate decreases with decreasing absorbed light intensity within experimental error. The induction time for the SH experiment ranges from 11 to 44 seconds, increasing with decreasing absorbed light intensity. The trends for droplets on H surfaces are similar and those for SH surfaces. The average rates of polymerization of droplets on a SH surface are about 1.1 times the average rate of polymerization on a H surface.

4.3.2 Polymerization in a Vial

The small volume of these 10 μL droplets could influence the kinetics of polymerization due to the lack of mixing and limited convection within the static droplets. In order to determine the effect of this restricted environment, photopolymerization reactions were also conducted in a well-mixed 1 mL vial, which represents a 100 fold volume increase over the droplets. In the 1.16 cm (o.d.) glass vial, 1.0 mL of 1.40 M acrylamide solution with Darocur 1173 initiator was placed. The vial is inserted into an environmental holder and set on the magnetic stirrer. The oxygen in the solution was purged and removed using nitrogen. The solutions were irradiated with a range of UV powers as shown in Table 4.4.

To calculate the amount of UV light absorbed by the initiator, the first step is to determine the percent of UV light which is transmitted into the solution. The percent transmission of the glass vial at a wavelength of 300 nm was characterized by UV-Vis spectrometry to be 49.9%. This relatively low percent transmission is due to reflections off the curved surface of the vial, absorption by the glass, and the refractive index of the medium.

To calculate the contribution from the vial, the following steps were taken. In the spectrometer, the vial is illuminated over a 47 mm^2 area (Fig. 4.12A). The largest incident angle of light on this surface is 36.2°. This illuminated area of the vial was sliced into 9,350 polygons to calculate the reflected light energy. Based on Fresnel equations and Shell's law, (where the refractive index of glass at 25 ℃ and nitrogen is 1.50 and 1.00, respectively), and considering that light is transmitted through two walls of the vial before reaching the UV detector, 84.6% of the light would be transmitted to the UV detector assuming that the glass does not absorb any light. Since measurements show that only 49.9% of the light is transmitted, then each glass wall of the vial absorbs 23.2% of the incident light at 300 nm. The details are in Appendix IV.

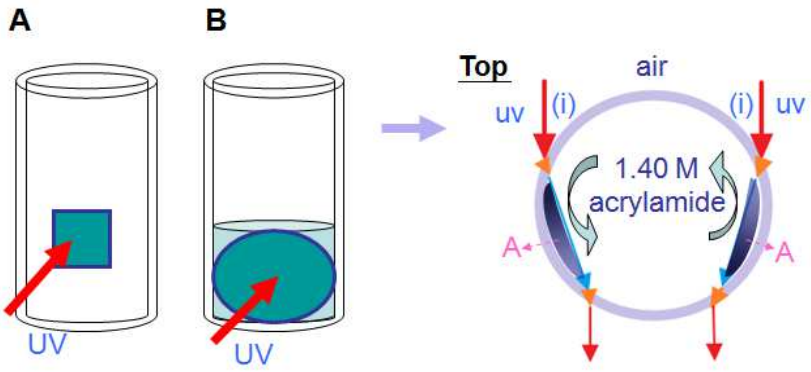

Figure 4.12 Schematics of (A) illuminated area by UV-Vis spectrometry and (B) illuminated area by UV light during polymerization as well as top view (UV light ray (i) has the largest incident angle. Area A is dark part in the vial.).

When polymerization reactions are performed in a vial within the Raman spectrometer, the distance between the vial and the UV lightguide is 1.0 cm. A circular area with a diameter of 1.0 cm is illuminated on the wall of the vial. Due to thickness of the glass vial of 0.77 ± 0.02 mm and refractive index of medium, the range of incident angles on glass is between 0° and 60.0° and the range of incident angles on the solution is between 0° and 41.7° (Fig. 4.12B). To calculate the light transmitted into solution, a calculation was conducted by applying 34,000

polygons onto the circular area of light as well as taking into account the absorption of the glass and the refractive index of the acrylamide solution. Based on this calculation, 74.0% of the incident light would be transmitted into the solution.

The UV light illuminating the wall of the vial has a circular area of 1.0 cm diameter as shown in Fig. 4.12B. Most of the light would strike the center of the vial and less at the edge, resulting in a longer average path length. To calculate the average path length, the area was divided into 32,000 polygons. The average path length was calculated to be 1.83R.

The light absorbed by the initiator in the vial was calculated using Eq. 4.8 and converted to absorbed light intensity at 300 nm and shown in Table 4.4. As the UV light power density increases, the absorbed light intensity also increases.

Table 4.4 The rate of polymerization in 1.0 mL 1.40 M acrylamide with 0.003 M Darocur 1173 in a vial under UV. Reported rates are averages of three experiments per condition.

Incident power density[(a)] $\times 10^3$ (mW/cm^2)	Absorbed power[(a)] $\times 10^1$ (mW)	Absorbed light intensity[(b)] $\times 10^7$ (mol s^{-1} L^{-1})	Conversion from Micro-dilatometry (%)	Induction time (s)	R_p' (s^{-1})
733	4.8	12	20 ± 1	149 ± 4	0.0029 ± 0.0003
407	2.7	6.7	19 ± 1	140 ± 28	0.0018 ± 0.0003
325	2.1	5.3	20 ± 1	183 ± 65	0.0017 ± 0.0001
102	0.67	1.7	19 ± 1	178 ± 76	0.0010 ± 0.0001
76	0.50	1.2	20 ± 1	324 ± 51	0.0011 ± 0.0001

(a) Two-dimensional projection area of light onto the side of the vial is 0.79 cm^2.
(b) Data were calculated at a wavelength of 300 nm.

The concentration of acrylamide in a vial during the polymerization reaction was monitored in real time by Raman (Fig. 4.13). The CH_2 vibration band for acrylamide is between 1310 and 1265 cm^{-1}. The peak region of water is between 3560 and 3137 cm^{-1}. Figure 4.13 shows the decrease of the CH_2 vibration with polymerization time. As discussed in section 4.2.7, the

concentration of acrylamide was obtained by calculating the ratio of the area of the CH_2 vibration with the OH peak. This ratio was calculated every 30 seconds.

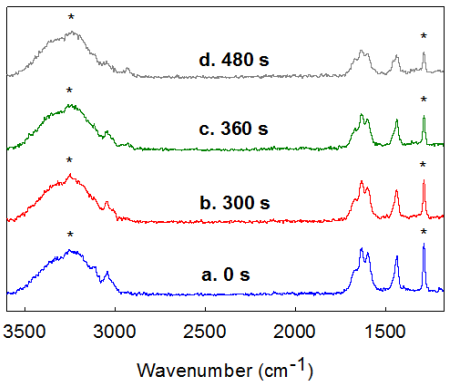

Figure 4.13 Raman spectra (10 accumulation) for 1 mL 1.40 M acrylamide with 0.003 M Darocur 1173 in a vial at 25 ℃ under UV 0.325 mW/cm^2 when exposure time is (a) 0 s, (b) 300 s, (c) 360 s and (d) 480 s.

To provide an illustrative example of the photopolymerization reaction, a plot of monomer conversion to polymer vs reaction time is shown in Fig. 4.14 (0.003 M Darocur 1173) for two UV powers intensities: 0.325 and 0.407 mW/cm^2. At a power density of 0.325 mW/cm^2, the conversion for acrylamide monomer to polymer reached 19% within 280 s, at a rate of 0.0017 s^{-1}. At a higher power density (0.407 mW/cm^2), the polymer conversion reached 20% within 240 s, giving a rate of 0.0019 s^{-1}. The rate increased 11% as UV intensity increased 25%. The difference in induction time between two experiments is less than 50 s.

Data for the rates and induction times for all experiments in the vial is shown in the Table 4.4. As the UV light power density increases, the rate of polymerization also increases; a detailed analysis of the relation is discussed in the next section (4.3.3). The induction times in Table 4.4 show a similar trend to those for the droplets (Table 4.3); shorter induction times are observed at higher UV power densities. The induction times for the vial experiments are longer than those for the droplets in Table 4.3 due to the larger volume of solution.

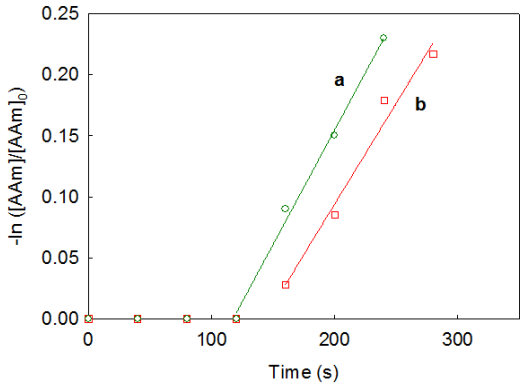

Figure 4.14 Fraction conversion, ln ([AAm]/[AAm]$_o$), plotted as a function of time for a 1 mL 1.40 M acrylamide with 0.003 M Darocur 1173 in a vial at 25 °C under (a) (□) 0.325 mW/cm^2 (*Rp'*=0.0017 s^{-1}, and R^2=0.976) and (b) (○) 0.407 mW/cm^2 (*Rp'*=0.0019 s^{-1}, and R^2=0.995).

These reaction rates and induction times for well-mixed solutions are comparable to those reported in the literature using a different initiator. Seabrook et al. reported the photo-polymerization of 1.41 M acrylamide with the initiator 2,2'-Azobis(2-methylpropionamidine) di-hydrochloride (V-50), where [*I*] was varied from 0.010 M to 0.0005 M.[26] The relationship between initiator concentration and polymerization rate was similar, as was the relationship between UV power and induction time. For example, Seabrook reported that acrylamide with 0.010 M V-50 had rate of polymerization of 0.0012 s^{-1} and induction time of 300 s, whereas reducing the concentration of V-50 to 0.0005 M reduced the rate of polymerization to 0.00033 s^{-1} and increased the induction time to 750 s. When the initiator V-50 was used in our vial set-up, similar results to Seabrook were obtained. Acrylamide with a V-50 concentration of 0.010 M exhibited a polymerization rate of 0.0010 s^{-1} and induction time of 256 s, whereas a lower V-50 concentration of 0.0005 M exhibited a polymerization rate of 0.00027 s^{-1} and induction time of 815 s. These results are within 20% of Seabrook's values and demonstrate the validity of the procedure. As discussed previously in section 2.1, we only used Darocur 1173 in our droplet experiments, as V-50 evolves nitrogen gas during radical generation; the resulting gas bubbles in

the droplets interfere with the micro-dilatometry volume measurements. Darocur 1173 results in faster reactions and lower induction times than V-50.

4.3.3 Kinetic Study

As discussed in section 4.2.11 and shown in Eq. 4.4, the relationship between the rate of polymerization and the square root of absorbed light intensity can be expressed as $R_p^{'} = (\Phi k_p^2 / k_t)^{0.5} \times I_{\varepsilon \ell c}^{0.5}$.[26] Plotting $R_p^{'}$ vs $I_{\varepsilon \ell c}^{0.5}$ results in a straight line, where the slope equals $\Phi^{0.5}(k_p / k_t^{0.5})$, as shown in Fig. 4.15, where the experimental results for acrylamide photopolymerization on a SH surface, a H surface and in a vial are plotted. The value of $\Phi^{0.5}(k_p / k_t^{0.5})$ for polymerization on a SH surface (4.8 $L^{0.5}$ $mol^{-0.5}$ $s^{-0.5}$) is close to that on a H surface (4.0 $L^{0.5}$ $mol^{-0.5}$ $s^{-0.5}$). The value of $\Phi^{0.5}(k_p / k_t^{0.5})$ for polymerization in a vial, however, is 2.5 $L^{0.5}$ $mol^{-0.5}$ $s^{-0.5}$, which is significantly smaller. The values of k_p and Φ for these three conditions should be similar as experimental conditions, such as solvent, temperature, and wavelength of UV light, are the same. However, the value of k_t is known to be affected by experimental conditions. In radical polymerization, k_t can be reduced at high conversions, because the viscosity of the solution increases, reducing the mobility of the growing chain radicals.[30] A similar situation has been observed in photopolymerization of thin films, where k_t is reduced at high conversion due to limited lateral diffusion of the chain radicals. With increasing polymerization conversion, a reaction diffusion mechanism occurs,[31] where the growing chain radical is immobilized due to chain entanglements. As a result, the only way the polymer chain radicals can terminate is by monomer addition to the radical chain end. This reaction diffusion mechanism continues until two such growing chains meet and terminate. In a small droplet, where there is no convection, lateral diffusion of the growing chain radicals can also be limited.

This would also lead to termination being dominated by a reaction diffusion mechanism. No increase in solution viscosity would be required since it is the lack of mixing and convection that limits polymer chain mobility.

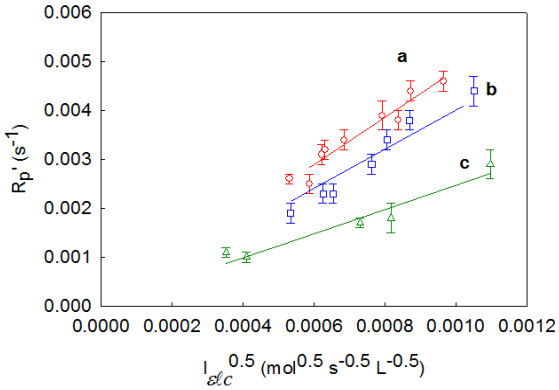

Figure 4.15 Rate of polymerization, R_P', as a function of square root of absorbed light intensity at 25 ℃. (a) (◯) polymerization on SH surface (slope = 4.8 $L^{0.5}$ $mol^{-0.5}$ $s^{-0.5}$, and R^2=0.94), (b) (□) polymerization on H surface (slope = 4.0 $L^{0.5}$ $mol^{-0.5}$ $s^{-0.5}$, and R^2=0.92) and (c) (Δ) polymerization in a vial (slope = 2.4 $L^{0.5}$ $mol^{-0.5}$ $s^{-0.5}$, and R^2=0.94). Lines are forced to pass through the origin.

Based on these results, the molecular weights of polymers were measured to assess the impact of low termination rate. Table 4.5 shows molecular weight of polyacrylamide polymerized to ~18% conversion in three environments. The molecular weights of the polyacrylamide obtained from the SH and the H surfaces are similar when the absorbed UV light are similar; the molecular weight is inversely proportional to absorbed light. The molecular weight of polyacrylamide in the vial is smallest among these three and approximately half the M_n obtained within a droplet on a SH surface. Since the concentration of monomer, initiator and absorbed light intensity is the same for all three environments, these results provide support for a slower termination rate within the droplets relative to the value of k_t in the vial.

To determine the relative values of k_t in these three environments, the values of $1/\Phi^{0.5} \times (k_p / k_t^{0.5})$ can be obtained from Eq. 4.5 and compared to the values of $\Phi^{0.5}(k_p / k_t^{0.5})$ from Fig. 4.15. According to Eq. 4.5, the relation of the average number degree of polymerization and the square root of light absorbed could be described as $\frac{M_o}{M_n} = \frac{(2-a)}{[M]} \frac{k_t^{0.5}}{k_p} \Phi^{0.5} I_{\varepsilon \ell c}^{0.5} + C_M$, where C_M of acrylamide at 25 ℃ is 1.2 $\times 10^{-5}$.[152] In similar free radical polymerization systems of acrylamide in water, coupling of growing chains was the main termination mechanism reported for photopolymerization.[24-26] Akyuz et al. reported the average coupling fraction for termination of acrylamide in aqueous solvent using ultrasonic depolymerization techniques was 0.74.[27] Hence, we assume the coupling fractions of acrylamide in this case is 0.74. The equation $\frac{M_o}{M_n} = \frac{(1.26)}{[M]} \frac{k_t^{0.5}}{k_p} \Phi^{0.5} I_{\varepsilon \ell c}^{0.5} + C_M$ is obtained by substituting this value of 0.74 into Eq. 4.5. In this way, the M_0/M_n values can be related to $1/\Phi^{0.5} \times (k_p / k_t^{0.5})$. The SH surface experiments have the largest average number degree of polymerization of polymers among the three environments as shown in Table 4.6. The smallest M_0/M_n value in Table 4.6 is 4 times of C_M, and so C_M cannot be ignored.

By plotting $1/(M_0/M_n - C_M)$ as a function of $[M]/1.26 * I_{\varepsilon \ell c}^{0.5}$, as shown in Fig. 4.16, the value of $1/\Phi^{0.5} \times (k_p / k_t^{0.5})$ can be determined from the slope. The values of $1/\Phi^{0.5} \times (k_p / k_t^{0.5})$ for polymerization on a SH surface, on a H surface and in a vial are 15, 15, 8.3 $L^{0.5}$ $mol^{-0.5}$ $s^{-0.5}$, respectively. The value in the vial is, as expected, approximately ½ the value in the SH droplet. Comparing with the values of $\Phi^{0.5}(k_p / k_t^{0.5})$ from Fig. 4.15, the Φ value is calculated to be 0.29 ± 0.02. The quantum yield, Φ, is dependent on light wavelength, solvent, and inert gas/nitrogen

environment. The Φ values of Darocur 1173 in presence of oxygen were reported to be 0.15 in *t*-butyl acrylate,[13] 0.2 in methyl methacrylate (MMA),[14] and 0.25 in butyl acrylate.[11] Irgacure 651 (dimethoxyphenylacetophenone, DMPA) has similar structure to Darocur 1173. The Φ values of Irgacure 651 in presence of oxygen were reported to be between 0.1 and 0.4.[10,12] The Φ value of Irgacure 651 in presence of nitrogen was reported to be 0.7.[15] One study, using a fluorescence probe technique, indicated that the quantum efficiency of Darocur 1173 is 0.88 ± 0.03 times that of Irgacure 651.[16] Based on this result, the maximum value of Φ for Darocur 1173 would be 0.62, which is in reasonable agreement with the quantum yield value derived from Fig. 4.15 (0.30). However, the intensity of the UV source at each wavelength is not uniform. Taking into consideration the absorption of 1173 as a function of wavelength, the calculated value of Φ for Darocur 1173 is approximately 0.25 ± 0.04. Since the intensity of the UV lamp as a function of wavelength was not measured (manufacturer's data used), this value of Φ is an approximation.

Table 4.5 The results of photopolymerization of 1.40 M acrylamide and 0.003 M 1173 in water on a SH surface, a H surface and in a vial at 25 ℃.

Environment	Absorbed light intensity[(a)] × 10^7 (mol s^{-1} L^{-1})	Conversion (%)	M_n (GPC) (g mol^{-1})	PDI
SH	5.0	18	1,300,000	1.64
H	5.4	19	1,300,000	1.57
Vial	5.4	20	840,000	1.64
SH	2.6	18	1,700,000	1.74
H	2.4	18	1,700,000	1.72
H	1.9	18	1,900,000	1.66
Vial	1.7	20	1,400,000	1.63

(a) Data were calculated using a 300 nm wavelength.

Based on the $R_i = \frac{-d[I_2]}{dt} = 2\Phi I_{\varepsilon\ell c}$, the concentration of initiator in the droplet on a SH surface under UV of 0.090 mW/cm^2 at 36 s, where conversion is 9% in Fig. 4.10, is 0.00299 mol L^{-1}. The concentration of initiator at 58 s, where conversion is 18%, is 0.00299 mol L^{-1}. The

concentration of initiator in the droplet on a H surface under UV of 0.11 mW/cm^2 at 58 s, where conversion is 9% in Fig. 4.11, is 0.00299 mol L^{-1}. The concentration of initiator at 92 s, where conversion is 18%, is 0.00298 mol L^{-1}. The concentration of initiator at 201 s in the vial under UV of 0.325 mW/cm^2, where conversion is 9% in Fig. 4.14, is 0.00298 mol L^{-1}. The concentration of initiator at 262 s, where conversion is 18%, is 0.00296 mol L^{-1}. To compare these concentrations of initiators at conversion 9% and 18%, concentrations of initiators do not change significantly and hence the kinetic assumptions are valid.

Table 4.6 The molecular weight results of photopolymerization of 1.40 M acrylamide in water on a SH surface at 25℃.

[1173] $\times 10^3$ (mol L^{-1})	Absorbed light intensity[(a)] $\times 10^7$ (mol s^{-1} L^{-1})	R_p' (s^{-1})	M_n (GPC) (g mol^{-1})	PDI	$M_0/M_n \times 10^5$
10	6.2	0.0040	1,100,000	1.65	6.3
10	2.4	0.0026	1,600,000	1.61	4.5
5	5.5	0.0033	1,200,000	1.68	6.0
3	5.0	0.0035	1,300,000	1.64	5.4
3	4.7	0.0034	1,300,000	1.59	5.3
3	3.9	0.0028	1,400,000	1.63	5.1
3	3.6	0.0030	1,400,000	1.63	5.0
3	3.4	0.0026	1,500,000	1.74	4.6
3	3.2	0.0028	1,500,000	1.64	4.8
3	2.6	0.0021	1,700,000	1.74	4.1

(a) Data were calculated using a 300 nm wavelength.

The $k_p / k_t^{0.5}$ values for the reactions in droplets on SH or H surfaces, as well as in the vial are 8.5, 7.7, and 4.6 L$^{0.5}$ mol$^{-0.5}$ s$^{-0.5}$, respectively, based on the square root of product of $1/\Phi^{0.5} \times (k_p / k_t^{0.5})$ and $\Phi^{0.5}(k_p / k_t^{0.5})$. The $k_p / k_t^{0.5}$ values for acrylamide without mixing were reported to be 19 L$^{0.5}$ mol$^{-0.5}$ s$^{-0.5}$ using 0.002 M UO_2^{2+} at 50 ℃,[24-26] 13 L$^{0.5}$ mol$^{-0.5}$ s$^{-0.5}$ using 0.002 M UO_2^{2+} at 20 ℃,[24-26] and 4.7 L$^{0.5}$ mol$^{-0.5}$ s$^{-0.5}$ using 0.002 M H_2O_2 at 25 ℃.[48] The $k_p / k_t^{0.5}$ values in this experiment are reasonable because they are between 13 and 4.7 L$^{0.5}$ mol$^{-0.5}$ s$^{-0.5}$.

The values for Φ and k_p are similar in these three environments and are not expected to influence the calculated values of k_t. The ratio of k_t values is shown in Table 4.7. The k_t value in the SH experiments is the smallest and close to that in the H experiments. The k_t value in the vial experiments is the largest among three.

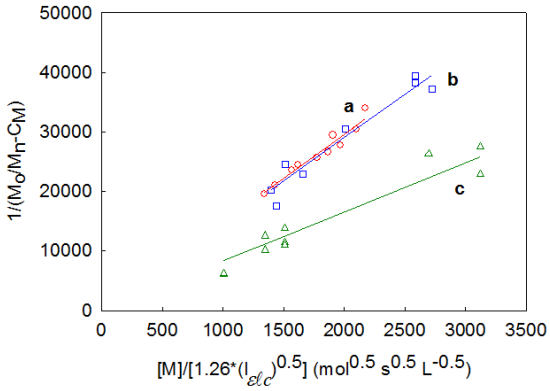

Figure 4.16 The $1/(M_o/M_n-C_M)$ as a function of the concentration of acrylamide and the square root of absorbed light intensity at 25 ℃. (a) (◯) polymerization on a SH surface (slope = 15 $L^{0.5}$ $mol^{-0.5}$ $s^{-0.5}$, and R^2=0.95), (b) (□) polymerization on a H surface (slope = 15 $L^{0.5}$ $mol^{-0.5}$ $s^{-0.5}$, and R^2=0.94) and (c) (Δ) polymerization in a vial (slope = 8.3 $L^{0.5}$ $mol^{-0.5}$ $s^{-0.5}$, and R^2=0.92). Lines are forced to pass through the origin.

Table 4.7 The results of photopolymerization of 1.40 M acrylamide and 1173 in water on a SH surface, a H surface and in a vial at 25 ℃.

Environment	Experiment $k_p(\Phi/k_t)^{0.5}$ $L^{0.5}$ $mol^{-0.5}$ $s^{-0.5}$	Experiment $1/\Phi^{0.5}\times(k_p/k_t^{0.5})$ $L^{0.5}$ $mol^{-0.5}$ $s^{-0.5}$	Average[(a)] $k_p/(k_t)^{0.5}$ $L^{0.5}$ $mol^{-0.5}$ $s^{-0.5}$	Calculation k_t ratio (droplet:vial)
SH	4.8	15	8.5	1.0 (by definition)
H	4.0	15	7.7	1.2
Vial	2.5	8.3	4.6	3.4

(a) Square root of product of $k_p/(k_t^{0.5}\Phi^{0.5})$ and $\Phi^{0.5}(k_p/k_t^{0.5})$.

The reason the k_t values are different in these three environments may be due to the lack of mixing in small droplets which restricts the mobility of chain end radicals. There are two

mechanisms that can cause significant mixing: mechanical stirring and convection. In a vial, the solution is well mixed due to the action of a magnetic stir bar. As the percent conversion is limited to 20%, the viscosity does not increase significantly and so the chain termination rate should not be affected and the reaction rate should follow standard kinetics. However, in a small droplet, no mechanical stirring is possible. Moreover, convection was suppressed as there were no forces available to drive convection. Neither temperature gradients existed, nor significant evaporation occurred in the temperature and atmosphere controlled chamber. In a small droplet, the chain ends can find each other only by diffusion. Convection in the polymerized droplet was monitored as shown in Appendix II. The images and videos of droplets in Appendix II indicate that convection did not obviously appear in the droplets either before or during polymerization. This is consistent with the low Reynolds number of a 2.3 mm droplet (Re = 2 at a velocity of 1×10^{-3} m/s). Only when significant evaporation of water was forced to occur by the flow of dry nitrogen could convection be observed within the droplet.

Because of this static environment, the chain radicals in the droplet can only move by diffusion, thereby lowering the value of k_t compared to a well-mixed system. The diffusion-controlled termination rate coefficient, k_t, is expressed by translational diffusion (TD), segmental diffusion (SD) and chemical reaction (CR), $\frac{1}{k_t} = \frac{1}{k_{TD}} + \frac{1}{k_{SD}} + \frac{1}{k_{CR}}$.[156] Translational diffusion is defined as the movement of one radical through the reaction medium. Segmental diffusion occurs when a segment of a polymer chain moves with respect to another chain, especially when a chain end penetrates another polymer chain to react. Chemical reaction of the two radical sites produces the polymer and terminates the reaction. The reciprocal of the termination rate coefficient is proportional to the sum of the reciprocals of the self-diffusion coefficients of the radicals. In a mixed vial and a static droplet, all three modes of diffusion: translational,

segmental and chemical reaction, occur at similar rates in the two environments. What mixing does change, however, is the frequency at which growing radicals may come sufficiently close that diffusion processes can result in termination.

By comparing the end-to-end distance of the polymer radical with the average distance between radicals, the effect of mixed and static environments can be compared. For example, an acrylamide polymer with a molecular weight of M_n = 840,000 g mol^{-1} was obtained in a polymerization reaction in a vial (Table 4.5). Because the reaction terminated through coupling, the M_n of the combining radicals would be, on average, 420,000 g mol^{-1}. Polyacrylamide with M_n of 420,000 g mol^{-1} has a root-mean-square end-to-end distance $\langle r^2 \rangle^{1/2}$ about 132 nm.[25,157] Diffusivities of small molecules are reported to be between 10^{-6} and 10^{-10} cm^2/s, but that of polymeric species ranges from 10^{-11} to 10^{-13} cm^2/s.[132] The diffusivity of acrylamide (monomer) in 1.40 M acrylamide is 2.54 × 10^{-6} cm^2/s, as calculated using the Einstein-Stokes equation, $D = \frac{kT}{6\pi\eta R}$,[32,158] where k is Boltzmann's constant, T is the absolute temperature, R is the radius of the acrylamide (0.25 nm) and η is the viscosity of 1.40 M acrylamide (0.00344 Pa s, which is calculated from work of Savart et al.[159]). As polymerization conversion achieves 18%, the viscosity of the solution increases to 0.038 Pa s, which is calculated using the intrinsic viscosity and Mark–Houwink parameters[157] as well as the Huggins constant from the specific viscosity plot.[158] Based on the Einstein-Stokes equation[32,158] and the hydrodynamic radius of the polyacrylamide of 40 nm,[160] the diffusivities of acrylamide monomer and polyacrylamide radicals of M_n 420,000 g mol^{-1} would be 2.30 × 10^{-7} and 1.42 × 10^{-9} cm^2/s, respectively. The diffusivity of acrylamide is significantly greater than polyacrylamide.

The number of radicals present at any given time in this 1 mL vial of this solution (assuming a radical lifetime of 1 second) is 2.46×10^{13}, based on the $[R\bullet] = (\Phi I_{abs} / k_t)^{0.5} = R' / k_p$, where R_p' is 0.0018 s-1 and k_p is 4.4×10^4 L mol^{-1} s^{-1}.[26] The volume which one radical would occupy is 4.06×10^{-17} L; this would be equivalent to a sphere with a diameter of 426 nm, which is 3.2 times larger than the average radical end-to-end distance (132 nm[157]) for a radical with M_n = 420,000 g mol^{-1}.The average distance between radicals before termination is 295 nm by comparing the volume occupied with the size of the radical chain. This average separation (295 nm) is smaller than the diffusion length (533 nm), based on $X = (2D \times t)^{0.5}$,[32] where X is the diffusion length, and t is lifetime (t is assumed as 1 s), and so termination by translational diffusion alone would be possible. However, because of mixing in the vial, turbulent random motion in the fluid would increase the frequency of radical-radical encounters and so help explain the relatively higher value of k_t compared to static droplets.

In a static droplet, propagation would continue until the growing radicals diffuse together and combine to terminate as mixing is not available. In the static droplet, where the M_n is ~ 1,300,000, the average radical end-to-end distance is 168 nm[157] and the diameter of the volume occupied by a radical is 342 nm, based on $[R\bullet] = (\Phi I_{abs} / k_t)^{0.5} = R' / k_p$, where R_p' is 0.0035 s^{-1} and k_p is 4.4×10^4 L mol^{-1} s^{-1}.[26] The average separation between radicals is estimated to be 174 nm. As polymerization conversion achieves 18%, where the viscosity of the solution increases to 0.064 Pa s,[157,161] the diffusivities of acrylamide monomer and polyacrylamide radicals of M_n 1,300,000 g mol^{-1} are 1.36×10^{-7} and 6.63×10^{-10} cm^2/s, respectively. This diffusion length of this high molecular weight polyacrylamide radical is 364 nm. The diffusion length (364 nm) is greater than the distance between radicals (174 nm) which is consistent with termination by diffusion. Although both these calculations, in the vial and the droplet, demonstrate radical

termination by diffusion is probable, the calculations are approximate as the lifetime of the radical in this solution is not known. A longer lived radical would be able to diffuse further; one study has shown that the lifetime can be assumed to be as long as 30 seconds at low pH.[48] To explain the higher k_t in the mixed vial, the turbulent random motion caused by mixing would increase the frequency of radical-radical encounters.

The effect of mixing on relative reaction rates has been studied in both the bulk[162] as well as microfluidic applications.[36-43] Ehrfeld et al. demonstrated the effect of mixing in the chemical reaction of KI, KIO_3, NaAc and HCl by examining the effect of mixing in both batch (e.g. beakers) as well as micro-channel reactors.[162] Due to the faster reaction rate of H^+ and Ac^- to that of I^-, IO_3^-, when good mixing is achieved HAc is produced. Otherwise, I_2 and H_2O are generated with poor mixing. By monitoring the concentration of I_2 produced, a qualitative view of mixing quality was achieved. In the batch experiment, the amount of I_2 formation without stirring was three times greater than with heavy stirring. Similarly, when a mixing "tee" was used, the concentration of I_2 observed was 4.5 times greater in the laminar regime (Re = 177) and the turbulent regime (Re = 531). The mixer arrays, having a channel width of 25 - 40 μm, exhibited the least I_2 formation of any system studied. This is because the small scale channels shorten diffusion distances across which the fast reactants (H^+ and Ac^-) are required to travel. The slower/faster reactions reported by Ehrfeld et al.[162] are comparable to the slow/fast diffusion coefficients of monomer and polymer radicals.

In microfluidic channels, the effect of mixing on reaction rates is readily apparent and special mixing channels are required to overcome the lack of mixing in droplets. For example, sinusoidal channels are required in microfluidic systems to insure good mixing.[36] When two separate streams converge into a straight channel, two distinct phases are retained such that Janus

particles can be readily fabricated.[37-43] Figure 4.17 shows that dispersed phases are retained after two separate streams converge and form two aqueous phases in a droplet.[41] This formation of dispersed phases in microfluidic systems is similar to the confluence of two rivers with slow flow rates as shown in Figure 4.18.[171] Without forces that generate mixing (e.g. shear, turbulence, etc.) reaction rates become limited by diffusion. Turbulent random motion increases the frequency of encounters and increases reaction rates.

Thus, for a well-mixed vial, the k_t is higher (by a factor of 3.4) and the average M_n is lower because mixing increases the probability of radical-radical interactions above that from diffusion alone. The difference in diffusion coefficients between monomer and the polymer radical affects the competition between the propagation and termination reactions when external mixing is not available to increase the encounter frequency of the radical chains.

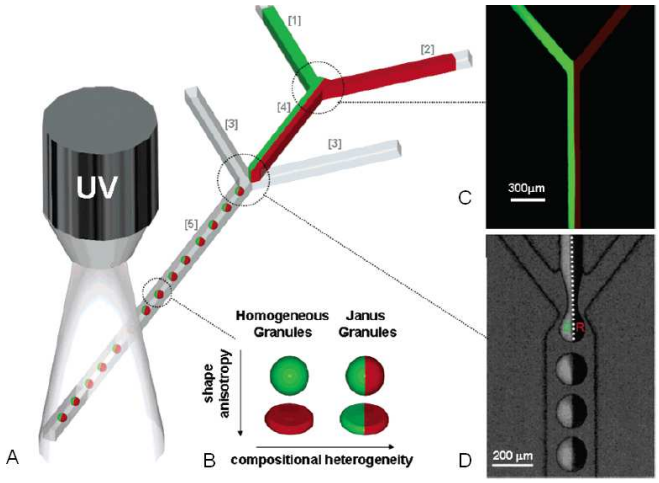

Figure 4.17 (A) Schematic representation of a microfluidic device used to produce Janus particles, (B) schematic view of particles shapes, (C) fluorescent image of formation of dispersed phases after confluence, and (D) backlit fluorescence image of formation of Janus particles.[41]

The static low-viscosity environment is somewhat similar to a well-mixed bulk polymerization, where the viscosity increases rapidly, leading to autoacceleration (or gel effect),

where faster polymerization rates occur. Autoacceleration occurs when the viscosity of the polymerization medium increases, thereby reducing translational motion of the chain ends and forming diffusion-controlled termination. As a result, the termination reaction is slowed, the k_t value decreases, the k_p value is barely affected and so the polymerization rate increases.[11,13] A second consequence is that the molecular weight increases.[134,163] A similar effect is observed in the UV cure of thin coatings,[17] where growing polymer chains near the surface become entangled and cannot diffuse. In such cases, termination occurs by reaction diffusion, where the chain ends must grow into each other. These two effects (increased values of both R_p and M_n) are also evident for the droplet polymerization reactions. The higher rates of polymerization in a droplet compared to the vial are shown in Fig. 4.15. The ~two times increase in M_n within a droplet compared to the vial is evident in Table 4.5. However, the reaction in a droplet is controlled (as opposed to an uncontrolled reaction during autoacceleration) due to the linear relationship between polymerization conversion and time that occurs without an abrupt increase in viscosity.

Figure 4.18 Confluence of the Ohio and Mississippi Rivers at Cairo, IL, USA.[171]

Polymerization in the small static droplets has a special advantage as the molecular weight distribution is not affected by the reduction in the termination rate. The molecular weight

distribution of polyacrylamide in static droplets and the stirred vial are similar as shown in Table 4.5. Therefore, the polymerization in the droplets offers the advantages of high molecular weight and molecular weight distribution control.

The difference between reactions conducted in droplets on superhydrophobic and hydrophobic surfaces is relatively minor. The k_t value for the reactions in droplets on H surfaces is slightly higher than that on SH surface (approx. 20% as shown in Table 4.7). The droplet on the H surface has a large contact area (~760 times the area compared to a droplet on the SH surface) that would facilitate heat transfer across this large interface. One explanation for the higher k_t value in a droplet on a H and SH surface is that temperature gradients in the droplet could develop on the H surface that may cause a small amount of convection to occur, thereby increasing polymer radical encounters. The k_t value in droplets is, however, significantly smaller than the k_t in the well-mixed vial and results in the synthesis of polymers with higher molecular weight.

4.4 Conclusion

A detailed investigation of the kinetics of photopolymerization in a static droplet on superhydrophobic (SH) or hydrophobic (H) surfaces is presented. The effect of light path, absorbed light intensity and initiator concentration on the rate of polymerization was studied. Reaction rates within droplets were found to be about twice as fast as those in a well-mixed vial. The k_t values of polymerization in a droplet on a SH surface or H surface were found to be lower than those in a well-mixed vial. This results in higher effective polymerization rates in static droplets. Higher molecular weights are also achieved in droplets as confirmed using GPC. As essentially no mixing occurs within the droplets, chain ends terminate only through diffusion

processes accounting for the higher polymerization rates and higher molecular weights. These results (higher polymerization rate and higher molecular weight) are similar to a bulk polymerization reaction experiencing autoacceleration or cases were polymerization occurs in confined spaces. However, there are significant differences between polymerization in small droplets and autoacceleration. These include low viscosity and controlled molecular weight distribution in droplets. The measured PDI in droplets is ~ 1.67 which is consistent with the PDI for radical polymerization in well-mixed systems, whereas the PDI in a system experiencing autoacceleration would be significantly greater than 2.[134,163] Limited convection may occur in droplets on a H surface which could account for the 20% higher value of k_t observed in droplets on a H, rather than SH surface. This investigation provides an understanding of polymerization kinetics in a droplet and it also provides new applications of SH surfaces for the synthesis of polymers.

Chapter 5. Conclusions and Recommendations

In this chapter, results of the research project will be summarized and conclusions will be drawn. Recommendations on how to use the obtained experimental results and how to improve the current experimental setup will be presented. Finally, future research in the utilization of micro-dilatometry to study photopolymerization will be proposed.

5.1 Summary

The research presented in this thesis can be summarized as follows:

- The effect of droplet size on the polymerization kinetics and molecular weight was investigated to gain insight into the free-radical photopolymerization mechanism in a small, 10 microliter droplet.
- Micro-dilatometry has the ability to track volume changes of during acrylamide polymerization within an aqueous droplet on a surface inside the environmental chamber with controlled humidity, and hence, can provide a method to monitor polymerization reactions in real time.
- The measurement of the conversion of monomer to polymer in a droplet determined by ^{1}H NMR yielded good agreement with data obtained experimentally by micro-dilatometry up to 18% conversion. The polymerization rates, R_p', were obtained as a function of conversion in time.
- At percent conversions greater than 20%, micro-dilatometry does not accurately measure the percent polymer formed. The volume of the droplet at high conversion decreases not only from monomer contraction during polymerization, but also by water evaporation. This excess evaporation is due to the change in vapor pressure of

water when the number of solute molecules significantly decreased, relative to the reservoirs.

- Kinetic studies were performed and indicate that the faster polymerization rates and higher molecular weights that are observed in small droplets are due to a reduced termination rate constant. This result from the lack of mixing/convection within the droplet, which reduces the rate at which growing chain ends, can diffuse, couple and terminate.
- Polymerization in a droplet provides low k_t that cannot be easily obtained using other techniques commonly employed to study photopolymerization.

5.2 Conclusions

Studying polymerization reactions in isolated single droplets is challenging. For example, the percent conversion of polymerization in droplets in a microfluidic system was studied by Raman spectroscopy, but the reaction was not followed in real-time. On open surfaces, evaporation rates of small droplets pose a greater challenge and the presence of oxygen must be excluded. To address these issues, an environmental chamber was designed and built that incorporated thermal control as well as solution reservoirs to stabilize the vapor pressure of the solvent in this sealed environment. As a result, the volume of droplets could be made to be stable over long periods of time (>10 minutes with <0.2% change). The change in droplet volume that occurs during polymerization can then be accurately measured to a volume of ± 0.01 μL. By knowing the contraction factor for a polymer, the rate of reaction can be followed in real-time by monitoring the image of a droplet. By purging the chamber with nitrogen before forming

droplets, oxygen can be excluded such that induction times are kept short (typically <30 s) and so the initial concentration of initiator is constant.

Micro-dilatometry tracked volume changes of the acrylamide droplet with Darocur 1173 on a surface as a function of time and offered a novel way to study the kinetics of acrylamide photopolymerization. Polymerization conversion from micro-dilatometry was confirmed by ^{1}H NMR at conversions up to 18%. An increase in the polymerization rate was observed as a function of UV intensity and Darocur 1173 concentration. These results show that micro-dilatometry conducted in an environmental chamber with reservoirs to control vapor pressure of solvent have the ability to provide valuable data for the analysis of acrylamide polymerization. In addition, micro-dilatometry has the ability to monitor the droplet on superhydrophobic or hydrophobic surfaces. Significantly polymerized droplets did not have strong adhesion to either of the two type surfaces and could be completely removed by using a syringe for further analysis when conversion is below 18%.

The conversion difference between micro-dilatometry data and NMR data increases with the increase polymerization conversion above 18%. This result indicates droplet gradually evaporates. The reasons of the evaporation of droplet was studied and found to be caused primarily by the composition change of the droplet. As the monomer polymerizes, the number of solute molecules decrease rapidly leading to an increased vapor pressure of water as predicted by Raoult's law. Since the composition of the solvent reservoirs do not change during the photopolymerization reaction, the relatively higher vapor pressure of water in the droplet causes the droplet to shrink. The heat of polymerization may also contribute to this excess evaporation. These experimental results indicate the limit of micro-dilatometry beyond 18% conversion.

Kinetic studies of photopolymerization were performed for the acrylamide system on both superhydrophobic and hydrophobic surfaces and compared to the results for a well-mixed vial. The path length of light transiting through a droplet was calculated so that the absorbance of the photoinitiator could be determined in the spherical and hemispherical geometries of droplets on these two types of surfaces as well as in the cylindrical vial. The results show that, as expected, the polymerization rate is proportional to the square root of the absorbed UV intensity of Darocur 1173. In comparison with reactions in a well-mixed vial, the polymerization rate in the droplets is approximately twice as fast. The results in Fig. 4.15 provide a good understanding of how the reaction kinetics, shown in Eq. 4.4, are affected by the environment. The values for $\Phi^{0.5}(k_p/k_t^{0.5})$ for droplets on a superhydrophobic surface are shown to be smallest among these three environments with the value for a droplet on a hydrophobic surface only 8% lower. In contrast, the value in the vial was half as large. The molecular weight data of polymerized droplets and 1 mL polymerized solution as a function of square root of the absorbed UV intensity provides confirmation and are shown in Fig. 4.16. The faster polymerization rates and higher molecular weight in the droplet are caused by low diffusion of polymer chain radicals leading to reduced termination rates.

In conclusion, micro-dilatometry is an effective tool for monitoring the photopolymerization process. The study of polymerization in isolated single droplets conducted in this thesis demonstrates that termination rates can be reduced when convection is absent in a low viscosity solution. This leads to faster rates and high molecular weight polymers while maintaining relatively narrow molecular weight distributions.

5.3 Recommendations

The above presented research has demonstrated that measuring the change in volume by micro-dilatometry can be used to monitor the photopolymerization of 1.40 M acrylamide droplets using Darocur 1173 as the initiator. The resolution of this technique is limited due to the limits of the magnification and imaging system. A higher magnification lens and higher resolution camera would improve the resolution of the system beyond the current 0.01 μL limit. Excess evaporation of the droplet resulting from the change in the number of solute molecules remains a challenge for following reactions by micro-dilatometry beyond 18% conversion. A system for controlling the vapor pressure of water in the chamber would extend the range of applicability. For example, the concentration of the reservoir could be varied over the course of the reaction. Alternatively, the concentration of acrylamide could also be decreased. This would have several advantages, such as decreasing the composition deference in vapor pressure between the polymerized droplet and the reservoirs, as well as decreasing heat released by the exothermic polymerization. However, a higher resolution imaging system would be required to detect the smaller changes in volume corresponding to the lower concentration.

Holtze et al. reported the fabrication of ultra-high molecular weight polystyrene using a free radical miniemulsion polymerization, as well as cycles of short microwave times and ice-bath black period.[46] Their mechanism of miniemulsion polymerization is shown in Fig. 1.9. High molecular weight was obtained due to low transfer limit of polystyrene at low temperature. Currently our environmental chamber has ability to stabilize droplet volume between 15 and 35 ℃. By increasing the thermal insulation of the chamber, experiments could be conducted at temperature approaching 0 ℃ and a pulsed laser light source could be used. This approach could

lead to higher molecular weight of polyacrylamide in the droplet as well as determination of k_t and k_p values directly.

5.4 Future Research

Micro-dilatometry has ability to monitor photopolymerization reactions in a droplet with contact angles from 90 to 155° on a surface at 25 ℃. The environmental chamber shows the ability to maintain droplet volume stability at a range of 15 and 35 ℃ in an inert gas ambient. This technique opens a new method to fabricate polymers and study their kinetics when diffusion of large polymer chains is limited but viscosity remains low. Acrylamide is only one water-based monomer and can be replaced by other water-based monomers, such as 2-hydroxyethyl methacrylate (HEMA).[164] HEMA is widely used in free-radical photopolymerization processes. To avoid PHEMA precipitation from water, the water can be mixed with a co-solvent[165] and maintain the droplet on a superhydrophobic surface. Further, micro-dilatometry could be utilized for research in water-based copolymers.

Micro-dilatometry could also be used to study monomers and polymers that are soluble only in non-aqueous solvents by a new syringe technique[166] for fabrication of oil-based polymers, such as polystyrene.[167] The syringe includes two size tubes and is controlled by syringe pump. Water and anisole flow through the outer and inner tube, respectively, and a droplet, where water surrounds anisole, forms and is placed on a surface. Anisole with density of 0.995 g/mL at 25 ℃ and refractive index 1.5126 is used because its properties are close to water. Water-based initiators or oil-based initiators could be used. During photopolymerization, shrinkage caused by the formation of polymers would decrease the volume of the droplet. This method makes

possible the fabrication of oil-based polymers in a aqueous droplet on a surface and so further extend the applications of micro-dilatometry.

Appendix I. The Principle and Measurement Accuracy of Micro- Dilatometry

The aim of this appendix is to explain the principle which is used by the goniometer software to calculate the volume of droplets used for micro-dilatometry, and also to determine the accuracy of micro-dilatometry for measuring the height and volume of liquid droplets.

I.1 Measurement Method: Contact Angle Goniometer

For droplets on a surface, a backlit image is recorded using the digital camera of a contact angle goniometer from ramé-hart (Model 250). Two horizontal baselines (pink and green lines) and one vertical line (a red line) are set by the operator to identify the apex and the base of the drop surface so that the software can more accurately measure the height and width of the droplet (Fig. I.1).[168]

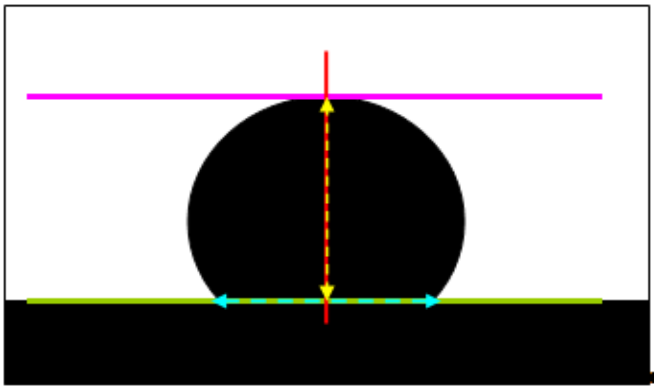

Figure I.1 Schematic of image of a sessile droplet with two horizontal baselines and one vertical baseline positioned.

I.2 Calibration

Pixel dimensions are determined by the calibration process. In the calibration process, a sphere of known diameter is mounted on a clear substrate which is held vertically such that the sphere profile can be recorded by the goniometer measurement system without interference from a solid substrate. The sphere is backlit and focused by manually adjusting the position of the sample stage. A digital image is captured from the live video stream and the number of horizontal (orange dotted line in Fig. I.2) and vertical (yellow dotted line) pixels of the image are determined. The sizes of the horizontal and vertical pixels are calculated, based on the known sphere diameter, and stored for future dimensional measurements. The ratio of horizontal and vertical pixel dimensions should be close to 1.000 and is monitored to insure accuracy and consistency.

The vertical and horizontal pixels were first calibrated using the sphere calibration tool (4.000 mm steel ball bearing glued to a glass slide) supplied with the instrument. This sphere was placed on the sample stage of the contact angle goniometer and a backlit image was taken with the camera (Fig. I.2). The vertical pixel, horizontal pixel, and the aspect ratios obtained were 10.664 μm, 10.651 μm and 1.0012, respectively.

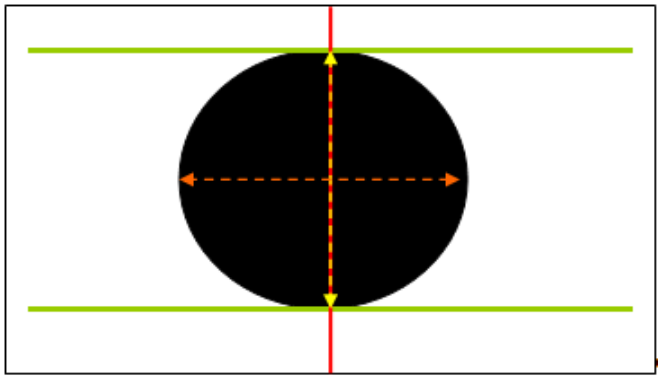

Figure I.2 Schematic image of the sphere calibration tool with two horizontal baselines and one vertical baseline positioned.

I.3 Measurement

To measure the volume of a liquid droplet on a surface, the droplet is placed on the appropriate surface and a backlit image is recorded and the horizontal and vertical baselines are positioned as described in the previous section. The program identifies the edge of the droplet by finding the highest contrast between bright and dark pixels. Height and width of the droplet are calculated from the experimental profile. The height (a yellow dotted line in Fig. I.1) and width (a blue dotted line) of a droplet are determined by multiplying of the numbers of pixels along the yellow and blue dotted lines by the pixel dimensions. For example, the width of the droplet in Fig. 2.7B is 1.767 mm, which is smaller than its diameter 2.5 ± 0.02 mm.

The volume of the droplet is calculated from the drop profile determined by the software. The program places hundreds of points around the drop perimeter and a fourth order polynomial is fit to these points to accurately describe the curve. The polynomial is then integrated to calculate the volume of the droplet.[118]

I.4 Precision and Accuracy Test for the Known Sphere Calibration Tools

The precision and accuracy of the instrument for determining the dimensions of the sphere calibration tools were determined using three different sphere calibration tools, made by adhering stainless steel ball bearings to glass slides. The 4.000 mm and 1.000 mm spheres were supplied by ramé-hart. The 2.500 mm sphere was prepared for this experiment as it is similar to the diameter of a 10.00 μL droplet (2.667 mm), in which the polymerization reaction is performed. After calibration for these spheres was performed, these spheres were placed in the same position and measured for 10 times without refocusing. The diameters of three sphere calibration tools were 4.000 ± 0.000 mm, 2.500 ± 0.000 mm and 1.000 ± 0.000 mm, respectively.

To determine the effect of manually focusing, the calibration and diameter measurements were repeated after first refocusing before each measurement. After refocusing and measuring 10 times, the size of vertical pixels of three sphere calibration tools with 4.000 mm, 2.500 mm and 1.000 mm were 10.664 ± 0.037 μm, 10.664 ± 0.024 μm and 10.791 ± 0.033 μm, respectively. The diameters of three sphere calibration tools were 4.000 ± 0.014 mm, 2.500 ± 0.006 mm and 1.000 ± 0.003 mm, respectively. The accuracies among three measurements are similar and in excellent agreement with actual values. The measurement precision for calibration tools with 4.000 mm and 2.500 mm diameters was lower than that for the tool with 1.000 mm diameter due to difficulties in focusing on the larger spheres. Therefore, the main source of error is caused by the refocusing process.

Thus, the goniometer is an effective measurement system for 10 μL droplets. During a micro-dilatometry experiment the droplet only needs to be focused once before the initial measurement. Subsequent measurements do not require refocusing and so, based on these calibration measurements, the repeatability of the droplet volume measurement is expected to be the same as the calibration spheres without refocusing (i.e. better than ± 0.001 mm).

I.5 Accuracy Test for a Transparent Sapphire Ball on a PDMS Surface

The volume accuracy of the goniometer was further verified by using a sapphire spherical ball lens placed on a flat surface. The sphere, with a diameter of 2.779 mm, is similar to the diameter of the water droplets used for micro-dilatometry experiments. The volume is 11.23 μL. The sphere was placed on a flat PDMS surface on the stage of the goniometer and focused. After refocusing and measuring 10 times, the measured volume of the ball was determined to be 11.11 ± 0.04 μL. The relative error of volume of the sphere on this hydrophobic surface is 1%. One

reason to explain this error is that some portion of the backlit image of the sphere was blocked by the soft PDMS surface. The precision of ± 0.04 μL is comparable to that found for similarly sized calibration sphere measurements subject to refocusing. Without refocusing, the volume of the sapphire sphere does not change and was 11.11 ± 0.00 μL.

I.6 Accuracy Test for Known Volume Water Droplets on a Surface

The measurement accuracy of known volume water droplets on a surface was obtained using both a ramé-hart automated dispensing system and a 100 μL glass syringe (Hamilton) with a 22 gauge needle. The minimum resolution of the automated dispensing system is reported to be ± 0.01 μL.[168] A droplet of 10.00 μL was placed on the surfaces using the automated dispensing system and its volume measured using the goniometer. Ten droplets were measured on each surface and the values were averaged. The measured volume of the droplets on a flat hydrophobic and superhydrophobic surface was 10.35 ± 0.06 μL and 10.08 ± 0.04 μL, respectively. After refocusing the imaging system, the volume of the water droplets on a hydrophobic and superhydrophobic surface was determined to be 10.54 ± 0.08 μL and 10.17 ± 0.06 μL, respectively. Refocusing after each drop decreased the accuracy and precision; the percent error on a flat hydrophobic and superhydrophobic surface was 5.4% and 1.7%, respectively (Table I.1). The accuracy of a volume measurement on a superhydrophobic surface (with a contact angle of about 160°) was found to be higher than on a hydrophobic surface (with contact angle of about 90°). This may be due to the smaller liquid-solid contact area on the superhydrophobic surface such that nearly the entire droplet perimeter is clearly visible.

To estimate the repeatability of the measurement of water droplet volume, measurements were repeated without refocusing. To minimize the effect of evaporation, which would cause the

drop to shrink over time, the droplets were maintained in the environmental chamber in an atmosphere equilibrated with water vapor. The volume of the droplet remained stable for 10 min. After 10 measurements (recorded once every 2 s) without refocusing, no change in droplet volume was observed as shown in the second column of Table I.1.

Table I.1 The percent difference of 10.00 μL droplet for difference source from Micro-dilatometry measurement.

10.00 μL Droplet	Percent error in volume (%)	Percent error in volume from continuous measurement (%)
On a flat hydrophobic surface using the automated dispensing system	5.4	0
On a flat superhydrophobic surface using the automated dispensing system	1.7	0
On a flat hydrophobic surface using 100 μL syringe	5.5	0
On a flat superhydrophobic surface using 100 μL syringe	2.0	0

The resolution of the 100 μL glass syringe is reported to be ± 1 μL.[169] A 10 μL droplet was placed on the surfaces using the 100 μL glass syringe and measured. After measuring 10 droplets, the measured volume of the droplets on a flat hydrophobic and superhydrophobic surface was determined to be 10.55 ± 0.10 μL and 10.20 ± 0.07 μL, respectively. The percent error of volume of droplets on a flat hydrophobic and superhydrophobic surface from refocusing is 5.5% and 2.0%, respectively. These values are better than the resolution of the syringe ± 1 μL (or 10% of a 10 μL drop). The results indicate that both the accuracy and precision of the automated dispenser and manual syringe are very similar (e.g. 10.17 vs 10.20 μL with standard deviation of 0.06 vs 0.07 μL respectively on a superhydrophobic surface). The reasons are that the gauge of the

needle increases the error of automated dispenser system as well as the careful injection reduces the error of manual syringe.

I.7 Conclusion

The width and height from micro-dilatometry is based on the number and size of pixels obtained from a backlit image of a droplet. The volume values were obtained by calibrating the size of pixels on the imaging system as well as by determining a best-fit fourth-order polynomial to the shape of the droplet curve. This polynomial is then integrated to determine droplet volume. The accuracy of measuring the diameters of suspended metal sphere calibration tools is very high; mean values of the diameters of metal spheres were better than 0.001 mm. For the calibration standards, repeatability of the diameter and volume measurements is excellent (<0.001 mm / 0.01 μL). Focusing of the imaging system on the droplet perimeter causes errors of 0.35%, 0.2%, and 0.3% for the 4.000, 2.500 and 1.000 mm diameter metal spheres, respectively. The precision of the diameter measurements increased with decreasing sphere diameter, ranging from 0.014 to 0.003 mm. The main source of source of this reduced precision was shown to be the refocusing processes.

The volume accuracy of the instrument was also verified using a 11.23 μL sapphire ball on a flat PDMS surface. The advantage of this sapphire sphere is that there is a better match to the optical properties (compared to steel spheres) of water droplets on a superhydrophobic surface while maintaining a perfectly spherical shape that is not affected by evaporation. The measured value was 1% less than the measured value (11.11 μL measured (calculated diameter: 2.769 mm) vs 11.23 μL actual (diameter: 2.779 mm)). This lower value may be due to the backlit image of the sphere being partially covered by the soft PDMS surface. Without refocusing, the

repeatability of the volume measurement is excellent with no changes observed after 10 measurements.

The accuracy of volume measurements for 10 μL water droplets on surfaces was estimated using an automated dispensing system to produce 10 μL droplets. The accuracy of a droplet volume measurement on a superhydrophobic surface (contact angle of about 160°) is higher than for a droplet on a hydrophobic surface (contact angle of about 90°). The accuracy is 1.7% vs 5.4% for these types of surfaces. The lower accuracy of water droplets, compared to calibration spheres results from a combination of dispensing errors, focusing errors, evaporation, and occlusion of the water-liquid interface by the substrate (especially for the hydrophobic surface). In addition, there was no way to independently verify the true size of dispensed drops. The drop volume was determined by the displacement of a plunger by a computer controlled stepping motor in a positive displacement pump. However, calibration of this small displacement was not verified. In addition, bubbles in the system between the pump and dispensing needle could reduce accuracy. The accuracy and repeatability of the volume measurement of droplets formed from a 100 μL syringe was comparable to the automated dispensing system in spite of the limited resolution of the syringe and potential for manual errors. The results indicate that both the accuracy and precision of the automated dispenser and manual syringe are very similar because the gauge of the needle increases the error of automated dispenser system as well as the careful injection reduces the error of manual syringe.

Overall, these results indicate that the measurement system can measure ***changes*** in the volume of water droplets with a precision of approximately 0.001 mm (or 0.01 μL). The absolute accuracy of the volume measurement is affected by several sources of error including focusing, ambiguity of the location of the liquid-solid interface, and standards for liquids droplets. This

limits absolute accuracy of the total volume of a water droplet to approximately 1.7% on a superhydrophobic surface and approximately 5.4% on a hydrophobic surface.

Appendix II. Convection in a Small and Isothermal Droplet

The purpose of this appendix is to investigate convection phenomena in small, isothermal droplets both in an open system and in an environment with high relative humidity, where the volume of the droplet is stable, especially when an exothermic reaction is performed in the droplet.

II.1 Introduction

The polymerization of acrylamide is an exothermic reaction ($\triangle H_p$ = 81.6 kJ/mol). When this polymerization reaction is performed in a small droplet, the generated heat is gradually transferred to the environment via conduction, convection, and/or evaporation of the solvent. In the chapter 3, the temperature of droplet during polymerization did not have significant change. However, due to vapor pressure in the chamber during polymerization, the evaporation of droplet obviously appeared beyond 18% conversion. Owing to the mass transfer and latent heat of vaporization, evaporation of the solvent decreases the surface temperature of the droplet to generate temperature gradients that can cause convective flow in the droplet. The effect of the convective flow in the droplet during the polymerization reaction is analogous to stirring in the bulk and would increase mixing and the mobility of chain radicals. In contrast, in a droplet without convection, the radicals would be relatively immobile and their movement would be restricted to diffusion.

The convective flow inside droplets is created by density differences in the fluid occurring due to temperature gradients as well as mass transfer from the droplet to the gas phase.[94] The flow velocity decreases with increase of relative humidity, which reduces evaporation of a water-

based droplet.[47,94] Hence, convective flow is expected to occur inside a small droplet when exposed to open air where the driving force for evaporation is greatest. Convective flow would not occur inside the droplet when the vapor pressure of the droplet is in equilibrium with its surroundings, such as in an environmental chamber with solvent reservoirs.[47,94]

To verify the absence of convection in small droplets in the micro-dilatometry system, a 10 μL water droplet on a flat superhydrophobic surface was observed under the following five conditions:

(a) pure water droplet in open air where evaporation can occur freely,

(b) pure water droplet in an environmental chamber which is opened to the air and with solvent reservoirs present,

(c) pure water droplet in a closed environmental chamber with solvent reservoirs,

(d) pure water droplet in a closed environmental chamber with solvent reservoirs and irradiated with UV light (0.2 mW/cm^2), and

(e) droplet of acrylamide solution (1.40 M in water) with initiator in a closed environmental chamber with solvent reservoirs under UV light (0.2 mW/cm^2).

II.2 Experiments

In all cases, backlit images of 10 μL droplets were recorded using the contact angle goniometer.

II.3 Results

Convection in a droplet is expected to occur when the droplet is sitting on a superhydrophobic surface in an open system. Backlit images of a droplet on flat superhydrophobic surface (without the environmental chamber) are shown in Fig. II.1. The droplet in such environment is evaporating quickly such that convection occurs. In order to indicate the convection flow more clearly, the images of the droplet at 5 s and 6 s are shown. Within the same location (red circle), dust particles are observed to move during the one second interval from 5 s to 6 s. Arrows in these Figures point to the position of the particles. The convective flow in the water droplet is very obvious as these small dust particles can be easily seen to move around the droplet.

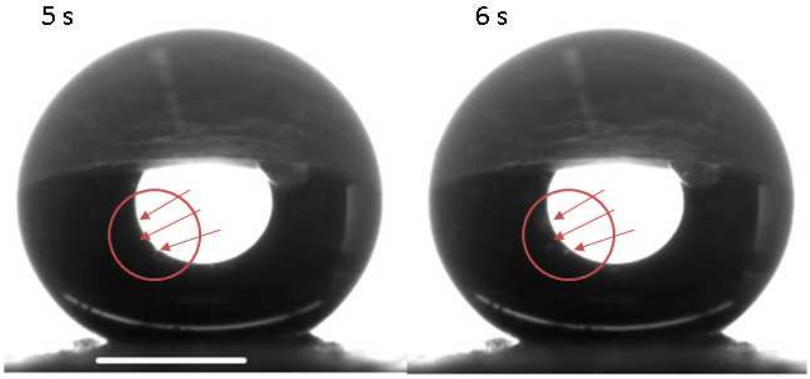

Figure II.1 Backlit images of pure water in open air.

Convection generated by evaporation is expected to decrease as the relative humidity increases. Convective flow within a droplet on a SH surface with reservoirs in an opened chamber was investigated and backlit images of the droplet are shown in Fig. II.2. In this more controlled environment, evaporation is limited and small particles can, on rare occasions, be seen to drift slowly across the droplet.

When the environmental chamber was sealed and the vapor pressure was in (or close to) equilibrium, no evaporation was expected. Backlit images of water droplets on a surface with reservoirs inside a sealed chamber without UV or under UV irradiation are shown in Fig. II.3 and Fig. II.4, respectively. No movement of particles inside the droplets was observed in either condition.

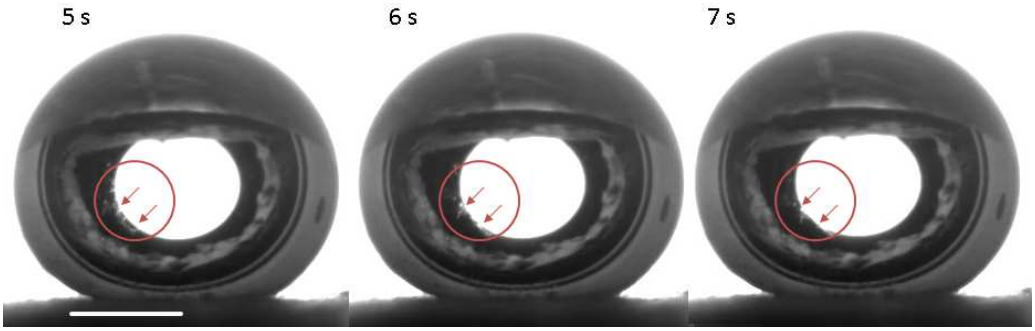

Figure II.2 Backlit images of pure water in an environmental chamber. Slow movement of particles was observed.

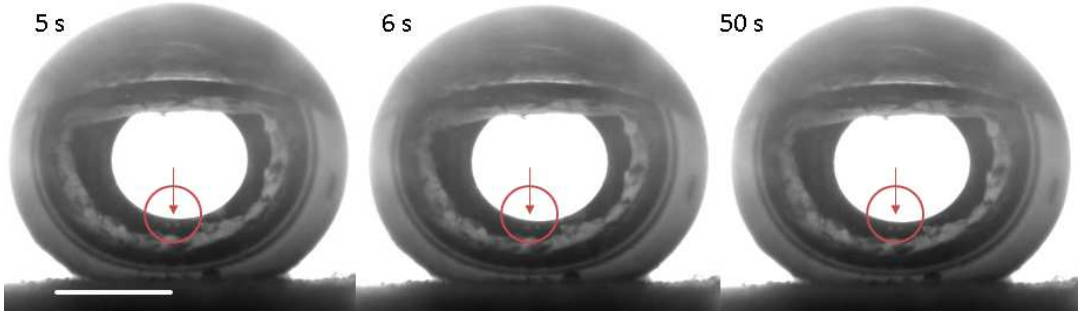

Figure II.3 Backlit images of pure water in a closed environmental chamber with solvent reservoirs.

In the fifth example, a droplet undergoing polymerization within the equilibrium conditions in the environmental chamber was studied. In this case, the exothermic polymerization reaction and/or excess evaporation from the increasing vapor pressure of water within the droplet could drive convection. Several periods during the polymerization were studied. At first, before polymerization, no evaporation occurs in the sealed chamber as the vapor pressure of the droplet was in equilibrium with the chamber. Secondly, as the polymerization reaction proceeds, some

heat is generated, albeit at a relatively modest rate. When the percent conversion to polymer is below 18%, evaporation does not occur to any significant extent (the % conversion measured by micro-dilatometry agrees well with the % conversion by NMR) and thus convection in the droplet is not expected to occur. Thirdly, when the percent conversion to polymer exceeds 18% evaporation does occur due to a combination of the heat of polymerization and the increased vapor pressure of water in the droplet due to its significantly reduced number of monomer (solute) molecules (i.e. Raoult's Law). Although convection in the droplet could occur above 18% conversion, it may not occur to a significant extent for two reasons. First, the viscosity of the droplet will have increased, reducing the internal flow rate. In addition, the temperature gradients may not be sufficient to drive significant convection.[92] No movement was observed in backlit images of droplets at about 30% conversion, as shown in Fig. II.5. Fourthly, when the percent conversion to polymer in a droplet exceeds a certain percentage (~50%), evaporation will increase, but the viscosity of the droplet will increase significantly, such that the droplet becomes a gel at 80% conversion. At such high viscosities, convection in the droplet cannot occur.

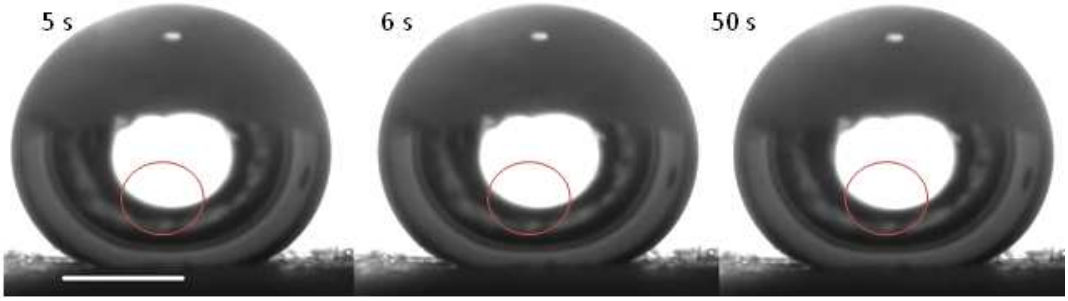

Figure II.4 Backlit images of pure water in a closed environmental chamber with solvent reservoirs under UV light (0.2 mW/cm^2).

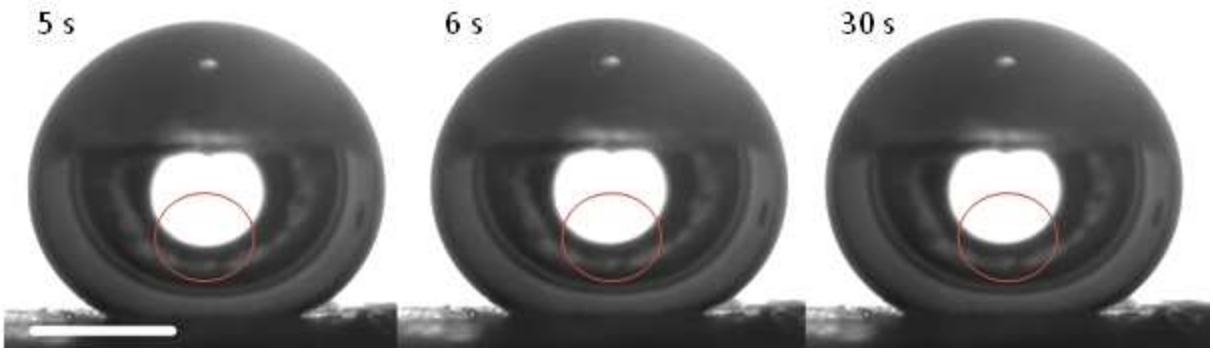

Figure II.5 Backlit images of acrylamide solution (1.40 M in water) with initiator in a closed environmental chamber with solvent reservoirs under UV light (0.2 mW/cm^2).

II.4 Conclusion

Convective flow does not appear to any significant extent when droplets are placed on a superhydrophobic surface in a sealed environmental chamber with reservoirs. This is because, at steady state, evaporation and condensation achieve equilibrium. Also, because the temperature of the chamber is well controlled, there are no thermal gradients large enough that could drive convection.

During the polymerization reaction, heating does occur, but thermal gradients and evaporation are minimal during the initial stage (first 18% conversion) of the reaction. At higher conversions, convection may still not occur as the temperature gradient would be spherically symmetrical. Even if thermal gradients did occur, the increased viscosity at higher percent conversion would restrict convective flow from occurring. Although no obvious convection was observed, slow rates of convection may be difficult to observe in this experimental apparatus. These observations are consistent with our expectations and with the literature.[170]

Appendix III. Calculation of Reflected and Refracted UV Light Percent as well as Path Length for Droplet

Light illuminates only the upper half of the nearly spherical surface of a droplet on a superhydrophobic surface. Similarly, it illuminates the entire liquid-air interface for a droplet on a hydrophobic surface. To calculate the fraction of light entering the droplet, the percent reflected light must be calculated. The reflectance, ρ, is as a function of the incidence angle and refraction angle.[154]

$$\rho = \frac{1}{2}\left[\frac{\sin^2(\theta_i - \theta_r)}{\sin^2(\theta_i + \theta_r)} + \frac{\tan^2(\theta_i - \theta_r)}{\tan^2(\theta_i + \theta_r)}\right] \tag{4.6}$$

where θ_i is incident angle and θ_r is refraction angle which is calculated using Snell's law, $sin\theta_i$ / $sin\theta_r = n_2 / n_1$, where n is the refractive index of the medium.

Assuming the incident light is normal to the substrate and since the surface of the droplet is curved, the incident angle will vary across the droplet. To calculate the reflectance, the surface was sliced up into small polygonal surfaces such that the reflectance could be calculated for a fixed incident angle. Two regions of polygons were created. At the apex of the droplet, a circular area (0.1 degree included angle from the center of the sphere) was defined. This circular area was divided into 360 triangles, one per degree, as shown in Fig. 4.8B. The remainder of the sphere was divided into bands that are concentric with this circle; each of these bands was split into polygons 1° wide, forming 360 polygons/band as shown in Fig. 4.8C (32,400 trapezoids total between incident angles of 0.1° and 90°).

To calculate the percent of incident light falling on a polygon, a projection of the light onto the 2-D substrate is first calculated. For a triangular polygon in the central circle (Fig. III.1A) the incident surface is defined by the curved surface TSP and the projected area is TDP. Since these polygons are near the apex of the curved surface, the incident and project surfaces are almost the same. The segment $\overline{AO}$ is the radius (R), $\overline{AD}$ would be Rsin(0.1°). The area of Triangle TDP is $1/2\times\overline{AD}\times\overline{TP}$, where $\overline{TP}$ is 1/360 of circumference with radius of Rsin(0.1°).

For the trapezoidal polygons composing the concentric bands, QVWX in Fig. III.1B is one of 32400 trapezoidal polygons with θ_i between 0.1° and 90°. Trapezoid QYZX in Fig. III.1B is the 2D projected area of trapezoid QVWX. The segment $\overline{EO}$ is R, $\overline{GH}$ and $\overline{EK}$ would be Rsin(θ_i) and Rsin(θ_{i+1}), respectively. The area of trapezoid QXYZ is $1/2\times(\overline{YZ}+\overline{QX})\times\overline{EJ}$, where $\overline{YZ}$ is 1/360 of circumference with radius of R$sin(\theta_i)$, $\overline{QX}$ is 1/360 of circumference with radius of R$sin(\theta_{i+1})$, and $\overline{EJ}$ is equal to (R$sin(\theta_{i+1})$- R$sin(\theta_i)$).

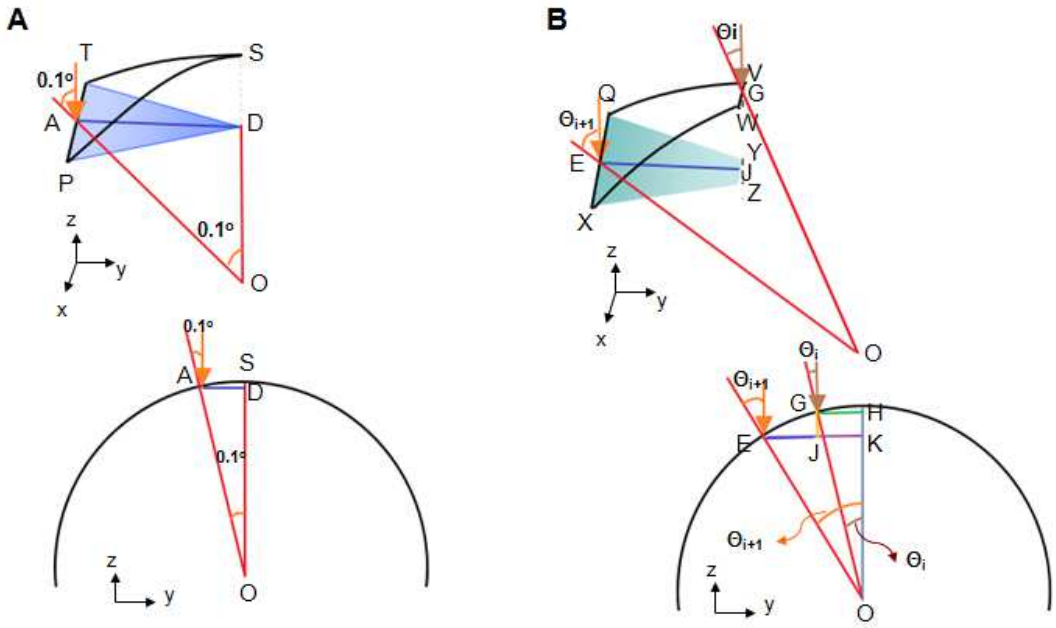

Figure III.1 Schematic of illuminated area calculation for droplet experiments. (A) Incident angle of 0.1°. (B) Incident angle between 0.1° and 90°.

III.1 Percent of Light Reflected for a Superhydrophobic Droplet

A. Reflectance from a superhydrophobic droplet. Light enters a 10 μL 1.40 M acrylamide droplet (R = 0.134 cm) on a superhydrophobic surface: Since UV light uniformly illuminates the droplet from above, the light rays can be assumed to be parallel (perpendicular to the substrate) with a range of incident angles between 0 and 90°. For a given polygon, the fraction of reflected light is calculated at a given incident angle (θ_i) using Fresnel equation (Col 3). The incident light at θ_i is determined from the projected area at θ_i (Col 4) and multiplying by 360 to determine the total projected area at θ_i (Col 5). The total fraction of reflected light at θ_i (Col 6) is calculated by multiplying (Col 3) by (Col 5). The average fraction reflected from the droplet is then the sum of Col 6 divided by the sum of Col 5. The refractive indices of N_2 and 1.40 M acrylamide are 1.00 and 1.35, respectively. The percent of light reflected is calculated to be 7.17% of incidence energy in Table III.1.

Table III.1 The calculation of light reflected for a 10 μL 1.40 M acrylamide droplet as light enters droplet.

Col 1	Col 2	Col 3	Col 4	Col 5	Col 6
Incident angle, θ_i	Refraction angle, θ_r	ρ fraction reflected	Projected area from one polygon	Total project-ed area at incident θ_i	ρ for total projected area at incident θ_i
degrees	degrees		cm^2	cm^2	cm^2
0.100	0.074	0.0222	4.77E-10	1.72E-07	3.81E-09
1.00	0.741	0.0222	4.72E-08	1.70E-05	3.77E-07
2.00	1.48	0.0222	1.43E-07	5.14E-05	1.14E-06
3.00	2.22	0.0222	2.38E-07	8.57E-05	1.90E-06
4.00	2.96	0.0222	3.33E-07	1.20E-04	2.66E-06
5.00	3.70	0.0222	4.27E-07	1.54E-04	3.41E-06
6.00	4.44	0.0222	5.21E-07	1.88E-04	4.16E-06
7.00	5.18	0.0222	6.14E-07	2.21E-04	4.91E-06
8.00	5.92	0.0222	7.07E-07	2.54E-04	5.64E-06
9.00	6.65	0.0222	7.98E-07	2.87E-04	6.38E-06
10.0	7.39	0.0222	8.89E-07	3.20E-04	7.10E-06
11.0	8.13	0.0222	9.79E-07	3.52E-04	7.82E-06

12.0	8.86	0.0222	1.07E-06	3.84E-04	8.53E-06
13.0	9.59	0.0222	1.15E-06	4.15E-04	9.23E-06
14.0	10.3	0.0222	1.24E-06	4.46E-04	9.92E-06
15.0	11.1	0.0222	1.32E-06	4.77E-04	1.06E-05
16.0	11.8	0.0223	1.41E-06	5.06E-04	1.13E-05
17.0	12.5	0.0223	1.49E-06	5.35E-04	1.19E-05
18.0	13.2	0.0223	1.57E-06	5.64E-04	1.26E-05
19.0	14.0	0.0223	1.64E-06	5.92E-04	1.32E-05
20.0	14.7	0.0224	1.72E-06	6.19E-04	1.38E-05
21.0	15.4	0.0224	1.79E-06	6.45E-04	1.45E-05
22.0	16.1	0.0225	1.86E-06	6.70E-04	1.51E-05
23.0	16.8	0.0225	1.93E-06	6.95E-04	1.57E-05
24.0	17.5	0.0226	2.00E-06	7.19E-04	1.62E-05
25.0	18.2	0.0227	2.06E-06	7.42E-04	1.68E-05
26.0	18.9	0.0228	2.12E-06	7.64E-04	1.74E-05
27.0	19.7	0.0229	2.18E-06	7.85E-04	1.80E-05
28.0	20.4	0.0230	2.24E-06	8.05E-04	1.85E-05
29.0	21.0	0.0231	2.29E-06	8.25E-04	1.91E-05
30.0	21.7	0.0233	2.34E-06	8.43E-04	1.96E-05
31.0	22.4	0.0235	2.39E-06	8.60E-04	2.02E-05
32.0	23.1	0.0237	2.43E-06	8.76E-04	2.07E-05
33.0	23.8	0.0239	2.48E-06	8.91E-04	2.13E-05
34.0	24.5	0.0242	2.51E-06	9.05E-04	2.19E-05
35.0	25.1	0.0245	2.55E-06	9.18E-04	2.24E-05
36.0	25.8	0.0248	2.58E-06	9.30E-04	2.30E-05
37.0	26.5	0.0251	2.61E-06	9.40E-04	2.36E-05
38.0	27.1	0.0255	2.64E-06	9.50E-04	2.43E-05
39.0	27.8	0.0260	2.66E-06	9.58E-04	2.49E-05
40.0	28.4	0.0265	2.68E-06	9.65E-04	2.56E-05
41.0	29.1	0.0271	2.70E-06	9.71E-04	2.63E-05
42.0	29.7	0.0277	2.71E-06	9.76E-04	2.70E-05
43.0	30.3	0.0284	2.72E-06	9.80E-04	2.78E-05
44.0	31.0	0.0292	2.73E-06	9.82E-04	2.86E-05
45.0	31.6	0.0300	2.73E-06	9.83E-04	2.95E-05
46.0	32.2	0.0310	2.73E-06	9.83E-04	3.05E-05
47.0	32.8	0.0321	2.73E-06	9.82E-04	3.15E-05
48.0	33.4	0.0332	2.72E-06	9.80E-04	3.26E-05
49.0	34.0	0.0346	2.71E-06	9.76E-04	3.37E-05
50.0	34.6	0.0360	2.70E-06	9.72E-04	3.50E-05
51.0	35.1	0.0376	2.68E-06	9.66E-04	3.63E-05
52.0	35.7	0.0394	2.66E-06	9.58E-04	3.78E-05
53.0	36.3	0.0414	2.64E-06	9.50E-04	3.93E-05
54.0	36.8	0.0436	2.61E-06	9.41E-04	4.10E-05
55.0	37.4	0.0460	2.58E-06	9.30E-04	4.28E-05
56.0	37.9	0.0487	2.55E-06	9.19E-04	4.47E-05

57.0	38.4	0.0517	2.52E-06	9.06E-04	4.68E-05
58.0	38.9	0.0550	2.48E-06	8.92E-04	4.91E-05
59.0	39.4	0.0587	2.44E-06	8.77E-04	5.14E-05
60.0	39.9	0.0627	2.39E-06	8.61E-04	5.40E-05
61.0	40.4	0.0672	2.34E-06	8.44E-04	5.67E-05
62.0	40.9	0.0722	2.29E-06	8.25E-04	5.96E-05
63.0	41.3	0.0778	2.24E-06	8.06E-04	6.27E-05
64.0	41.7	0.0839	2.18E-06	7.86E-04	6.59E-05
65.0	42.2	0.0907	2.13E-06	7.65E-04	6.94E-05
66.0	42.6	0.0982	2.06E-06	7.43E-04	7.30E-05
67.0	43.0	0.107	2.00E-06	7.20E-04	7.67E-05
68.0	43.4	0.116	1.93E-06	6.96E-04	8.07E-05
69.0	43.8	0.126	1.87E-06	6.72E-04	8.47E-05
70.0	44.1	0.138	1.79E-06	6.46E-04	8.89E-05
71.0	44.5	0.150	1.72E-06	6.20E-04	9.31E-05
72.0	44.8	0.164	1.65E-06	5.93E-04	9.74E-05
73.0	45.1	0.180	1.57E-06	5.65E-04	1.02E-04
74.0	45.4	0.197	1.49E-06	5.37E-04	1.06E-04
75.0	45.7	0.217	1.41E-06	5.08E-04	1.10E-04
76.0	46.0	0.238	1.33E-06	4.78E-04	1.14E-04
77.0	46.2	0.262	1.24E-06	4.48E-04	1.17E-04
78.0	46.4	0.289	1.16E-06	4.17E-04	1.20E-04
79.0	46.7	0.319	1.07E-06	3.86E-04	1.23E-04
80.0	46.9	0.352	9.83E-07	3.54E-04	1.24E-04
81.0	47.0	0.389	8.93E-07	3.22E-04	1.25E-04
82.0	47.2	0.430	8.03E-07	2.89E-04	1.24E-04
83.0	47.3	0.476	7.11E-07	2.56E-04	1.22E-04
84.0	47.5	0.528	6.18E-07	2.23E-04	1.17E-04
85.0	47.6	0.585	5.25E-07	1.89E-04	1.11E-04
86.0	47.7	0.650	4.31E-07	1.55E-04	1.01E-04
87.0	47.7	0.722	3.37E-07	1.21E-04	8.76E-05
88.0	47.8	0.802	2.42E-07	8.72E-05	7.00E-05
89.0	47.8	0.893	1.47E-07	5.30E-05	4.73E-05
90.0	47.8	1.00	5.20E-08	1.87E-05	1.86E-05
Sum				0.0564	0.00404
Average fraction of light reflected: 0.00404/0.0564= 0.0717					

B. After the light is transmitted across the spherical droplet, it encounters the liquid-air interface at the superhydrophobic surface (ray **b'** in Fig. III.2A). A fraction of the light is internally reflected back into the droplet (ray **c** in Fig. III.2A) whereas most of the light exits

from the 10 μL 1.40 M acrylamide droplet (R = 0.134 cm) with contact angle of 155° and encounters the superhydrophobic surface (ray **d** in Fig. III.2A).

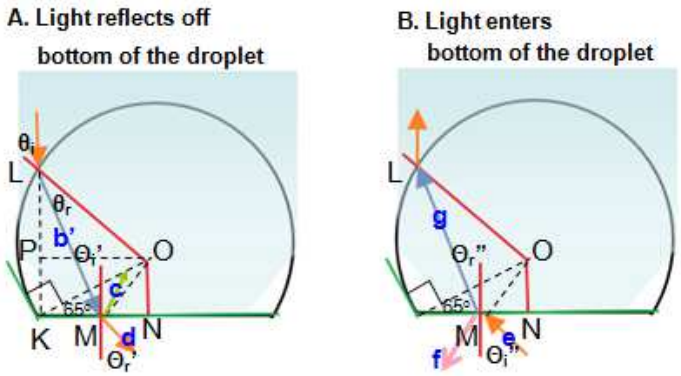

Figure III.2 Schematic of incident angle from a droplet into air for superhydrophobic droplet experiments. (A) Light reflects off bottom of the droplet. (B) Light enters bottom of the droplet.

In Fig. III.2A, the θ_i and θ_r are calculated in Table III.1 above. The incident angle from a droplet into air, θ_i', is (θ_i - θ_r) in Fig. III.2A. The bottom surface of the droplet on a superhydrophobic surface has a complex geometry as it curves around the PDMS posts; to simplify the calculations, the bottom of the droplet will be considered as an average which is nominally flat and parallel to the substrate. The range of incident angles, θ_i', of ray **b'** is between 0 and 42° (Col 1 in Table III.2) and so the range of angles of ray **d** is between 0 and 65° due to refraction (Col 2 in Table III.2). The fraction of reflected light is calculated at a given incident angle (θ_i') using Fresnel equation (in Table III.2 Col 3). The illuminated 2-D area is dependent on the $\angle MON$, calculated using $R\sin(\theta_i) - \tan(\theta_i')(R\cos\theta_i + R\sin(CA - 90^o)) = R\sin(CA - 90^o)\tan(\angle MON)$, where $R\sin\theta_i$ is $\overline{OP}$ (= $\overline{KM}$), CA is contact angle between the droplet and the superhydrophobic surface (155°), $\tan(\theta_i')(R\cos\theta_i + R\sin(CA - 90^o))$ is $\overline{KM}$, and $R\sin(CA - 90^o)\tan(\angle MON)$ is $\overline{MN}$. When $\angle MON$ is 0.0800°, illuminated 2-D projected area is calculated using triangular polygon, ½ × $(R\sin(CA - 90^o)\tan 0.0800^o) \times$

$(1/360 \times 2\pi \times R\sin(CA - 90^o)\tan 0.0800^o)$. The range of $\angle MON$ is between 0.08 and 21°. When $\angle MON$ is more than 0.08°, illuminated 2-D projected area is calculated using trapezoidal polygons, ½ $\times |R\sin(CA - 90^o)\tan x - R\sin(CA - 90^o)\tan y| \times (1/360 \times 2\pi \times R\sin(CA - 90^o)) \times (\tan x + \tan y))$, where x and y represent different $\angle MON$ and follow the sequence in Col 4 in Table III.2. For example, for calculation of projected area at incident angle of 0.260°, *x* and *y* are 0.0800° and 0.558° in the first and second row of Col 4 in Table III.2, respectively. The percent of light reflected (ray **c**) is calculated to be 3.02% of the incidence light (ray **b'**) in Table III.2.

Table III.2 The calculation of light reflected for a 10 μL 1.40 M acrylamide droplet as light exits from the droplet.

Col 1	Col 2	Col 3	Col 4	Col 5	Col 6	Col 7
Incident angle, θ_i	Refraction angle, θ_r	ρ fraction reflected	$\angle MON$	Projected area from one polygon	Total projected area at incident θ_i'	ρ for total projected area at incident θ_i'
degrees	degrees		degrees	cm^2	cm^2	cm^2
0.0245	0.0331	0.0222	0.0800	2.50E-10	9.01E-08	2.00E-09
0.260	0.350	0.0222	0.558	1.19E-08	4.30E-06	9.54E-08
0.519	0.700	0.0222	1.12	3.65E-08	1.32E-05	2.92E-07
0.778	1.05	0.0222	1.67	6.08E-08	2.19E-05	4.86E-07
1.04	1.40	0.0222	2.23	8.50E-08	3.06E-05	6.79E-07
1.29	1.75	0.0222	2.78	1.09E-07	3.92E-05	8.70E-07
1.56	2.11	0.0222	3.33	1.33E-07	4.77E-05	1.06E-06
1.82	2.46	0.0222	3.88	1.56E-07	5.62E-05	1.25E-06
2.08	2.81	0.0222	4.43	1.79E-07	6.45E-05	1.43E-06
2.35	3.17	0.0222	4.97	2.02E-07	7.26E-05	1.61E-06
2.61	3.52	0.0222	5.55	2.24E-07	8.06E-05	1.79E-06
2.87	3.88	0.0222	6.05	2.46E-07	8.84E-05	1.96E-06
3.14	4.24	0.0222	6.58	2.67E-07	9.60E-05	2.13E-06
3.41	4.60	0.0222	7.11	2.87E-07	1.03E-04	2.29E-06
3.68	4.97	0.0222	7.63	3.07E-07	1.11E-04	2.45E-06
3.95	5.33	0.0222	8.14	3.26E-07	1.18E-04	2.61E-06
4.22	5.70	0.0222	8.65	3.45E-07	1.24E-04	2.75E-06
4.49	6.07	0.0222	9.16	3.62E-07	1.30E-04	2.89E-06
4.77	6.44	0.0222	9.65	3.79E-07	1.37E-04	3.03E-06
5.04	6.82	0.0222	10.1	3.95E-07	1.42E-04	3.16E-06

5.32	7.20	0.0222	10.6	4.10E-07	1.48E-04	3.28E-06
5.61	7.58	0.0222	11.1	4.24E-07	1.53E-04	3.39E-06
5.89	7.96	0.0222	11.6	4.37E-07	1.57E-04	3.49E-06
6.18	8.35	0.0222	12.0	4.49E-07	1.62E-04	3.59E-06
6.46	8.74	0.0222	12.5	4.60E-07	1.66E-04	3.67E-06
6.76	9.14	0.0222	12.9	4.70E-07	1.69E-04	3.75E-06
7.05	9.54	0.0222	13.4	4.78E-07	1.72E-04	3.82E-06
7.35	9.94	0.0222	13.8	4.86E-07	1.75E-04	3.88E-06
7.65	10.4	0.0222	14.2	4.92E-07	1.77E-04	3.93E-06
7.95	10.8	0.0222	14.6	4.97E-07	1.79E-04	3.97E-06
8.26	11.2	0.0222	15.0	5.01E-07	1.80E-04	4.00E-06
8.57	11.6	0.0222	15.4	5.03E-07	1.81E-04	4.02E-06
8.89	12.0	0.0222	15.8	5.04E-07	1.82E-04	4.03E-06
9.21	12.5	0.0222	16.1	5.04E-07	1.82E-04	4.03E-06
9.53	12.9	0.0222	16.5	5.03E-07	1.81E-04	4.02E-06
9.86	13.4	0.0222	16.8	5.00E-07	1.80E-04	4.00E-06
10.19	13.8	0.0222	17.1	4.96E-07	1.78E-04	3.97E-06
10.53	14.3	0.0222	17.5	4.90E-07	1.76E-04	3.92E-06
10.87	14.7	0.0222	17.8	4.83E-07	1.74E-04	3.87E-06
11.21	15.2	0.0222	18.1	4.75E-07	1.71E-04	3.80E-06
11.57	15.7	0.0223	18.4	4.65E-07	1.67E-04	3.72E-06
11.92	16.2	0.0223	18.6	4.54E-07	1.63E-04	3.64E-06
12.29	16.7	0.0223	18.9	4.41E-07	1.59E-04	3.54E-06
12.65	17.2	0.0223	19.1	4.27E-07	1.54E-04	3.43E-06
13.03	17.7	0.0223	19.4	4.12E-07	1.48E-04	3.31E-06
13.41	18.2	0.0223	19.6	3.95E-07	1.42E-04	3.17E-06
13.80	18.8	0.0223	19.8	3.77E-07	1.36E-04	3.03E-06
14.20	19.3	0.0223	20.0	3.58E-07	1.29E-04	2.88E-06
14.60	19.9	0.0224	20.2	3.37E-07	1.21E-04	2.72E-06
15.01	20.5	0.0224	20.3	3.15E-07	1.14E-04	2.54E-06
15.43	21.0	0.0224	20.5	2.92E-07	1.05E-04	2.36E-06
15.85	21.6	0.0224	20.6	2.68E-07	9.65E-05	2.17E-06
16.28	22.2	0.0225	20.8	2.43E-07	8.73E-05	1.96E-06
16.73	22.9	0.0225	20.9	2.16E-07	7.78E-05	1.75E-06
17.18	23.5	0.0226	21.0	1.88E-07	6.78E-05	1.53E-06
17.64	24.1	0.0226	21.1	1.60E-07	5.75E-05	1.30E-06
18.11	24.8	0.0227	21.1	1.30E-07	4.68E-05	1.06E-06
18.59	25.5	0.0227	21.2	9.94E-08	3.58E-05	8.13E-07
19.08	26.2	0.0228	21.2	6.80E-08	2.45E-05	5.58E-07
19.58	26.9	0.0229	21.2	3.58E-08	1.29E-05	2.95E-07
20.09	27.6	0.0230	21.2	2.90E-09	1.04E-06	2.40E-08
20.61	28.4	0.0231	21.2	3.06E-08	1.10E-05	2.54E-07
21.15	29.1	0.0232	21.2	6.47E-08	2.33E-05	5.40E-07
21.69	29.9	0.0233	21.1	9.93E-08	3.58E-05	8.33E-07
22.25	30.7	0.0234	21.1	1.34E-07	4.83E-05	1.13E-06

22.82	31.6	0.0236	21.0	1.69E-07	6.10E-05	1.44E-06
23.41	32.4	0.0238	20.9	2.05E-07	7.38E-05	1.75E-06
24.00	33.3	0.0240	20.7	2.40E-07	8.65E-05	2.08E-06
24.61	34.2	0.0242	20.6	2.76E-07	9.93E-05	2.40E-06
25.24	35.1	0.0245	20.4	3.11E-07	1.12E-04	2.74E-06
25.88	36.1	0.0248	20.3	3.46E-07	1.25E-04	3.09E-06
26.53	37.1	0.0252	20.0	3.81E-07	1.37E-04	3.45E-06
27.20	38.1	0.0256	19.8	4.15E-07	1.49E-04	3.82E-06
27.89	39.2	0.0261	19.6	4.48E-07	1.61E-04	4.21E-06
28.59	40.2	0.0266	19.3	4.81E-07	1.73E-04	4.61E-06
29.30	41.4	0.0273	19.0	5.12E-07	1.84E-04	5.03E-06
30.04	42.5	0.0280	18.7	5.43E-07	1.95E-04	5.48E-06
30.79	43.7	0.0289	18.4	5.72E-07	2.06E-04	5.96E-06
31.55	44.9	0.0300	18.0	6.00E-07	2.16E-04	6.47E-06
32.34	46.2	0.0312	17.6	6.26E-07	2.25E-04	7.04E-06
33.14	47.6	0.0327	17.2	6.50E-07	2.34E-04	7.65E-06
33.96	48.9	0.0345	16.7	6.72E-07	2.42E-04	8.34E-06
34.80	50.4	0.0366	16.2	6.92E-07	2.49E-04	9.12E-06
35.66	51.9	0.0392	15.7	7.09E-07	2.55E-04	1.00E-05
36.53	53.5	0.0424	15.2	7.24E-07	2.61E-04	1.10E-05
37.43	55.1	0.0463	14.6	7.35E-07	2.65E-04	1.23E-05
38.34	56.9	0.0513	14.0	7.43E-07	2.68E-04	1.37E-05
39.27	58.7	0.0575	13.3	7.47E-07	2.69E-04	1.55E-05
40.22	60.7	0.0656	12.7	7.47E-07	2.69E-04	1.77E-05
41.19	62.7	0.0763	11.9	7.43E-07	2.67E-04	2.04E-05
42.18	65.0	0.0907	11.2	7.33E-07	2.64E-04	2.39E-05
				Sum	0.0121	0.000367
Average fraction of ray b' that is internally reflected (ray c): 0.000367/0.0121= 0.0302						

C. After the light is reflected from the solid surface, it encounters the liquid-air interface at the superhydrophobic surface (ray **e** in Fig. 4.6A and III.2B). A fraction of the light is reflected off the droplet surface (ray **f** in Fig. 4.6A) whereas most of the light enters the 10 μL 1.40 M acrylamide droplet (R = 0.134 cm) (ray **g** in Fig. 4.6A and III.2B).

Although the superhydrophobic surface is rough, the path of reflected light is regarded as $\overline{LM}$**,** which is original path of ray **b'** (in Fig. III.2B). The range of incident angles, θ_i", of ray **e** is between 0 and 65° (from Col 2 in Table III.2), and so the range of angles, θ_r", of ray **g** is between 0 and 42° (from Col 1 in Table III.2) due to refraction. The range of $\angle MON$ is between

0.08 and 21° (from Col 4 in Table III.2). The fraction of reflected light and illuminated 2-D area are calculated at a given incident angle. The percent of light reflected (ray **f**) is calculated to be 3.02% of the incidence light (ray **e**).

III.2 Percent of Light Reflected from the Surface of a Hydrophobic Droplet

A. Reflectance from a hydrophobic droplet surface. Light enters a 10 μL 1.40 M acrylamide droplet (R = 0.162 cm) on a hydrophobic surface: The process for calculation of the percent of light reflected follows the same procedure as described in section A.III.1.A. The percent of light reflected (ray **a**) is calculated to be 7.17% of the incidence light (Fig. 4.6B).

B. Internal reflection. After the light is transmitted across the droplet, it reflects off the hydrophobic surface interface and traverses the droplet a second time. The ray encounters the liquid-air interface (ray **e'** in Fig. III.3). A fraction of the light is internally reflected back into the droplet (ray **h** in Fig. III.3) whereas most of the light exits from the droplet (ray **i** in Fig. III.3).

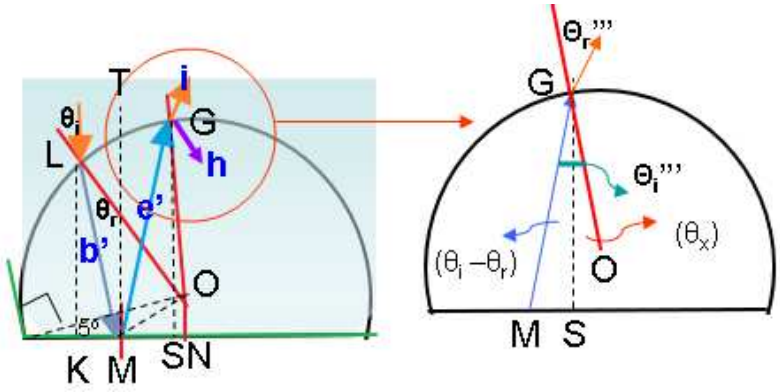

Figure III.3 Schematic of incident angle from a droplet into air for hydrophobic droplet experiments.

The θ_i and θ_r in Fig. III.3 are calculated in Table III.1 above. The incident angle, θ_i''', of ray **e'** is $\angle MGO$ in Fig. III.3. Due to $\overline{LK} // \overline{TM} // \overline{GS}$ and $\angle LMT = \angle TMG$, $\angle MGN$ is sum of $\angle MGS$ $(= \theta_i - \theta_r)$ and $\angle SGO (= \theta_x)$. θ_x is obtained using $\overline{SN} = \overline{KN} - \overline{KM} - \overline{MS}$, where $\overline{SN}$ is

$R\sin\theta_x$, $\overline{KN}$ is $R\sin\theta_i$, $\overline{KM}$ is $R(\cos\theta_i + R\sin(CA-90^o))\tan(\theta_i-\theta_r)$, $\overline{MS}$ is $R\times(\sin\theta_i/\tan((180-\theta_i)/2)/\cos(\theta_i-\theta_r)+(\cos\theta_i+\sin(CA-90^o))/\cos(\theta_i-\theta_r))\times\sin(\theta_i-\theta_r)$ and CA is contact angle between the droplet and the superhydrophobic surface (95°). The range of incident angles, θ_i''', of ray **e'** is between 0 and 39°, and so the range of angles, θ_r''', of ray **i** in Fig. III.3 is between 0 and 58° due to refraction. The illuminated 2-D area is dependent on the $\angle SGO$. When $\angle SGO$ is 0.0400°, illuminated 2-D projected area is calculated using triangular polygon, $1/2\times(R\sin 0.0400^o)\times(1/360\times 2\pi\times R\sin 0.0400^o)$. When $\angle SGO$ is more than 0.0400°, illuminated 2-D projected area is calculated using trapezoidal polygons, $1/2\times R|\sin a-\sin b|\times(1/360\times 2\pi\times R(\sin a+\sin b))$, where a and b represent different $\angle SGO$ and follow the sequence in Col 4 in Table III.3. For example, for calculation of projected area at incident angle of 0.696° in the second row of Col 4 in Table III.3, a and b are 0.0400° and 0.436° in the first row and second row of Col 4 in Table III.3, respectively. The percent of light internally reflected (ray **i**) is calculated to be 3.65% of the incident light (ray **e'**) in Table III.3.

Table III.3 The calculation of light reflected for a 10 μL 1.40 M acrylamide droplet as light exits from the droplet.

Col 1	Col 2	Col 3	Col 4	Col 5	Col 6	Col 7
Incident angle, θ_i	Refraction angle, θ_r	ρ fraction reflected	$\angle SGO$	Projected area from one polygon	Total projected area at incident θ_i'''	ρ for total projected area at incident θ_i'''
degrees	degrees		degrees	cm^2	cm^2	cm^2
0.0696	0.0939	0.0222	0.0400	1.11E-10	4.01E-08	8.90E-10
0.696	0.939	0.0222	0.436	1.31E-08	4.73E-06	1.05E-07
1.39	1.88	0.0222	0.872	3.97E-08	1.43E-05	3.17E-07
2.09	2.82	0.0222	1.31	6.61E-08	2.38E-05	5.28E-07
2.78	3.75	0.0222	1.74	9.23E-08	3.32E-05	7.37E-07
3.47	4.69	0.0222	2.18	1.18E-07	4.25E-05	9.44E-07
4.17	5.63	0.0222	2.61	1.44E-07	5.17E-05	1.15E-06
4.86	6.57	0.0222	3.03	1.69E-07	6.08E-05	1.35E-06
5.54	7.50	0.0222	3.47	1.94E-07	6.97E-05	1.55E-06

6.23	8.43	0.0222	3.89	2.18E-07	7.84E-05	1.74E-06
6.92	9.37	0.0222	4.31	2.41E-07	8.68E-05	1.93E-06
7.61	10.3	0.0222	4.74	2.64E-07	9.50E-05	2.11E-06
8.29	11.2	0.0222	5.15	2.86E-07	1.03E-04	2.28E-06
8.97	12.2	0.0222	5.57	3.07E-07	1.11E-04	2.45E-06
9.65	13.1	0.0222	5.98	3.27E-07	1.18E-04	2.62E-06
10.3	14.0	0.0222	6.38	3.46E-07	1.25E-04	2.77E-06
11.0	14.9	0.0222	6.78	3.65E-07	1.31E-04	2.92E-06
11.7	15.8	0.0223	7.18	3.82E-07	1.37E-04	3.06E-06
12.3	16.8	0.0223	7.57	3.98E-07	1.43E-04	3.19E-06
13.0	17.7	0.0223	7.96	4.13E-07	1.49E-04	3.31E-06
13.7	18.6	0.0223	8.34	4.26E-07	1.53E-04	3.42E-06
14.3	19.5	0.0224	8.71	4.38E-07	1.58E-04	3.53E-06
15.0	20.4	0.0224	9.08	4.49E-07	1.62E-04	3.62E-06
15.6	21.3	0.0224	9.44	4.58E-07	1.65E-04	3.70E-06
16.3	22.2	0.0225	9.80	4.66E-07	1.68E-04	3.77E-06
16.9	23.1	0.0225	10.1	4.72E-07	1.70E-04	3.83E-06
17.5	24.0	0.0226	10.5	4.77E-07	1.72E-04	3.88E-06
18.2	24.9	0.0227	10.8	4.80E-07	1.73E-04	3.92E-06
18.8	25.8	0.0228	11.1	4.82E-07	1.73E-04	3.94E-06
19.4	26.6	0.0228	11.4	4.81E-07	1.73E-04	3.96E-06
20.0	27.5	0.0229	11.8	4.80E-07	1.73E-04	3.96E-06
20.6	28.4	0.0231	12.1	4.76E-07	1.71E-04	3.95E-06
21.2	29.3	0.0232	12.3	4.71E-07	1.69E-04	3.93E-06
21.8	30.1	0.0233	12.6	4.64E-07	1.67E-04	3.89E-06
22.4	31.0	0.0235	12.9	4.55E-07	1.64E-04	3.84E-06
23.0	31.8	0.0236	13.1	4.44E-07	1.60E-04	3.78E-06
23.6	32.7	0.0238	13.4	4.32E-07	1.55E-04	3.70E-06
24.1	33.5	0.0240	13.6	4.17E-07	1.50E-04	3.61E-06
24.7	34.3	0.0243	13.8	4.01E-07	1.44E-04	3.50E-06
25.2	35.1	0.0245	14.0	3.84E-07	1.38E-04	3.38E-06
25.8	36.0	0.0248	14.2	3.64E-07	1.31E-04	3.25E-06
26.3	36.8	0.0251	14.4	3.43E-07	1.23E-04	3.09E-06
26.8	37.6	0.0254	14.6	3.20E-07	1.15E-04	2.92E-06
27.4	38.4	0.0257	14.7	2.95E-07	1.06E-04	2.73E-06
27.9	39.1	0.0261	14.9	2.69E-07	9.68E-05	2.52E-06
28.4	39.9	0.0265	15.0	2.41E-07	8.68E-05	2.30E-06
28.9	40.7	0.0269	15.1	2.12E-07	7.62E-05	2.05E-06
29.4	41.4	0.0273	15.2	1.81E-07	6.50E-05	1.78E-06
29.8	42.2	0.0278	15.2	1.48E-07	5.34E-05	1.49E-06
30.3	42.9	0.0283	15.3	1.15E-07	4.13E-05	1.17E-06
30.8	43.7	0.0289	15.3	7.98E-08	2.87E-05	8.30E-07
31.2	44.4	0.0295	15.4	4.37E-08	1.57E-05	4.64E-07
31.6	45.1	0.0301	15.4	6.57E-09	2.36E-06	7.12E-08
32.1	45.8	0.0308	15.3	3.15E-08	1.14E-05	3.50E-07

32.5	46.5	0.0315	15.3	7.05E-08	2.54E-05	7.99E-07
32.9	47.2	0.0322	15.3	1.10E-07	3.97E-05	1.28E-06
33.3	47.8	0.0330	15.2	1.50E-07	5.41E-05	1.79E-06
33.7	48.5	0.0338	15.1	1.91E-07	6.88E-05	2.33E-06
34.1	49.1	0.0347	15.0	2.32E-07	8.35E-05	2.90E-06
34.4	49.7	0.0356	14.8	2.73E-07	9.82E-05	3.50E-06
34.8	50.3	0.0365	14.7	3.14E-07	1.13E-04	4.13E-06
35.1	50.9	0.0375	14.5	3.54E-07	1.28E-04	4.78E-06
35.4	51.5	0.0385	14.3	3.94E-07	1.42E-04	5.47E-06
35.8	52.1	0.0395	14.1	4.34E-07	1.56E-04	6.17E-06
36.1	52.6	0.0406	13.8	4.72E-07	1.70E-04	6.90E-06
36.4	53.1	0.0417	13.5	5.09E-07	1.83E-04	7.63E-06
36.6	53.7	0.0428	13.2	5.44E-07	1.96E-04	8.38E-06
36.9	54.1	0.0439	12.9	5.77E-07	2.08E-04	9.13E-06
37.2	54.6	0.0451	12.5	6.09E-07	2.19E-04	9.87E-06
37.4	55.1	0.0462	12.2	6.37E-07	2.29E-04	1.06E-05
37.6	55.5	0.0473	11.8	6.63E-07	2.39E-04	1.13E-05
37.8	55.9	0.0485	11.3	6.85E-07	2.46E-04	1.19E-05
38.0	56.3	0.0496	10.8	7.03E-07	2.53E-04	1.25E-05
38.2	56.7	0.0507	10.4	7.17E-07	2.58E-04	1.31E-05
38.4	57.0	0.0517	9.82	7.26E-07	2.61E-04	1.35E-05
38.6	57.3	0.0527	9.26	7.29E-07	2.62E-04	1.38E-05
38.7	57.6	0.0536	8.67	7.26E-07	2.61E-04	1.40E-05
38.8	57.8	0.0544	8.05	7.17E-07	2.58E-04	1.40E-05
38.9	58.0	0.0552	7.39	7.00E-07	2.52E-04	1.39E-05
39.0	58.2	0.0558	6.70	6.74E-07	2.43E-04	1.35E-05
39.1	58.4	0.0563	5.97	6.39E-07	2.30E-04	1.30E-05
39.2	58.5	0.0567	5.20	5.94E-07	2.14E-04	1.21E-05
39.2	58.5	0.0569	4.39	5.37E-07	1.93E-04	1.10E-05
39.2	58.5	0.0570	3.54	4.68E-07	1.68E-04	9.59E-06
39.2	58.5	0.0568	2.65	3.84E-07	1.38E-04	7.86E-06
39.1	58.4	0.0565	1.71	2.84E-07	1.02E-04	5.79E-06
39.1	58.3	0.0560	0.724	1.67E-07	6.01E-05	3.37E-06
39.0	58.1	0.0553	0.311	2.98E-08	1.07E-05	5.93E-07
38.8	57.8	0.0543	1.40	1.30E-07	4.67E-05	2.54E-06
38.6	57.5	0.0532	2.55	3.14E-07	1.13E-04	6.02E-06
38.4	57.0	0.0518	3.75	5.28E-07	1.90E-04	9.84E-06
				Sum:	0.0119	0.000434
Average fraction of ray e' internally reflected (ray h): 0.000434/0.0119= 0.0365						

III.3 Path Length of Light for a Superhydrophobic and a Hydrophobic Droplet

Since UV light uniformly illuminates the droplet from above, the light rays can be assumed to be parallel (perpendicular to the substrate) with a range of incident angles on the curved droplet surface ranging between 0 and 90°. For a given polygon, the path length of light ($\overline{LM}$ in Fig. III.4) is calculated at a given incident angle (θ_i) using $(R\cos\theta_i + R\sin(CA - 90^o)) \times \tan(\theta_i - \theta_r)$, where CA is the contact angle. The incident light at θ_i is determined from the projected area at θ_i (Table III.1 Col 8) and multiplying by 360 to determine the total projected area at θ_i (Table III.1 Col 9). The total path length at θ_i is calculated by multiplying path length of light at θ_i by Col 9 in Table III.1. The average path length from the droplet is then the sum of total path lengths at θ_i divided by the sum of total projected areas at θ_i. The average path length in a superhydrophobic droplet is calculated to be 1.63R. The average path length in a hydrophobic droplet is calculated to be 0.77R. These values are in good agreement with the calculation reported by Horowitz.[21]

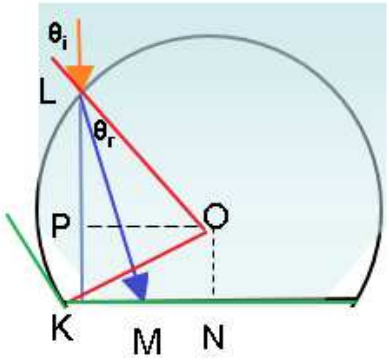

Figure III.4 Schematic of calculation of path length.

Appendix IV. Calculation of Reflected and Refracted UV Light Percent and Path Length for Reactants in a Vial

The effect of the curved surface of the reaction vial must be considered to accurately account for the amount of UV light that interacts with the sample. To calculate the fraction of light entering the reactants, the percent of light reflected and absorbed by the glass wall must be calculated. The reflectance, ρ, is as a function of the incidence angle and refraction angle.[154]

$$\rho = \frac{1}{2}\left[\frac{\sin^2(\theta_i - \theta_r)}{\sin^2(\theta_i + \theta_r)} + \frac{\tan^2(\theta_i - \theta_r)}{\tan^2(\theta_i + \theta_r)}\right] \tag{4.6}$$

where θ_i is the incident angle and θ_r is the refraction angle which is calculated using Snell's law, $\sin\theta_i / \sin\theta_r = n_2 / n_1$, where n is the refractive index of the medium.

Assuming the incident light is normal to the cylindrical axis of the vial and since the wall of the vial is curved, the incident angle will vary across the vial. To calculate the reflectance, the first step is to divide the surface into slices each of which are further divided into 180 rectangular polygons, 1^o in width (Fig. IV.1A).

To calculate the percent of incident light falling on a polygon, a projection of the light onto the 2-D plane is first calculated. For a rectangular polygon in the central circle (Fig. IV.1.B), the incident surface is defined by the curved surface QVWX and the projected area is QYZX. The segment $\overline{EO}$ is radius (R), $\overline{GH}$ and $\overline{EK}$ would be $R\sin(\theta_i)$ and $R\sin(\theta_{i+1})$, respectively. The area of the rectangle QYZX is $\overline{YZ} \times \overline{EJ}$, where $\overline{YZ}$ ($=\overline{QX}=\overline{VW}$) is defined as 0.00280 cm, and $\overline{EJ}$ is equal to $(R\sin(\theta_{i+1}) - R\sin(\theta_i))$.

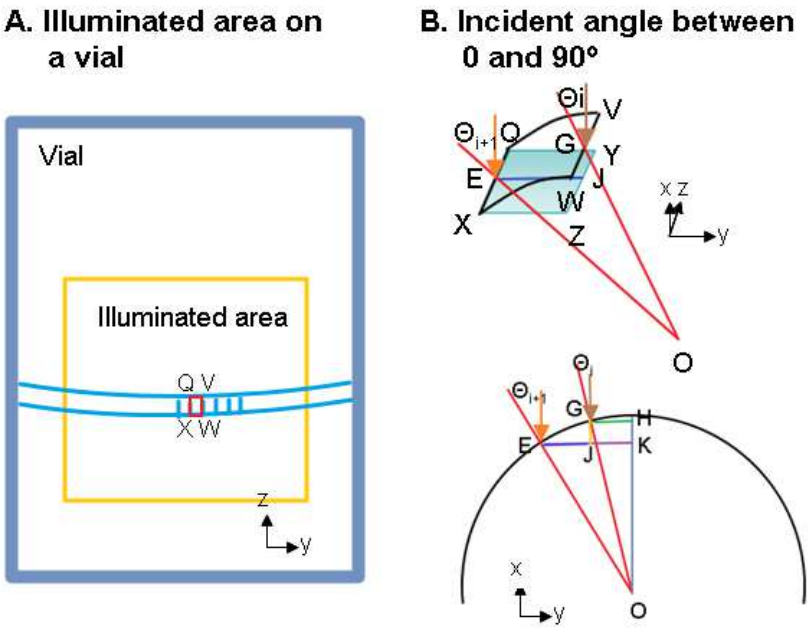

Figure IV.1 Schematic of (A) illuminated area of the vial in the UV-Vis spectrometer (B) 2-D projected area at incident angles between 0° and 90°.

IV.1 Percent of Light Absorbed by Glass

The percent transmission through an empty glass vial at a wavelength of 300 nm was characterized by UV-Vis spectrometry to be 49.9%. This relatively low percent transmission is due to reflections off the curved surface of the vial, absorption by the glass, and refractive indices of the media. In order to obtain the percentage of light absorbed by the glass, the percent reflected from the two walls of the vial first is calculated.

Percent reflected at the exterior air/glass interface (convex). In the spectrometer, the vial is illuminated over a 0.470 cm^2 area with height of 0.689 cm and width of 0.682 cm (Fig. IV.1A). Because $\overline{MN}$ is 0.341 cm (= 0.682 cm/2), $\overline{AO}$ is 0.577 cm, and $\overline{BO}$ is 0.500 cm in Fig. IV.2, the largest incident angle is 36.2°. Due to the refractive indices of glass (1.5) and air (1.0), the range of the refraction angles (θ_r) is between 0 and 23.2°. The illuminated area of the vial is divided into 9350 rectangular polygons with the height of 0.00280 cm and the width of 1°. For

each polygon, the fraction of reflected light and the 2-D projection of the area need be determined. The incident angles and refraction angles are used as inputs to the Fresnel equation to calculate the fraction of reflected light at each polygon. The height of 0.00280 cm and width, which is dependent on the incident angle, θ_i, from air to glass (parallel to the X axis) is used to calculate the 2-D projected area. The total fraction of reflected light at θ_i is calculated by multiplying fraction of reflected light at θ_i by the 2-D projected area at θ_i (Col 2 in Table IV.1). The average fraction of reflected light is then the sum of total fraction of reflected light at θ_i divided by the sum of total projected areas at θ_i. The results in Table IV.1 indicate the convex air/glass interface reflects 4.06% of light in the UV-Vis spectrometer.

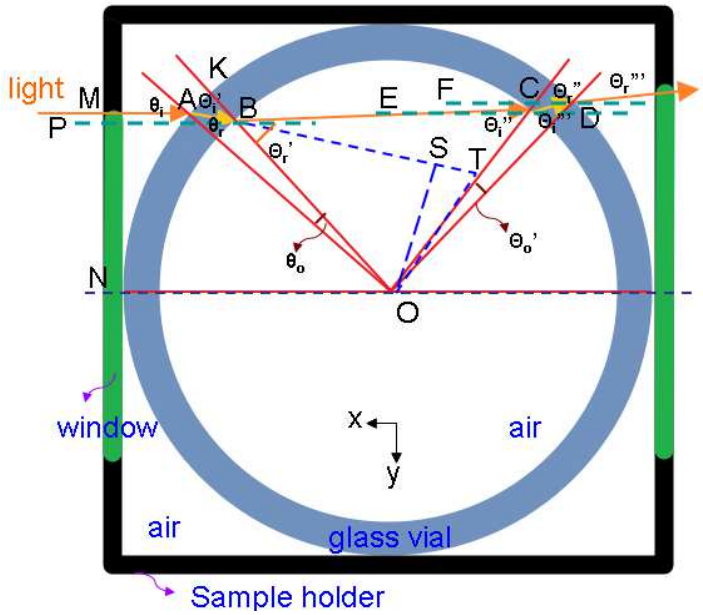

Figure IV.2 Schematic of light path for the empty glass vial in the UV-Vis spectrometer as seen looking down onto the vial.

Percent reflected at the interior glass/air interface (convex). Due to refraction and transmission of light, the incident angle, θ_i', is calculated to be ($\theta_r + \theta_o$) and the range is between 0 and 27.0°. To determine θ_i', two right triangles, △ATO, and △ASO can be defined where

$\angle AOT$ is 90°, and $\angle OSA$ is 90°. The result is shown in Col 4. The refraction angle, θ_r', is obtained using refractive indices of the glass/air, θ_i' and Snell's law. The fraction of reflected light for each polygon is calculated using the Fresnel equation. The angle, $\angle PBK$, where $\overline{PB}$ is parallel to the X axis, is calculated to be $(\theta_i + \theta_o)$ for the further calculation of the 2-D projected area of illumination. The calculation for the 2-D projected area (Col 5) and the average fraction of reflected light (Col 6) follow the same procedure as described in the above section and the results are shown in Table IV.1. The convex glass/air interface reflects 4.13% of light in UV-Vis spectrometry.

Percent reflected at the inner air/glass interface (concave). Due to transmission of light in cylindrical vial ($\overline{BO}$ is equal to $\overline{CO}$), the incident angle, θ_i'' (Col 7), is equal to the refraction angle, θ_r'. The refraction angle, θ_r'', is obtained using refractive indices of the air/glass, θ_i'' and Snell's law. The angle from air to glass, $\angle OCE$, where $\overline{CE}$ is parallel to the X axis, is calculated to be $(2\theta_i'' - \theta_i - \theta_o)$. The calculation for the fraction of reflected light for each polygon at the same θ_i'' (Col 9), the 2-D projected area (Col 8), and the average fraction of reflected light follow the same procedure as described in above section and the results are shown in Table IV.1. The concave air/glass interface reflects 4.14% of light in UV-Vis spectrometry.

Percent reflected at the exterior glass/air interface (concave). Due of transmission of light in glass, the incident angle, θ_i''' (Col 10), is calculated using the same procedure as described in the calculation of θ_i'. The refraction angle, θ_r''', is obtained using refractive indices of glass/air and Snell's law. The incident angle from glass to air, $\angle ODF$, where $\overline{DF}$ is parallel to the X axis, is $(2\theta_i'' - \theta_i - \theta_o - \theta_o')$. The fraction of reflected light at each polygon with the same incident angle (Col 12), the 2-D projected area (Col 11), and the average fraction of reflected light are

calculated following the same procedure as described in above section and shown in Table IV.1. The concave glass/air interface reflects 4.07% of light in UV-Vis spectrometry.

Hence, the percent of light transmission for light across two walls of the vial is obtained to be 84.6% of incident light. Since measurements show that only 49.9% of the light is transmitted, then each glass wall of the vial absorbs 23.2% of the incident light at 300 nm.

Table IV.1 The calculation of transmission for light across two walls of the vial.

Col 1	Col 2	Col 3	Col 4	Col 5	Col 6	Col 7	Col 8	Col 9	Col 10	Col 11	Col 12
Incident angle, θ_i	Total projected area at incident $\theta_i \times 10^2$	ρ for total projected area at incident $\theta_i \times 10^4$	Incident angle, θ_i'	Total projected area at incident $\theta_i' \times 10^2$	ρ for total projected area at incident $\theta_i' \times 10^4$	Incident angle, θ_i''	Total projected area at incident $\theta_i'' \times 10^2$	ρ for total projected area at incident $\theta_i'' \times 10^4$	Incident angle, θ_i'''	Total projected area at incident $\theta_i''' \times 10^2$	ρ for total projected area at incident $\theta_i''' \times 10^4$
de-grees	cm^2	cm^2	de-grees	cm^2	cm^2	de-grees	cm^2	cm^2	de-grees	cm^2	cm^2
0.100	0.139	0.555	0.031	0.0777	0.311	0.047	0.0351	0.141	0.027	0.0348	0.139
1.00	1.25	4.99	0.724	1.19	4.77	1.09	1.30	5.22	0.627	1.38	5.51
2.00	1.39	5.55	1.49	1.32	5.30	2.24	1.45	5.79	1.29	1.53	6.12
3.00	1.39	5.54	2.26	1.32	5.30	3.39	1.45	5.79	1.94	1.53	6.11
4.00	1.38	5.54	3.03	1.32	5.29	4.55	1.45	5.79	2.63	1.53	6.11
5.00	1.38	5.53	3.80	1.32	5.28	5.70	1.44	5.78	3.29	1.53	6.11
6.00	1.38	5.52	4.57	1.32	5.27	6.86	1.44	5.77	3.96	1.53	6.10
7.00	1.38	5.51	5.33	1.32	5.26	8.02	1.44	5.76	4.62	1.52	6.09
8.00	1.38	5.50	6.10	1.31	5.25	9.17	1.44	5.75	5.28	1.52	6.09
9.00	1.37	5.49	6.87	1.31	5.24	10.3	1.44	5.74	5.95	1.52	6.08
10.0	1.37	5.47	7.63	1.30	5.22	11.5	1.43	5.73	6.61	1.52	6.07
11.0	1.36	5.46	8.40	1.30	5.20	12.7	1.43	5.72	7.27	1.51	6.06
12.0	1.36	5.44	9.16	1.29	5.19	13.8	1.42	5.70	7.93	1.51	6.05
13.0	1.35	5.42	9.92	1.29	5.17	15.0	1.42	5.69	8.59	1.51	6.04
14.0	1.35	5.40	10.7	1.28	5.15	16.1	1.41	5.67	9.24	1.50	6.02
15.0	1.34	5.38	11.4	1.28	5.12	17.3	1.41	5.66	9.90	1.50	6.01
16.0	1.34	5.36	12.2	1.27	5.10	18.5	1.40	5.64	10.5	1.50	6.00
17.0	1.33	5.34	13.0	1.26	5.08	19.6	1.40	5.62	11.2	1.49	5.98
18.0	1.32	5.31	13.7	1.25	5.06	20.8	1.39	5.61	11.8	1.49	5.97
19.0	1.32	5.29	14.5	1.25	5.03	22.0	1.38	5.59	12.5	1.48	5.96

20.0	1.31	5.26	15.2	1.24	5.01	23.2	1.38	5.58	13.1	1.48	5.94
21.0	1.30	5.24	16.0	1.23	4.99	24.4	1.37	5.56	13.8	1.47	5.93
22.0	1.29	5.21	16.7	1.22	4.96	25.5	1.36	5.55	14.4	1.47	5.92
23.0	1.28	5.19	17.4	1.21	4.94	26.7	1.35	5.54	15.1	1.46	5.91
24.0	1.27	5.16	18.2	1.20	4.92	27.9	1.34	5.53	15.7	1.45	5.90
25.0	1.26	5.14	18.9	1.19	4.90	29.1	1.34	5.52	16.3	1.45	5.89
26.0	1.25	5.11	19.7	1.17	4.88	30.3	1.33	5.52	17.0	1.44	5.88
27.0	1.24	5.08	20.4	1.16	4.87	31.5	1.32	5.52	17.6	1.43	5.87
28.0	1.23	5.06	21.1	1.15	4.86	32.7	1.31	5.52	18.2	1.43	5.87
29.0	1.22	5.04	21.9	1.14	4.85	33.9	1.30	5.53	18.8	1.42	5.87
30.0	1.21	5.01	22.6	1.12	4.85	35.2	1.28	5.54	19.4	1.41	5.87
31.0	1.20	4.99	23.3	1.11	4.85	36.4	1.27	5.56	20.0	1.41	5.87
32.0	1.18	4.97	24.0	1.10	4.85	37.6	1.26	5.59	20.7	1.40	5.88
33.0	1.17	4.95	24.7	1.08	4.86	38.9	1.25	5.62	21.3	1.39	5.89
34.0	1.16	4.94	25.4	1.07	4.88	40.1	1.24	5.66	21.9	1.38	5.90
35.0	1.14	4.92	26.1	1.05	4.91	41.4	1.22	5.72	22.4	1.38	5.92
36.0	1.13	4.91	26.8	1.04	4.95	42.6	1.21	5.78	23.0	1.37	5.94
36.2	0.269	1.17	27.0	0.246	1.18	42.9	0.288	1.39	23.2	0.327	1.42
Average reflection (air to convex glass): Sum(Col 3)/Sum(Col 2) =4.06%			Average reflection (convex glass to air): Sum(Col 6)/Sum(Col 5) =4.13%			Average reflection (air to concave glass): Sum(Col 9)/Sum(Col 8) =4.14%			Average reflection (concave glass to air): Sum(Col 12)/Sum(Col 11) =4.07%		
Transmission 95.9%			Transmission 95.9%			Transmission 95.9%			Transmission 95.9%		

IV.2 Percent of Light Transmission for the Vial Polymerization Experiment

In this experiment the vial is illuminated by UV light emitted from the end of a 0.3 cm diameter lightguide held 1.0 cm away. The light illuminates a circular region on the vial 1.0 cm in diameter. The percent transmission is influenced by the curved surface of the glass vial, absorption by the glass, and the refractive indices of the media. The absorption by the glass was determined in the previous section to be 23.2%. In the vial experiments, the media include air, glass and 1.40 M acrylamide solution. The light path in the vial is illustrated using Fig. IV.3. The calculation of fraction of light reflected is described below.

Percent reflected at the exterior air/glass interface (convex). In Fig. IV.3A, the vial is illuminated over a 0.79 cm^2 area with radius of 0.50 cm. Because $\overline{MN}$ is 0.25 cm (= 0.50 cm/2),

$\overline{AO}$ is 0.577 cm, and $\overline{QO}$ is 0.500 cm, the largest incident angle is 60° (Col 1). Due to the refractive indices of glass (1.5) and air (1.0), the range of refraction angles is between 0 and 35°. The illuminated area in vial is divided into 32155 rectangular polygons with the height of 0.00280 cm and the width of 1°. The height, H, of illuminated area on the wall of the vial at θ_i is $2\times\sqrt{(0.50cm)^2-(0.577cm\times\sin(\theta_i))^2}$, where 0.50 cm is the radius of illuminated area and 0.577 cm is the outside radius of the glass vial. The number of 2-D projected polygons at θ_i is H (cm)/0.00280 (cm). The fraction of reflected light for each polygon is calculated using the Fresnel equation. The angle, θ_i, from air to glass (parallel to the X axis) is used to calculate the 2-D projected illuminated area; the sum of the projected areas at the same θ_i is shown in Col 2. The calculation for the average fraction of reflected light follows the same procedure as described in the above sections and the results are shown in Col 3 of Table IV.2. The convex air/glass interface reflects 4.31% of light.

Percent reflected at the interior glass/1.40 M acrylamide interface (convex). Due to refraction and transmission of light in glass, the incident angle, θ_i', is calculated to be ($\theta_r + \theta_o$) and the range is between 0 and 67° (Col 4) using the same procedure described in section A.IV.1. The refraction angle, θ_r', is obtained using refractive indices of the glass/1.40 M acrylamide (1.5/1.35), θ_i' and Snell's law. The fraction of reflected light for each polygon is calculated using the Fresnel equation. The angle, $\angle PBK$, where $\overline{PB}$ is parallel to the X axis, is calculated to be ($\theta_i + \theta_o$) for the further calculation of the 2-D projected illuminated area at the same θ_i (Col 5). The height, H', of illuminated area on the acrylamide at ($\theta_i + \theta_o$) is $2\times\sqrt{(0.50cm)^2-(0.500cm\times\sin(\theta_i+\theta_0))^2}$, where 0.50 cm is the radius of the illuminated area and 0.500 cm is the inside radius of the vial. The number of 2-D projected polygons at ($\theta_i + \theta_o$) is

H’ (cm)/0.00280 (cm). The calculation for the 2-D projected area (Col 5) and the average fraction of reflected light (Col 6) follow the same procedure as described above. The results indicate the convex glass/1.40 M acrylamide interface reflects 0.300% of light.

Hence, because the convex air/glass interface reflects 4.31% of light, the convex glass/1.40 M acrylamide interface reflects 0.300% of light, and each glass wall of the vial absorbs 23.2% of the incident light at 300 nm, the percent of light transmission for light across one wall of the vial with 1.40 M acrylamide is calculated to be 74.0% of incident light.

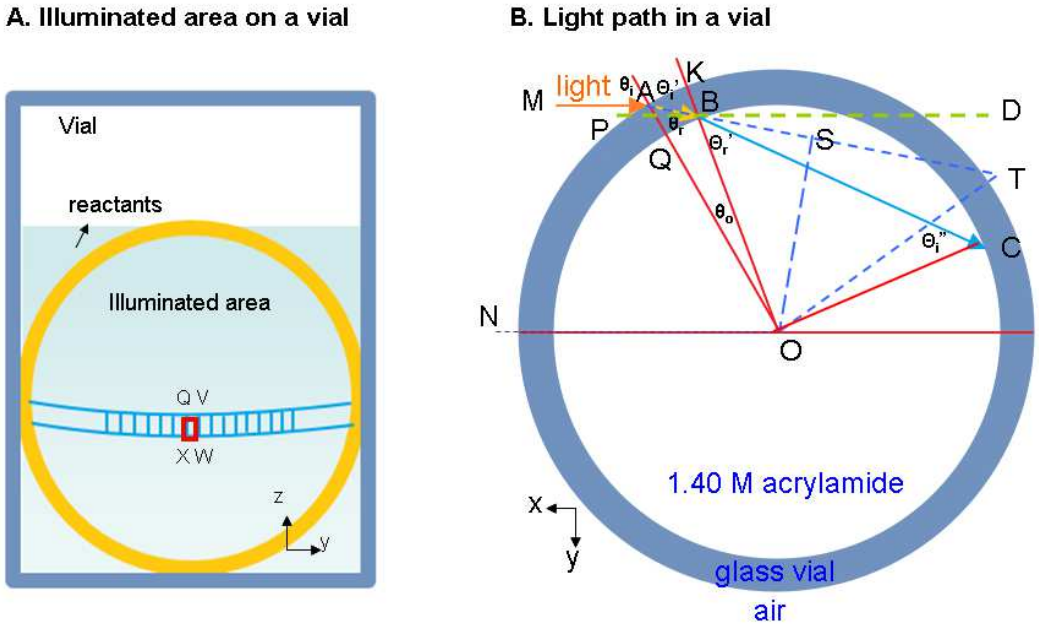

Figure IV.3 Schematic of (A) illuminated area for vial experiments and (B) light path for 1.40 M acrylamide in the glass vial.

Table IV.2 The calculation of transmission for light across one wall of the vial with 1.40 M acrylamide.

Col 1	Col 2	Col 3	Col 4	Col 5	Col 6
Incident angle, θ_i	Total projected area at incident θ_i	ρ for total projected area at incident θ_i	Incident angle, θ_i’	Total projected area at incident θ_i’	ρ for total projected area at incident θ_i’
degrees	cm^2	cm^2	degrees	cm^2	cm^2
0.100	2.01E-03	8.05E-05	0.031	1.13E-03	3.12E-06
1.00	1.81E-02	7.25E-04	0.724	1.73E-02	4.79E-05

2.00	2.01E-02	8.04E-04	1.49	1.92E-02	5.32E-05
3.00	2.01E-02	8.03E-04	2.26	1.92E-02	5.31E-05
4.00	2.00E-02	8.01E-04	3.03	1.91E-02	5.30E-05
5.00	2.00E-02	7.99E-04	3.80	1.91E-02	5.29E-05
6.00	1.99E-02	7.96E-04	4.57	1.90E-02	5.27E-05
7.00	1.98E-02	7.92E-04	5.33	1.89E-02	5.24E-05
8.00	1.97E-02	7.88E-04	6.10	1.88E-02	5.21E-05
9.00	1.96E-02	7.84E-04	6.87	1.87E-02	5.18E-05
10.0	1.95E-02	7.78E-04	7.63	1.86E-02	5.15E-05
11.0	1.93E-02	7.73E-04	8.40	1.84E-02	5.11E-05
12.0	1.92E-02	7.67E-04	9.16	1.83E-02	5.07E-05
13.0	1.90E-02	7.60E-04	9.92	1.81E-02	5.03E-05
14.0	1.88E-02	7.53E-04	10.7	1.80E-02	4.98E-05
15.0	1.86E-02	7.46E-04	11.4	1.78E-02	4.93E-05
16.0	1.84E-02	7.38E-04	12.2	1.76E-02	4.88E-05
17.0	1.82E-02	7.29E-04	13.0	1.73E-02	4.82E-05
18.0	1.79E-02	7.21E-04	13.7	1.71E-02	4.76E-05
19.0	1.77E-02	7.12E-04	14.5	1.69E-02	4.70E-05
20.0	1.74E-02	7.02E-04	15.2	1.66E-02	4.64E-05
21.0	1.72E-02	6.92E-04	16.0	1.64E-02	4.58E-05
22.0	1.69E-02	6.82E-04	16.7	1.61E-02	4.51E-05
23.0	1.66E-02	6.72E-04	17.4	1.58E-02	4.44E-05
24.0	1.63E-02	6.62E-04	18.2	1.56E-02	4.37E-05
25.0	1.60E-02	6.51E-04	18.9	1.53E-02	4.30E-05
26.0	1.57E-02	6.40E-04	19.7	1.50E-02	4.23E-05
27.0	1.53E-02	6.29E-04	20.4	1.46E-02	4.16E-05
28.0	1.50E-02	6.17E-04	21.1	1.43E-02	4.08E-05
29.0	1.47E-02	6.06E-04	21.9	1.40E-02	4.01E-05
30.0	1.43E-02	5.94E-04	22.6	1.37E-02	3.93E-05
31.0	1.40E-02	5.83E-04	23.3	1.33E-02	3.85E-05
32.0	1.36E-02	5.71E-04	24.0	1.30E-02	3.78E-05
33.0	1.32E-02	5.59E-04	24.7	1.26E-02	3.70E-05
34.0	1.28E-02	5.47E-04	25.4	1.23E-02	3.63E-05
35.0	1.24E-02	5.36E-04	26.1	1.19E-02	3.55E-05
36.0	1.20E-02	5.24E-04	26.8	1.16E-02	3.47E-05
37.0	1.17E-02	5.12E-04	27.5	1.12E-02	3.40E-05
38.0	1.12E-02	5.00E-04	28.2	1.08E-02	3.32E-05
39.0	1.08E-02	4.88E-04	28.9	1.04E-02	3.25E-05
40.0	1.04E-02	4.77E-04	29.6	1.01E-02	3.17E-05
41.0	1.00E-02	4.65E-04	30.3	9.70E-03	3.10E-05
42.0	9.59E-03	4.53E-04	30.9	9.32E-03	3.03E-05
43.0	9.17E-03	4.41E-04	31.6	8.95E-03	2.96E-05
44.0	8.74E-03	4.29E-04	32.3	8.57E-03	2.88E-05
45.0	8.31E-03	4.17E-04	32.9	8.20E-03	2.81E-05
46.0	7.88E-03	4.05E-04	33.6	7.83E-03	2.74E-05

47.0	7.44E-03	3.93E-04	34.2	7.46E-03	2.67E-05
48.0	7.01E-03	3.80E-04	34.8	7.10E-03	2.60E-05
49.0	6.57E-03	3.67E-04	35.5	6.73E-03	2.53E-05
50.0	6.12E-03	3.53E-04	36.1	6.38E-03	2.46E-05
51.0	5.68E-03	3.38E-04	36.7	6.02E-03	2.39E-05
52.0	5.23E-03	3.23E-04	37.3	5.68E-03	2.32E-05
53.0	4.77E-03	3.06E-04	37.9	5.33E-03	2.25E-05
54.0	4.30E-03	2.87E-04	38.4	5.00E-03	2.17E-05
55.0	3.83E-03	2.66E-04	39.0	4.67E-03	2.10E-05
56.0	3.33E-03	2.43E-04	39.6	4.35E-03	2.02E-05
57.0	2.81E-03	2.15E-04	40.1	4.04E-03	1.95E-05
58.0	2.24E-03	1.80E-04	40.7	3.74E-03	1.87E-05
59.0	1.57E-03	1.32E-04	41.2	3.44E-03	1.79E-05
60.0	4.37E-04	3.89E-05	41.7	3.16E-03	1.70E-05
Average reflection (air to glass): Sum(Col 3)/Sum(Col 2) =4.31%			Average reflection (glass to solution): Sum(Col 6)/Sum(Col 5)=0.300%		
Transmission 96.7%			Transmission 99.7%		

IV.3 Average Path Length of Light in the Glass Vial Filled with 1.40 M Acrylamide Solution

For a given polygon at the interior glass/1.40 M acrylamide interface, the path length of light, $\overline{BC}$ in Fig. IV.3, at incident angle $\angle KBP$ is calculated using the equation, $(2 \times 0.500cm \times \cos\theta_i')$, where 0.500 cm is the inside radius of the vial and θ_i' is the incident angle form glass to solution ($\theta_i' = \angle KBA$). The 2-D projected area is shown in Col 5 of Table IV.2. The total path length at $\angle KBP$ is calculated by multiplying path length of light at $\angle KBP$ by Col 5. The average path length is then the sum of total path lengths at $\angle KBP$ divided by the sum of total projected areas at $\angle KBP$. The average path length in a vial is calculated to be 1.83R.

Bibliography

(1) G. Odian, *Principles of Polymerization*, 4th ed., Wiley Interscience, Hoboken, New Jersey, **2004**, 204-292.

(2) K. Matyjaszewski, T. P. Davis, *Handbook of Radical Polymerization*, Wiley Interscience, Hoboken, **2002**, 187-252.

(3) M. D. Goodner, C. N. Bowman, *Chemical Engineering Science*, **2002**, *57*, 887-900.

(4) N. S. Allen, *Photopolymerization and Photoimaging Science and Technology*, Elsevier, **1989**.

(5) N. J. Turro, *Macromolecular Photochemistry*, Benjamin-Cummings, **1978**.

(6) L. Zhang, Z. Zeng, Y. Chen, C. Wu, J. Gao, *J. Applied Polym. Sci.*, **1997**, *66*, 2543-2549.

(7) J. P. Fouassier, P. Jacques, D. J. Lougnot, T. Pilot, *Polym. Photochem.*, **1984**, *5*, 57-76.

(8) J. Eichler, C. P. Herz, I. Naito, W. Schnabel, *J. Photochem.*, **1980**, *12*, 225-234.

(9) J. Groenenboom, H. J. Hageman, T. Overeem, A. J. M. Weber, *Makromol. Chem*., **1982**, *183*, 281-292.

(10) C. Decker, A. D. Jenkins, *Macromolecules*, **1985**, *18*, 1241-1244.

(11) M. Buback, B. Degener, *Makromolekulare Chemie.*, **1993**, *194*, 2875-2883.

(12) C. Decker, K. Moussa, *Makromolekulare Chemie.*, **1990**, *191*, 963-979.

(13) M. D. Dickey, C. G. Willson, *AlChE J.*, **2006**, *52*, 777-784.

(14) J. P. Fouassier, *Progress in Organic Coatings*, **1990**, *18*, 229-252.

(15) J. L. Mateo, J. Serrano, P. Bosch, *Macromolecules*, **1997**, *30*,1285-1288.

(16) S. Hu, R. Popielarz, DC. Neckers, *Macromolecules*, **1998**, *31*, 4107-4113.

(17) G. Terrones, A. J. Pearlstein, *Macromolecules*, **2001**, *34*, 8894-8906.

(18) Y. Cai, J. L. P. Jessop, *Polymer*, **2006**, *47*, 6560-6566.

(19) Y. Zhang, D. E. Kranbuehl, H. Sautereau, G. Seytre, J. Dupuy, *Macromolecules*, **2009**, *42*, 203-210.

(20) S. R. Arridget, M. Copet, D. T. Delpyi, *Phys. Med. Biol.*, **1992**, *37*, 1531-1560.

(21) M. Horowitz, *J. Applied Probability*, **1965**, *2*, 169-177.

(22) C. Decker, *Poly Intl.*, **1998**, *45*, 133-141.

(23) G. R. Tryson, A. R. Shultz, *J. Polym. Sci., Polym. Phys. Ed.*, **1979**, *17*, 2059-2075.

(24) S. A. Seabrook, M. P. Tonge, R. G. Gilbert, *J. Polymer Sci.: Part A: Polymer Chem.*, **2005**, *43*, 1357-1368.

(25) S. A. Seabrook, P. M. Pascal, P. Tonge, R. G. Gilbert, *Polyme*r, **2005**, *46*, 9562-9573.

(26) S. A. Seabrook, R. G. Gilbert, *Polymer*, **2007**, *48*, 4733-4741.

(27) O. Akyuz, A. Giz, H. Catalgil-Giz, *Macromol. Symp.*, **2009**, *275-276*, 112-119.

(28) M. J. Fevola, R. D. Hester, C. L. Mccormick, *J. Poly. Sci.: Part A: Poly. Chem.*, **2003**, *41*, 560-568.

(29) N. Nikitin, R. A. Hutchinson, M. Buback, P. Hesse, *Macromol. Chem. Phys*., **2011**, *212*, 699-707.

(30) G. Oster, N.-L. Yang, *Chemical Reviews*, **1968**, *68*, 125-151.

(31) K. S. Anseth, C. M. Wang, C. N. Bowman, *Macromolecule*s, **1994**, *27*, 650-655.

(32) M. A. Islam, *Physica Scriota*, **2004**, *70*, 120-125.

(33) M. North, G. A. Reed, *Transactions of the Faraday society*, **1961**, *57*, 859-870.

(34) G. Terrones, A. J. Pearlstein, *Macromolecules*, **2004**, *37*, 1565-1575.

(35) J. Beebe, G. A. Mensing, G. M. Walker, *Annu. Rev. Biomed. Eng.*, **2002**, *4*, 261-286.

(36) D. S. S. Nunes, F. M. B. Coutinho, *European Polymer J.*, **2002**, *38*, 1159-1165.

(37) H. Song, D. L. Chen, R. F. Ismagilov, *Angew. Chem. Int. Ed.*, **2006**, *45*, 7336 -7356.

(38) K. P. Yuet, D. K. Hwang, R. Haghgooie, P. S. Doyle, *Langmuir*, **2010**, *26*, 4281-4287.

(39) Z. Yu, C.-F. Wang, L. Ling, L. Chen, S. Chen, *Angew. Chem. Int. Ed.*, **2012**, *51*, 2375-2378.

(40) Z. Nie, W. Li, M. Seo, S. Q. Xu, E. Kumacheva, *J. Am. Chem. Soc.*, **2006**, *128*, 9408-9412.

(41) R. F. Shepherd, J. C. Conrad, S. K. Rhodes, D. R. Link, M. Marquez, D. A. Weitz, J. A. Lewis, *Langmuir*, **2006**, *22*, 8618-8622.

(42) T. Nisisako, T. Torii, *Adv. Mater.*, **2007**, *19*, 1489-1493.

(43) C.-H. Chen, R. K. Shah, A. R. Abate, D. A. Weitz, *Langmuir*, **2009**, *25*, 4320-4323.

(44) N. Prasad, J. Perumal, C.-H. Choi, C.-S. Lee, D.-P. Kim, *Adv. Funct. Mater.*, **2009**, *19*, 1656-1662.

(45) C. Holtze, M. Antonietti, K. Tauer, *Macromolecules*, **2006**, *39*, 5720-5728.

(46) C. Holtze, K. Tauer, *Macromol. Rapid Commun.*, **2007**, *28*, 428-436.

(47) J. J. Hegseth, N. Rashidinia, A. Chai, *Physical Review E.*, **1996**, *54*, 1640-1644.
(48) S. Dainton, M. Tordoff, *Transactions of the Faraday Society*, **1957**, *53*, 499-511.
(49) E. Andrzejewska, *Prog. Polym. Sci.*, **2001**, *26*, 605-665.
(50) R. Bao, S. Jönsson, *Progress in Organic Coatings*, **2008**, *61*, 176-180.
(51) M. Lyons, L. P. Hale, C. W. Wilkins, *J. Vac. Sci. Technol. B*, **1985**, *1*, 447-452.
(52) J. C. McDonald, G. M. Whitesides, *Accounts of Chemi-cal Research*, **2002**, *35*, 491-499.
(53) S. Fiorini, R. M. Lorenz, J. S. Kuo, D. T. Chiu, *Anal. Chem.*, **2004**, *76*, 4697-4704.
(54) You, S. M. Kang, S. Lee, Y. O. Cho, J. B. Kim, S. B. Lee, Y. S. Nam, H. Lee, *Angew. Chem. Int. Ed.*, **2012**, *51*, 1-6.
(55) C. H. Choi, C. J. Kim, *Nanotechnolog*, **2006**, *17*, 5326-5333.
(56) M. Im, H. Im, J. -H. Lee, J. -B. Yoon, Y. -K. Choi, *Langmuir*, **2010**, *26*, 17389-17397.
(57) C. D. Marco, S. M. Eaton, M. Levi, G. Cerullo, S. Turri, R. Osellame, *Langmuir*, **2011**, *27*, 8391-8395.
(58) T. Kawakatsu, Y. Kikuchi, M. Nakajima, *J. Am. Oil Chem. Soc.*, **1997**, *74*, 317-321.
(59) D. Dendukuri, P. S. Doyle, *Adv. Mater.*, **2009**, *21*, 1-16.
(60) S. Badilescu, M. Packirisamy, *Polymers*, **2012**, *4*, 1278-1310.
(61) T. Nisisako, T. Torii, T. Higuchi, *Chem. Engineering J.*, **2004**, *101*, 23-29.
(62) W. J. Jeong, J. Y. Kim, J. Choo, E. K. Lee, C. S. Han, D. J. Beebe, G. H. Seong, S. H. Lee, *Langmuir*, **2005**, *21*, 3738-3741.
(63) W. Li, H. H. Pham, Z. Nie, B. MacDonald, A. Güenther, E. Kumacheva, *J. Am. Chem. Soc.*, **2008**, *130*, 9935-9941.
(64) M. Seo, Z. Nie, S. Xu, P. C. Lewis, E. Kumacheva, *Langmuir*, **2005**, *21*, 4773-4775.
(65) D. Dendukuri, K. Tsoi, T. A. Hatton, P. S. Doyle, *Langmuir*, **2005**, *21*, 2113-2116.
(66) S. Q. Xu, Z. H. Nie, M. Seo, P. Lewis, E. Kumacheva, H. A. Stone, P. Garstecki, D. B. Weibel, I. Gitlin, G. M. Whitesides, *Angew. Chem*., **2005**, *117*, 734-738.
(67) K. W. Bong, K. T. Bong, D. C. Pregibon, P. S. Doyle, *Angew. Chem. Int. Ed.*, **2010**, *49*, 87 –90.
(68) M. E. Helgeson, S. C. Chapin, P. S. Doyle, *Current Opinion in Colloid & Interface Science*, **2011**, *16*, 106-117.
(69) M. Gupta, *J. Phys. II France*, **1993**, *3*, 407-419.
(70) G. F. Christopher, S. L. Anna, *J. Phys. D: Appl. Phys.*, **2007**, *40*, R319-R336.

(71) B. Theberge, F. Courtois, Y. Schaerli, M. Fischlechner, C. Abell, F. Hollfelder, W. T. S. Huck, *Angew. Chem. Int. Ed*., **2010**, *49*, 5846-5868.

(72) S. A. Khan, A. Günther, M. A. Schmidt, K. F. Jensen, Langmuir, 2004, 20, 8604-8611.

(73) L. Cao, H.-H. Hu, D. Gao, *Langmuir*, **2007**, *23*, 4310-4314.

(74) X.-M. Li, D. Reinhoudt, M. Crego-Calama, *Chem. Soc. Rev*., **2007**, *36*, 1350-1368.

(75) N. Miljkovic, R. Enright, E. N. Wang, *ACS Nano*, **2012**, *6*, 1776-1785.

(76) C. Dietz, K. Rykaczewski, A. G. Fedorov, Y. Joshi, *Applied Physics Letters*, **2010**, *97*, 033104.

(77) T. Zhang, J. Wang, L. Chen, J. Zhai, Y. Song, L. Jiang, *Angew. Chem. Int. Ed.*, **2011**, *50*, 5311-5314.

(78) Y. Wu, N. Saito, F. A. Nae, Y. Inoue, O. Takai, *Surface Science*, **2006**, *600*, 3710-3714.

(79) Shastry, M. J. Case, K. F. Bőhringer, *Langmuir*, **2006**, *22*, 6161-6167.

(80) Y. Lee, B. J. Zhang, J. Park, K. J. Kim, *International Journal of Heat and Mass Transfer*, **2012**, *55*, 2151-2159.

(81) M. Kuncicky, O. D. Velev, *Langmuir*, **2008**, *24*, 1371-1380.

(82) C.-H. Choi, C.-J. Kim, *Langmuir*, **2009**, *25*, 7561-7567.

(83) B. Balu, A. D. Berry, D. W. Hess, V. Breedveld, *Lab Chip*, **2009**, *9*, 3066-3075.

(84) J.-Y. Shiu, C.-W. Kuo, W.-T. Whang, P. Chen, *Lab Chip*, **2010**, *10*, 556-558.

(85) B. Su, S. Wang, Y. Song, L. Jiang, *Nano Res.*, **2011**, *4*, 266-273.

(86) E. Ueda, F. L. Geyer, V. Nedashkivskaab, P. A. Levkin, *Lab Chip*, **2012**, *12*, 5218-5224.

(87) A. Accardo, F. Mecarini, M. Leoncini, F. Brandi, E. D. Cola, M. Burghammer, C. Riekelc, E. D. Fabrizio, *Lab Chip*, **2013**, *13*, 332-335.

(88) C. Lima, W. Song, B. Blanco-Fernandez, C. Alvarez-Lorenzo, *J. F. Mano, Pharm Res*, **2011**, *28*, 1294-1305.

(89) H. Song, D. L. Chen, R. F. Ismagilov, *Angew. Chem. Int. Ed.*, **2006**, *45*, 7336-7356.

(90) W. Barthlot, C. Nienhuis, *Planta*, **1997**, *202*, 1-8.

(91) L. T. Shi, C. G. Jiang, G. J. Ma, C. W. Wu, *Biomicrofluidics*, **2010**, *4*, 041101.

(92) D. Tam, V. V. Arnim, G. H. Mckinley, A. E. Hosoi, *J. Fluid Mech.*, **2009**, *624*,101-123.

(93) K. Rykaczewski, J. H. J. Scott, A. G. Fedorov, *Appl. Phys. Lett.*, **2011**, *98*, 093106.

(94) S. T. Chang, O. D. Velev, *Langmuir*, **2006**, *22*, 1459-1468.

(95) G. McHale, S. Aqil, N. J. Shirtcliffe, M. I. Newton, H. Y. Erbil, *Langmuir*, **2005**, *21*,

11053-11060.

(96) E. E. Ross, S.-W. Mok, S. R. Bugni, *Langmuir*, **2011**, *27*, 8634-8644.

(97) V. Rastogi, S. Melle, O. G. Calderón, A. A. García, M. Marquez, O. D. Velev, *Adv. Mater.*, **2008**, *20*, 4263-4268.

(98) R. Bhardwaj, X. Fang, P. Somasundaran, D. Attinger, *Langmuir*, **2010**, *26*, 7833-7842.

(99) S. Utada, E. Lorenceau, D. R. Link, P. D. Kaplan, H. A. Stone, D. A. Weitz, *Science*, **2005**, *308*, 537-541.

(100) S.-Y. Teh, R. Lin, L.-H. Hung, A. P. Lee, *Lab Chip*, **2008**, *8*, 198-220.

(101) W. Li, H. H. Pham, Z. Nie, B. MacDonald, A. Güenther, E. Kumacheva, *J. Am. Chem. Soc.*, **2008**, *130*, 9935-9941.

(102) D. Velev, B. G. Prevo, K. H. Bhatt, *Nature*, **2003**, *426*, 515-516.

(103) T. M. Squires, S. R. Quake, *Rev. Mod. Phys*, **2005**, *77*, 977-1026.

(104) S.-H. Hung, Y.-H. Lin, G.-B. Lee, *J. Micromech. Microeng.*, **2010**, *20*, 1-8.

(105) M. Jalaal, B. Khorshidi, E. Esmaeilzadeh, *Experimental Thermal and Fluid Science*, **2010**, *34*, 1498-1506.

(106) G. M. Whitesides, A. D. Stroock, *Phys. Today*, **2001**, 42-47.

(107) S.-W. Lee, P. E. Laibinis, *J. Am. Chem. Soc.*, **2000**, *122*, 5395-5396.

(108) T. B. Jones, M. Gunji, M. Washizu, M. J. Feldman, *J. Appl. Phys.*, **2001**, *89*, 1441-1448.

(109) J. Zeng, T. Korsmeyer, *Lab Chip*, **2004**, *4*, 265-277.

(110) S. E. Barnes, Z. T. Cygan, J. K. Yates, K. L. Beers, *E. J. Amis, Analyst*, **2006**, *131*, 1027-1033.

(111) T. Ghannam, *J. Chem. Eng. Data*, **2002**, *47*, 274-277.

(112) E. Collinson, F. S. Dainton, G. S. McNaughton, *Trans. Faraday Soc.*, **1957**, *53*, 476-488.

(113) F. Candau, Y. S. Leong, R. M. Fitch, *J Polym Sci, Polym Chem Ed.*, **1985**, *23*, 193-214.

(114) C. Decker, *Macromol. Rapid Commun.*, **2002**, *23*, 1067-1093.

(115) C. Decker, T. Nguyen Thi Viet, D. Decker, E. Weber-Koehl, *Polymer*, **2001**, *42*, 5531-5541.

(116) M. Barahman, A. M. Lyons, *Langmuir*, **2011**, *27*, 9902-9909.

(117) T. Young, *Philos. Trans. R. Soc. London*, **1805**, *95*, 65-87.

(118) J. W. Harris, H. Stocker, *Handbook of Mathematics and Computational Science*; Springer- Verlag: New York, **1998**.

(119) M. Pearce, C. E. Wright, B. K. Bordoloi, *Laboratory Experiments in Polymer Synthesis and Characterization. Educational Modules for Materials Science and Engineering Project*, **1982**, pp 1-22.

(120) V. Gőkmen, T. K. Palazoğlu, *Journal of Food Engineering*, **2009**, *93*, 172-176.

(121) A. -R. Mahdavian, M. Abdollahi, H. R. Bijanzadeh, *J. Applied Polym. Sci.*, **2004**, *93*, 2007-2013.

(122) F. Ziaee, H. Bouhendi, F. Ziaie, *Iranian Polymer Journal*, **2009**, *18*, 947-956.

(123) J. R. Lizotte, T. E. Long, *Macromol. Chem. Phys.*, **2004**, *205*, 692-698.

(124) I. Lacík, S. Beuermann, M. Buback, *Macromolecules,* **2001**, *34*, 6224-6228.

(125) O. Olabisi, *Handbook of thermoplastics*, Marccel Dekker, Inc., New York, **1997**, pp 227-252.

(126) J. Hernández-Barajas, D. Hunkeler, *J. Polymer*, **1997**, *38*, 437-447.

(127) F. Mills, *Heat transfer*, Richard D. Irwin, INC., **1992**.

(128) E. Mark, *Polymer Data Handbook*, Oxford University Press, Inc., **1999**.

(129) I. Pješčić, C. Tranter, P. L. Hindmarsh, N. D. Crews, *Biomed Microdevices*, **2010**, *12*, 333-343.

(130) I. Shiota, Y. Miyamoto, *Functionally Graded Materials*, Elsevier science B. V., **1996**.

(131) J. Gao, A. Penlidis, *Rev. Macromol. Chem. Phys.*, **1996**, *C36*, 199-404.

(132) V. V. Krongauz, A. D. Trifunac, *Diffusion in Polymer Matrix and Anisotropic Photopolymerization. In Processes in Photoreactive Polymers*; Eds.; Chapman and Hall: New York, **1995**, p186.

(133) T. M. Lovesteada, J. A. Burdicka, K. S. Ansetha, C. N. Bowman, *Polymer*, **2005**, *46*, 6226-6234.

(134) F. Begum, S. L. Simon, *Polymer*, **2011**, *52*, 1539-1545.

(135) M. Cioffi, K. J. Ganzeveld, A. C. Hoffmann, L. P. B. M. Janssen, *Polymer Engineering And Science*, **2004**, *44*, 179-185.

(136) U. Shim, L. F. Olguin, G. Whyte, D. Scott, A. C. Babtie, C. Abell, F. Hollfelder, W. T. S. Huck, *J. Am. Chem. Soc.*, **2009**, *131*, 15251-15256.

(137) W. Y. Chen, Y. J. Yang, C. Rinadi, D. Zhou, A. Q. Shen, *Lab Chip*, **2009**, *9*, 2947-2951.

(138) E. Quevedo, J. Steinbacher, D. T. McQuade, *J. Am. Chem. Soc.*, **2005**, *127*, 10498-10499.

(139) W. Jiraprasertkul, R. Nuisin, W. Jinsart, S. Kiatkamjornwong, *J Appl. Polym. Sci.*, **2006**,

102, 2915-2928.

(140) T. H. Yang, *Recent Pat. Mater. Sci.*, **2008**, *1*, 29-40.

(141) A. Acheampong, J. W. Meulepas, P. N. Lens, *J Chem. Technol. Biotechnol.*, 2010, *85*, 590-613.

(142) S. L. Chavez, F. Rodriguez, *Chemical Engineering Communications*, **1983**, *24*, 21-36.

(143) P. Pascal, M. A. Winnik, *Macromolecules*, **1993**, *26*, 4572-4576.

(144) I. Barabanova, E.V. Bune, A.V. Gromov, V.F. Gromov, *European Polymer J.*, **2000**, *36*, 479-483.

(145) R. Murugan, S. Mohan, A. Bigotto, *J. Korean Physical Sci*., **1998**, *32*, 505-512.

(146) E. Saion, A. H. Shaari, M. Z. A. Rahman, M.D. K. Zaman, T. Kadni, A. Doyan, Susilawati, *American J. Applied Sci*., **2005**, *2*, 1248-1255.

(147) T. L. Rapp, W. K. Kowalchyk, K. L. Davis, E. A. Todd, K.-L. Liu, M. D. Morris, *Anal. Chem*., **1992**, *64*, 2434-2437.

(148) W.-J. Wang, D. Wang, B.-G. Li, S. Zhu, *Macromolecules*, **2010**, *43*, 4062-4069.

(149) *The LC Handbook Guide to LC Columns and Method Development*, Agilent Technologies, https://www.chromspec.com/pdf/e/ag34.pdf.

(150) G. Whitesides, E. E. Simanek, J. P. Mathiasc, C. Seto, D. N. Chin, M. Mammena, D. M. Gordon, *Acc. Chem. Res.*, **1995**, *28*, 37-44.

(151) G. Odian, *Principles of Polymerization*, 4th ed., Wiley Interscience, Hoboken, New Jersey, **2004**, pp 221-222.

(152) G. Odian, *Principles of Polymerization*, 4th ed., Wiley Interscience, Hoboken, New Jersey, **2004**, pp 236-243.

(153) G. Gauglitz, T. Vo-Dinh, *Handbook of Spectroscopy*, Weinheim, WILEY-VCH Verlag GmbH & Co. KgaA, **2003**, 72-73.

(154) S. R. Buss, *3D Computer Graphics: A Mathematical Introduction with OpenGL*, United Kingdom, The Press Syndicate of the University of Cambridge, **2003**, pp 96.

(155) *BlueWave 200 Spectral Output,* DYMAX Corporation.

(156) F. Ehlers, J. Barth, P. Vana, *RSC Polymer Chemistry Series No. 4, Fundamentals of Controlled/Living Radical Polymerization,* The Royal Society of Chemistry, **2013**, pp 29-31.

(157) J. Klein, K.-D. Conrad, *Makromol. Chem.*, **1980**, *181*, 227-240.

(158) L. Capretto, W. Cheng, M. Hill, X. Zhang, *Top Curr. Chem.*, **2011**, *304*, 27-68.

(159) T. Savart, C. Dove, B. J. Love, *Macromol. Mater. Eng.*, **2010**, *295*, 146-152.

(160) M. Muthukumar, *Polymer Translocation*, Taylor and Francis Group, LLC, **2011**, pp 28.

(161) P. Munk, T. M. Aminabhavi, P. Williams, D. E. Hoffman, M. Chmelir, *Macromolecules*, **1980**, *13,* 871-875.

(162) W. Ehrfeld, K. Golbig, V. Hessel, H. Löwe, T. Richter, *Ind. Eng. Chem. Res.* **1999**, *38,* 1075-1082.

(163) L. Gu, S. Zhu, A.N. Hrymak, R.H. Pelton, *Polymer*, **2001**, *42*, 3077-3086.

(164) H. B. Lee, M. S. Jhon, J. D. Andrade, *Journal of Colloid and Interface Science*, **1975**, *51*, 225-231.

(165) J. Catalán, C. Díaz, F. García-Blanco, *J. Org. Chem.*, **2001**, *66*, 5846-5852.

(166) A.S. Utada, L.-Y. Chu, A. Fernandez-Nieves, D.R. Link, C. Holtze, and D.A. Weitz, *MRS Bulletin*, **2007**, *32*, 702-708.

(167) D. Nagao, T. Ohta, H. Ishii, A. Imhof, M. Konno, *Langmuir*, **2012**, *28*, 17642-17646.

(168) *The manual of ramé-hart Model 250 standard Goniometer with DROPimage Advanced v2.4*, Ramé-hart instrument co..

(169) *The manual of Hamilton syringe*, http://www.hamiltoncompany.com/item/view/c/ 145/p/ 1598/.

(170) R. Kurose, A. Fujita, S. Komori, *J. Fluid Mechanics*, **2009**, *624*, 57-67.

(171) http://twistedsifter.com/2012/04/confluences-around-the-world/.